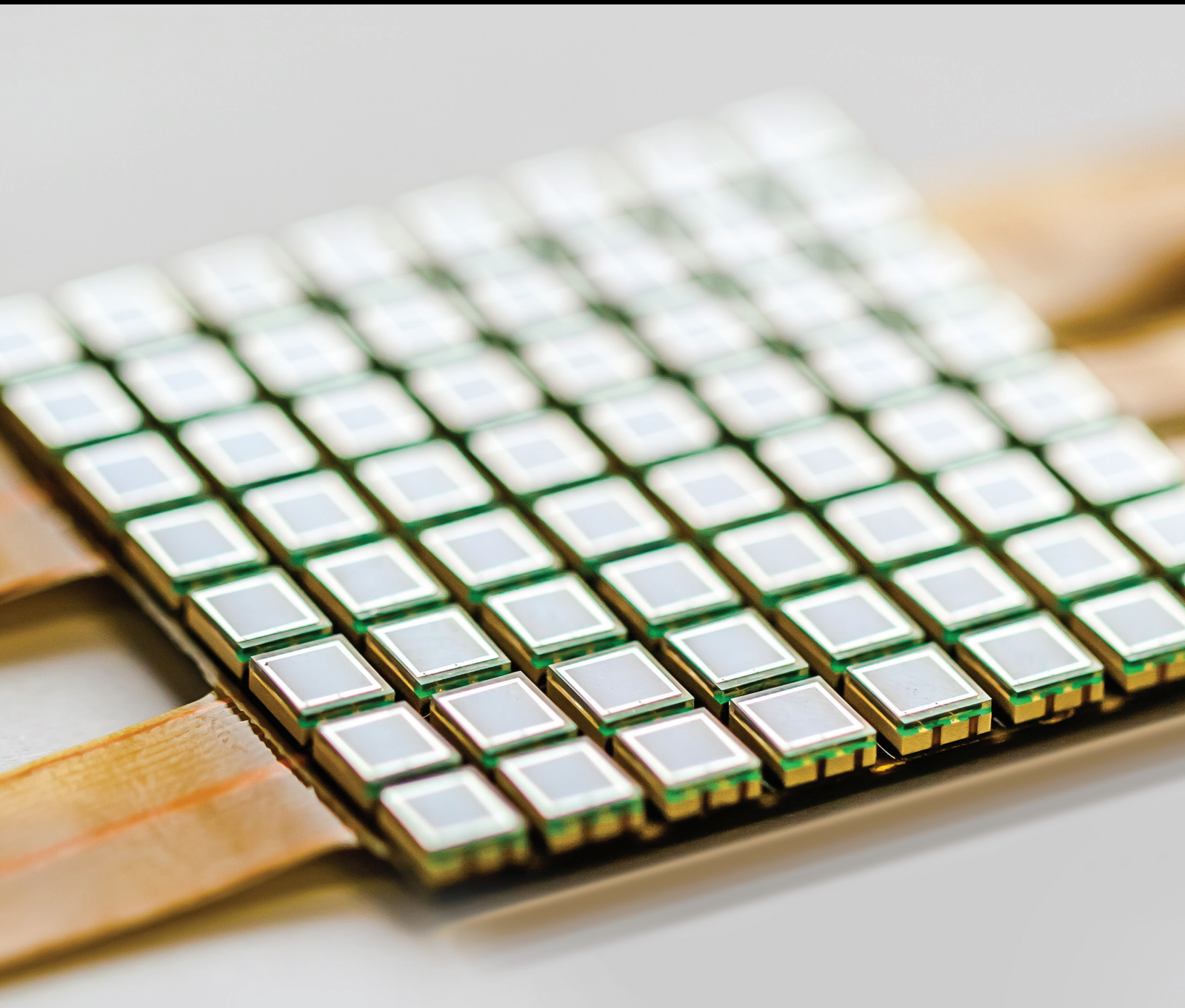


Advanced Sensing and Structural Health Monitoring

Lead Guest Editor: Young-Jin Cha

Guest Editors: Yeesock Kim and Taesun You





Advanced Sensing and Structural Health Monitoring

Journal of Sensors

Advanced Sensing and Structural Health Monitoring

Lead Guest Editor: Young-Jin Cha

Guest Editors: Yeesock Kim and Taesun You



Copyright © 2018 Hindawi. All rights reserved.

This is a special issue published in "Journal of Sensors." All articles are open access articles distributed under the Creative Commons Attribution License, which permits unrestricted use, distribution, and reproduction in any medium, provided the original work is properly cited.

Editorial Board

Harith Ahmad, Malaysia
M. İlhan Akbaş, USA
Manuel Aleixandre, Spain
Bruno Andò, Italy
Fernando Benito-Lopez, Spain
Romeo Bernini, Italy
Shekhar Bhansali, USA
Wojtek J. Bock, Canada
Paolo Bruschi, Italy
Belén Calvo, Spain
Stefania Campopiano, Italy
Domenico Caputo, Italy
Sara Casciati, Italy
Gabriele Cazzulani, Italy
Chi Chiu Chan, Singapore
Nicola Cioffi, Italy
Marco Consales, Italy
Jesus Corres, Spain
Andrea Cusano, Italy
Antonello Cutolo, Italy
Dzung Dao, Australia
Manel del Valle, Spain
Francesco Dell’Olio, Italy
Franz L. Dickert, Austria
Giovanni Diraco, Italy
Nicola Donato, Italy
Mauro Epifani, Italy
Abdelhamid Errachid, France
Stephane Evoy, Canada
Vittorio Ferrari, Italy
Luca Francioso, Italy
Manel Gasulla, Spain
Carmine Granata, Italy

Alfredo Guemes, Spain
Banshi D. Gupta, India
Clemens Heitzinger, Austria
María del Carmen Horrillo, Spain
Syed K. Islam, USA
Stephen James, UK
Hai-Feng Ji, USA
Sang Sub Kim, Republic of Korea
Antonio Lazaro, Spain
Laura M. Lechuga, Spain
Chengkuo Lee, Singapore
Chenzong Li, USA
Eduard Llobet, Spain
Jaime Lloret, Spain
Yu-Lung Lo, Taiwan
Oleg Lupan, Moldova
Frederick Mailly, France
Santiago Marco, Spain
Vincenzo Marletta, Italy
Eugenio Martinelli, Italy
Antonio Martínez Olmos, Spain
Jose R. Martínez-De-Dios, Spain
Giuseppe Maruccio, Italy
Yasuko Y. Maruo, Japan
Mike McShane, USA
Fanli Meng, China
Stephen. J. Mihailov, Canada
Heinz C. Neitzert, Italy
Calogero M. Oddo, Italy
M. Palaniswami, Australia
Alberto J. Palma, Spain
Lucio Pancheri, Italy
Roberto Paolesse, Italy

Alain Pauly, France
Giorgio Pennazza, Italy
Michele Penza, Italy
Salvatore Pirozzi, Italy
Antonina Pirrotta, Italy
Stavros Pissadakis, Greece
Biswajeet Pradhan, Malaysia
Armando Ricciardi, Italy
Christos Riziotis, Greece
Maria Luz Rodriguez-Mendez, Spain
Jerome Rossignol, France
Carlos Ruiz, Spain
Josep Samitier, Spain
Giorgio Sberveglieri, Italy
Andreas Schütze, Germany
Sandra Sendra, Spain
Woosuck Shin, Japan
Pietro Siciliano, Italy
Vincenzo Spagnolo, Italy
Sachin K. Srivastava, India
Stefano Stassi, Italy
Vincenzo Stornelli, Italy
Weilian Su, USA
Tong Sun, UK
Raymond Swartz, USA
Hidekuni Takao, Japan
Guiyun Tian, UK
Suna Timur, Turkey
H. Vaisocherova-Lisalova, Czech Republic
Xavier Vilanova, Spain
Luca Vollero, Italy
Qihao Weng, USA
Hai Xiao, USA

Contents

Advanced Sensing and Structural Health Monitoring

Young-Jin Cha , Yeesock Kim, and Taesun You
Editorial (3 pages), Article ID 7286069, Volume 2018 (2018)

Analysis of Wave-Induced Current Using Digital Image Correlation Techniques

Bumshick Shin  and KyuHan Kim 
Research Article (6 pages), Article ID 1784507, Volume 2018 (2018)

Self-Powered Wireless Sensor Network for Automated Corrosion Prediction of Steel Reinforcement

Dan Su, Ye Xia , and Robert Yuan
Research Article (10 pages), Article ID 4125752, Volume 2018 (2018)

Neck Flexion Angle Estimation during Walking

Duc Cong Dang, Quoc Khanh Dang, Young Joon Chee, and Young Soo Suh
Research Article (9 pages), Article ID 2936041, Volume 2017 (2018)

Impedance Based Health Monitoring Technique with Probabilistic Neural Network for Possible Wall Thinning Detection of Metal Structures

Wongi S. Na and Jongdae Baek
Research Article (11 pages), Article ID 8950518, Volume 2017 (2018)

The Research on Information Representation of Φ -OTDR Distributed Vibration Signals

Yanzhu Hu, Song Wang, Zhaoyang Wang, and Yixin Zhang
Research Article (12 pages), Article ID 6020645, Volume 2017 (2018)

Impact of Pyrotechnics over the Architectonic Heritage

Angel T. Lloret, Sandra Sendra, Jaime Lloret, Miguel Louis Cereceda, and Jesus Alba
Research Article (11 pages), Article ID 7214975, Volume 2017 (2018)

Performance Evaluation of Plain Weave and Honeycomb Weave Electrodes for Human ECG Monitoring

Xueliang Xiao, Sandeep Pirbhulal, Ke Dong, Wanqing Wu, and Xi Mei
Research Article (13 pages), Article ID 7539840, Volume 2017 (2018)

Editorial

Advanced Sensing and Structural Health Monitoring

Young-Jin Cha ¹, **Yeesock Kim**,² and **Taesun You**³

¹*Department of Civil Engineering, University of Manitoba, Winnipeg, MB, Canada R3T 5V6*

²*Department of Civil Engineering and Construction Management, California Baptist University, Riverside, CA, USA*

³*Houston District, Texas Department of Transportation, Houston, TX, USA*

Correspondence should be addressed to Young-Jin Cha; young.cha@umanitoba.ca

Received 11 April 2018; Accepted 11 April 2018; Published 10 May 2018

Copyright © 2018 Young-Jin Cha et al. This is an open access article distributed under the Creative Commons Attribution License, which permits unrestricted use, distribution, and reproduction in any medium, provided the original work is properly cited.

Structural health monitoring (SHM) is currently a hot topic within the engineering disciplines due to the aging of civil infrastructures in North America and other regions. The scope of the application of SHM is increasingly broad, ranging from civil infrastructures to human health monitoring. In order to implement SHM, many advanced sensors have been developed, from contact-based sensors (such as microelectromechanical sensors) to noncontact sensors (such as air-coupled sensors, vision sensors using cameras, wireless rechargeable sensor networks, and radar sensor networks). With the advancements in these sensors and sensing system technologies, many methods of structural damage detection, localization, and quantification have also been developed. However, there are still a remarkable number of questions associated with both damage detection and the validation of detected damage using traditional sensors for civil infrastructures, mechanical systems, environmental changes, and human health.

One of the critical missions in SHM is discovering how to determine damage-sensitive features and how to extract information about them from the data measured by sensors, in order to detect damage or changes to systems. It is a challenging problem. A number of damage-sensitive features have been suggested, experimented upon, and tested, but there are as yet few successful cases of detecting structural damage from traditional contact sensors in civil infrastructure. Most of the methods, with their specific damage-sensitive features, were able to provide alerts about changes in the monitored systems. However, they were not able to detect specific damages (and their locations in large-scale infrastructure) because of the many associated uncertainties,

including environmental changes and changes of boundary conditions. Nondestructive testing-based damage assessment for local damage has been quite successful by using impact-echo-based damage detection or piezoelectric sensors. The main problem with these approaches is that they require numerous sensors to cover the entire civil infrastructure. Even though these sensors can be applied to critical locations on the structures (based on engineering data), the location of the identified damage may be quite random.

To give an example from one of the papers in this special issue, a corrosion detection method using contact sensors was proposed. Structural deterioration due to aging is generally expressed as corrosion in steel structures, so corrosion detection and quantification are critical for evaluating the useful remaining life of structures. Many approaches have been proposed to detect steel corrosion or steel rebar corrosion in reinforced concrete beams, one of which is the use of contact sensors, but that approach uses a self-powered wireless sensor network for automated corrosion prediction. In order to monitor the progress of the corrosion of embedded steel reinforcement, a vibration-based energy harvester was developed for continuous corrosion data collection. Due to the nature of contact sensors, such a system cannot monitor locations where sensors are not installed. To cover the unmonitored areas, a spatial interpolation module was proposed to interpolate measured data from the sensors. The developed method provided for a period of five years an accurate prediction of corrosion by comparing the monitored data.

Corrosion of structures and/or wall thinning in pipes that could significantly reduce their mechanical strength can be

detected by another structural health monitoring method, electromechanical impedance (EMI). A reattached EMI method has been developed to reduce the high cost of covering large areas, but, in spite of the efficiency of the reattached EMI method, there remains a problem: The impedance signatures are changed by reattaching the piezoelectric transducer. This issue can be solved by using a probabilistic neural network algorithm. An integrated electromechanical impedance method with probabilistic neural network algorithm was developed to measure the thickness of a metal layer stack. Repeatability with high accuracy can be achieved by integrating the probabilistic neural network algorithm with the electromechanical impedance method and selecting the result most frequently appearing among measurements. When the reattached EMI method is applied to monitoring large structures such as bridges and buildings, the small sensing area it is able to cover causes difficulty and problems related to cost. A promising potential solution to those problems may be the use of a drone with an embedded solar-powered battery.

Among the contact-sensor-based approaches in this special issue, the wireless sensor network (WSN) is widely used in a variety of areas including military industries, agriculture, and infrastructure monitoring. In particular, it is a promising method for effectively monitoring structures with historical significance. Many events and festivals, for which the use of pyrotechnics is popular and frequent, take place near historic buildings. The vibroacoustic impacts of fireworks, which can potentially weaken historic structures, can be monitored by a WSN. Experiments have been conducted to measure sound levels in dB and acceleration for a variety of events, including fireworks, cannon firing, and multiple rifle shots. It has been shown that the vibroacoustic impacts of pyrotechnics cannot be ignored in narrow areas such as alleys, while they are insignificant in a broad, open area. These experiments have been performed with realistic scenarios during actual festivals, resulting in practical findings. The effects of pyrotechnics on historical structures have been monitored and quantified in terms of both acoustics and vibration. The integration of WSN into various historic buildings and other structures will be required to develop a robust and reliable monitoring method for measuring the effects of pyrotechnics.

Many vibration-based damage detection approaches have been developed using traditional contact sensors, such as accelerometers and strain gauges. However, many of these traditional methods require a large number of contact sensors, and managing the number of sensors required to monitor a typical large-scale civil infrastructure is challenging. The postprocessing of the measured data from these sensors is a huge task with tremendous computational costs. Selecting and extracting damage-sensitive features from the measured data is the most critical, yet difficult, aspect of detecting potential future damage. In addition, confirming whether the collected data actually indicates structural damage or results from sensory system malfunction, noisy signals, or a combination of these things typically requires that the sensing systems and structures be checked in person. Thus, regular visual inspection by trained engineers is still a

common method of SHM. However, human-based visual inspection is expensive, which leads to low inspection frequency and is restricted by the inaccessibility of areas such as the underside of bridge systems.

In order to overcome the drawbacks of traditional contact-sensor-based approaches, computer-vision-based methods have been proposed that use image processing techniques (IPTs) to detect damage and partially replace visual inspection. As an example from this special issue, advanced digital image correlation techniques were used for years to monitor erosion and sedimentation occurring repeatedly on South Korea's east coast. A three-dimensional (3D) hydraulic model was developed to investigate the effects of waves induced by the current to transport sediment. Using very sensitive high-resolution video cameras, images were obtained to upgrade the existing dot-unit measuring method to a plane-unit measuring method. From this study, the generation routes of longshore currents and strong rip currents were calculated and the flow direction and flow velocity measured by the plane-unit method in field observations showed very similar tendencies to those of 3D hydraulic model tests.

Another example is the phase-sensitive optical time-domain reflectometer (Φ -OTDR), which is widely used in health monitoring to extract a distributed vibration signal in order to enhance the accuracy and efficiency of the monitoring. For two-dimensional (2D) use of Φ -OTDR, a time-encoded signal processing (TESP) algorithm can be used to effectively reduce redundancy and increase effectiveness, even for fiber points with poor signal-to-noise ratio (SNR). Moreover, in the case of three-dimensional data in Φ -OTDR, two methods—empirical mode decomposition (EMD) and nonnegative matrix factorization (NMF)—can be combined and optimized by the genetic algorithm (GA) method. Better performance on the length and time dimensions is shown in a Φ -OTDR signal represented by the TESP method and the combined EMD and NMF method optimized by the GA method (GAEMD-NMF method). The accuracy of the TESP method and the similarity between the GAEMD-NMF results and the sensor signal in frequency domain are both enhanced. Both 2D and 3D Φ -OTDR vibrant signals can be represented with high accuracy and improved similarity. The TESP method is used for 2D signals, while the GAEMD-NMF method is used for 3D signals. The effectiveness and practicability of the TESP and GAEMD-NMF methods are proved by experimental tests in a controlled anechoic chamber. A broad range of experimental tests is required for further validating the TESP and GAEMD-NMF methods.

SHM approaches are currently being used to monitor human health, including neck pain, one of the more common musculoskeletal disorders (MSDs). In order to understand the primary cause of an instance of neck pain, the head flexion posture during walking is measured by an inertial sensor (using information on gravitational forces) attached to the neck. The craniovertebral angle (CVA) is measured using an OptiTrack camera system with experimental verification. This study investigated the relationship between CVA and neck flexion angle (NFA) in both static and dynamic cases. The results indicated that NFA has a close relationship to

CVA. Although the authors showed the good performance of the proposed method, there is clearly a need for more extensive experimental studies and a better algorithm for estimating a variety of angles.

In another study, physiological parameters were monitored using an electrocardiogram (ECG) to diagnose chronic cardiovascular diseases. This long-term monitoring requires wearable electrodes that are breathable, flexible, biocompatible, and friendly to the skin. Four conductive weave electrodes were developed for an extensive study of their performance as a sensing system. From these experiments, it was learned that conductive fabric for use on human skin must have lower skin-electrode impedance and greater comfort.

The technology of SHM is growing, and new technologies are introduced every year, even though many questions remain to be answered. In this special issue, we found potential solutions to address practical issues ranging from how to apply SHM methods to civil infrastructures and human bodies to improving on traditional contact-sensor-based approaches by using noncontact vision sensors. However, these vision-based approaches also require damage-sensitive features in order to pinpoint damage, and each approach can theoretically detect only a specific type of damage. Consequently, deep learning-based damage detection methods have recently been developed using a convolutional neural network [1, 2], although that development is not addressed in this special issue. The main advantage of deep learning-based approaches is that they automatically extract damage-sensitive features for multiple kinds of damage. Within a couple of years, we expect to see many new approaches and methods using these deep learning algorithms with noncontact vision sensors and autonomous, unmanned aerial vehicles to expand the scope of SHM.

*Young-Jin Cha
Yeesock Kim
Taesun You*

References

- [1] Y. J. Cha, W. Choi, and O. Büyüköztürk, "Deep learning-based crack damage detection using convolutional neural networks," *Computer-Aided Civil and Infrastructure Engineering*, vol. 32, no. 5, pp. 361–378, 2017.
- [2] Y. J. Cha, W. Choi, G. Suh, S. Mahmoudkhani, and O. Büyüköztürk, "Autonomous structural visual inspection using region-based deep learning for detecting multiple damage types," *Computer-Aided Civil and Infrastructure Engineering*, 2017.

Research Article

Analysis of Wave-Induced Current Using Digital Image Correlation Techniques

Bumshick Shin  and **KyuHan Kim** 

Catholic Kwandong University, Gangneung, Republic of Korea

Correspondence should be addressed to Bumshick Shin; bs.shin@gmail.com

Received 2 September 2017; Revised 12 November 2017; Accepted 17 January 2018; Published 10 April 2018

Academic Editor: Young-Jin Cha

Copyright © 2018 Bumshick Shin and KyuHan Kim. This is an open access article distributed under the Creative Commons Attribution License, which permits unrestricted use, distribution, and reproduction in any medium, provided the original work is properly cited.

Recently, advancement of digital image techniques and communications technology has enabled the application of existing images for scientific purposes. Furthermore, both quantitative and qualitative analyses of images have become possible through image processing such as transmit/storage of digital image data and image rectification. In this study, a coast having representative characteristics of east coast of Korea was selected with having erosion in winter, and the sedimentation in summer takes place repeatedly. Three-dimensional hydraulic model test was conducted to analyze its outcomes by a digital image correlation technique in order to understand the wave-induced current affecting the sediment transport. For this study, images filmed by the high-sensitive and high-resolution video camera were converted into stopped images of regular intervals and then those converted images were used for the following procedure to analyze flow and velocity into digital coordinates. The outcomes from interpretation of images filmed by the high-sensitive and high-resolution video camera can be utilized as a very useful analysis method for appreciating the generation mechanism and movement route of longshore current and rip current.

1. Introduction

When acquiring information of wave and current in a wide sandy beach, a number of measuring instruments are needed which is time-consuming and inefficient in economical purposes. Nonetheless, recent advancement of digital image techniques and communications technology has enabled the application of existing images for scientific purposes. Furthermore, both quantitative and qualitative analyses of images have become possible through image processing such as transmit/storage of digital image data and image rectification. Especially, these methods are useful in long-time observation without much cost that are employed for studies on coastal phenomena or coastal changes. In order to study the uprush of waves along coastline, Holman and Guza introduced the Argus time-lapse photography technique [1]. Holman and Lippmann [2] developed the technique for the observation of a three-dimensional shape of offshore bar which measures the topography and scale of natural offshore based on the shape of incoming breaking waves by the application of remote observation technology.

Holman et al. [3] showed an example of measuring the depth of water at coasts by using videos which caused less cost even for a longer period of time. Lippmann and Thornton [4] employed stereo video analysis technique to measure sea level rise, beach slope, and visibility. Liang and Puleo [5] applied an image interpretation technique to measure the surface flow. Vos [6] first noted observations of the developmental stages of a transient rip current on the Western coast of Australia. Symonds et al. [7] further characterized the development and decay of a rip with time-exposed video imagery.

The image sensor used for image interpretation, which is a semiconductor module converting optical images into electric signals, can be referred to as a kind of electronic part used for reproducing optical images in device for storing, transmitting, and displaying images. Generally, there are two types of image sensors, which are CCD and CMOS. CCD has the features of having less noise and better image quality than the CMOS while production of CMOS cost and power consumption is lower than that of CCD. Also, CMOS makes it easier for peripheral circuits to be integrated into identical

chips. Arita and Deguchi [8] introduced a considerable number of studies that have been conducted on the spatial wave distributions by using two CCD video camera images. These studies analyzed azimuth difference of digital images taken by video cameras.

In this study, the authors proposed the procedure to measure surface profile by applying stereo matching method of two images of the sea surface without any targets or tracers. IPX-11M5-GCxx made up of CCD image sensors with superior image quality and less noise was employed for the interpretation of video image data through digital image processing technique to analyze the generation and flow of wave-induced current.

2. Description of Digital Image Correlation Techniques

2.1. Image Coordinate Using Photogrammetry. The basis of understanding stereo imaging is the pinhole camera model which can be seen in the figure below [9]. The process of image interpretation is based on geometry having principles of photogrammetry. The position of a coordinate can be expressed as a function of the position on the ground corresponding to the position, the focal length, and the tilt of camera, swing, azimuth, and elevation. Formulas are expressed in the following:

$$(x, y) = f(X, Y, Z_c, f_c, t, f, s, H), \quad (1)$$

where (x, y) and X, Y, Z_c mean the coordinate in the image and the real coordinate on the ground which correspond to (x, y) in the image, respectively. And $f_c, t, s,$ and H mean the focal distance of the camera, tilt of the camera (upward from horizontal axis), azimuth (counter clockwise), swing or the roll angle, and the height from the origin of the coordinate, respectively.

2.2. Projective Transformation. Images have to be filmed vertically from the selected sea area for higher accuracy; however, it is not easy to obtain any vertical image. Therefore, the peripheral structures in the subject area should be filmed to get sloped images so that a digital orthoimage may be obtained through projective transformation as shown in Figure 1. The digital orthoimage, a fundamental principle of photographic survey, is based on a geometric condition of collinearity condition which arbitrary points in a space (or points of a subject: $X_p, Y_p,$ and Z_p), the points (x, y) on the photo corresponding to them, and the filming focus on the photo $(X_0, Y_0,$ and $Z_0)$ should be collinear.

When using collinearity condition, Z in (2) becomes the same, and the height of the cameras is always consistent and produces the projective transformation formula as shown in (3). This formula is valid when the sloped and vertical plane of the measured subject surface is flat even if it is not horizontal, where the coordinate transformation becomes possible with the evaluation of b1-b8. Moreover, the control points more than 4 are needed for the evaluation of b1-b8 parameters. Through the evaluation of the position $(X_0, Y_0,$ and $Z_0)$ of the camera, taking pictures and its slope (κ, ψ, ω) with the applied collinearity condition will lead to

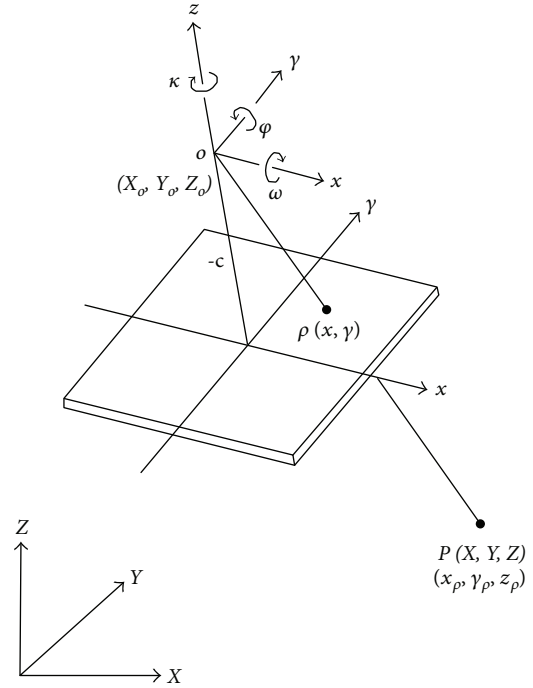


FIGURE 1: Projective transformation.

the correlation between photo coordinate (x, y) and ground coordinate $(X, Y,$ and $Z)$ where C is the focal distance.

$$\begin{aligned} X &= \frac{b_1x + b_2y + b_3}{b_7x + b_8y + 1}, \\ Y &= \frac{b_4x + b_5y + b_6}{b_7x + b_8y + 1}, \\ x &= -c \frac{x_p}{z_x}, \\ y &= -c \frac{y_p}{z_y}. \end{aligned} \quad (2)$$

$$\begin{pmatrix} x_p \\ y_p \\ z_p \end{pmatrix} = \begin{pmatrix} 1 & 0 & 0 \\ 0 & \cos \omega & \sin \omega \\ 0 & \sin \omega & \cos \omega \end{pmatrix} \begin{pmatrix} \cos \varnothing & 0 & \sin \omega \\ 0 & 1 & 0 \\ -\sin \omega & 0 & \cos \varnothing \end{pmatrix} \cdot \begin{pmatrix} \cos \kappa & -\sin \kappa & 0 \\ \sin \kappa & \cos \kappa & 0 \\ 0 & 0 & 1 \end{pmatrix} \begin{pmatrix} X - X_0 \\ Y - Y_0 \\ Z - Z_0 \end{pmatrix}. \quad (3)$$

3. Hydraulic Model Test and Image Interpretation

In this study, a coast having representative characteristics of east coast of Korea was selected with having erosion in winter, and the sedimentation in summer takes place repeatedly. Three-dimensional hydraulic model test was conducted to

TABLE 1: Wave basin and directional wave maker specifications.

| | | Specifications | Scene |
|------------|--------------|--------------------------------------|--|
| Wave basin | | 40 m(L) × 32 m(W) × 1.5 m(H) |  |
| | Wave boards | 0.75 m(W) × 1.5 m(H) | |
| | Wave maker | 36 m (0.75 m × 48 ea) | |
| | Max wave | 0.5 m | |
| | Period range | 0.5 sec~5.0 sec | |
| Wave maker | Type | Snake & piston type (AE servo motor) | |

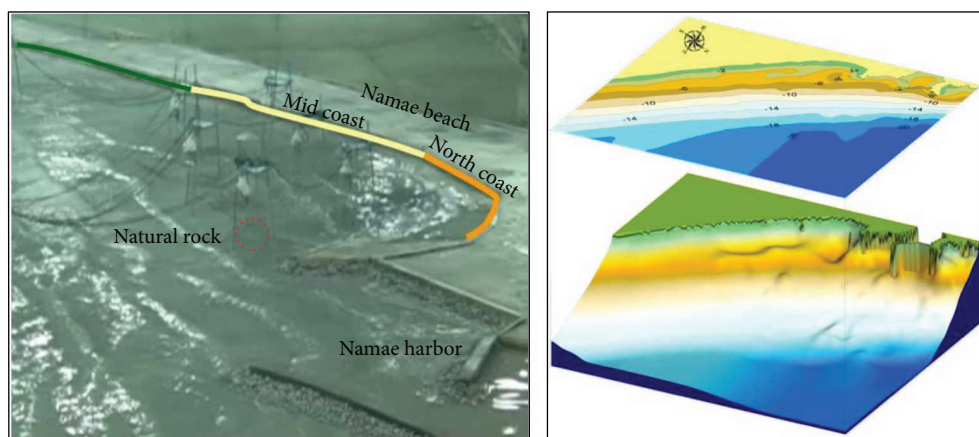


FIGURE 2: Bottom topography and experimental setup.

TABLE 2: Camera specifications.

| | | Specifications | Image |
|--------------|---------------|------------------------------|---|
| Model | | PX-4M15-LCFN |  |
| Manufacturer | | KYOCERA | |
| | Pixel | 2048 × 2048 | |
| | Data clock | 40 MHz | |
| Spec | Frame rate | 15 fps (dual), 118 fps (max) | |
| | Shutter speed | 1/20000~1/7 sec | |

analyze its outcomes by a digital image correlation technique in order to understand the wave-induced current affecting the sediment transport.

3.1. 3D Hydraulic Model Test. A 3D hydraulic model test, which was reduced according to similarity law, was carried out at the topography of real sea for the review of the applicability of wave-induced current monitoring through image interpretation technique [10, 11]. For this experiment, the high-sensitive and high-resolution video camera image interpretation system including CCD image sensor which is to be applied at the fields was employed for filming as shown in Table 1.

3.2. Modelling. The model considered that water flows from south to north for both summer and winter, so it reproduced

a range of 1500 m of south and 900 m of north including Namae port with Namae beach in the center where wave-induced current can be affected. The study is located at Namae beach at the center of a wave generator and a basin in order to earn the optimal estimation result as shown in Figure 2.

Moreover, 2.2 km is selected from coast line to offshore to simulate water depth of 20 m that may have an effect on incident wave. The model and water level production used recently published Digital Maritime Chart and site survey of water depth data by Korea Hydrographic and Oceanographic Administration.

3.3. Image Process. In the 3D hydraulic model test, quantitative data have been acquired through image digitalization,



FIGURE 3: Before projective transformation.

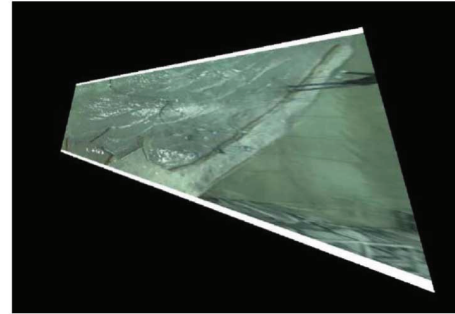


FIGURE 4: After projective transformation.

coordinate rectification, and image processing after filming of the physical phenomena such as waves and current generated along with the movement of wave makers by the high-sensitive and high-resolution video camera (IPX-11M5-GCxx). Table 2 shows the image sensors applied for filming. A considerable number of studies have been conducted on the spatial wave distributions by using two video camera images. These studies analyzed azimuth difference of digital images taken by video cameras. In this study, the authors proposed the procedure to measure surface profile by applying stereo matching method of two images of the sea surface without any targets or tracers. The validity of the proposed procedure was examined through the experiment in a wave basin.

For this study, images filmed by the high-sensitive and high-resolution video camera were converted into stopped images of regular intervals and then those converted images were used for the following procedure to analyze flow and velocity into digital coordinates.

- (1) Filming: creation of stopped images of regular interval (40 seconds) from filmed video images
- (2) Control point measuring: total station used for measuring control points which would be applied in case of any change to the shapes of shore protection or to protection
- (3) Protective transformation: 9 control points measured by total station adopted for protective transformation of stopped images to create vertical digital orth image as shown in Figures 3 and 4
- (4) Calibration: confirmation to see if protective transformation was carried out correctly after comparing the outcomes of control point measurement with the images after protective transformation
- (5) Image extraction (wave-induced current image analysis): pixels of water-blue part by the application of RGB image data to each image
- (6) Creation of image data: marking the extracted pixels on coordinate system

3.4. Simulation Results. Flow pattern of wave-induced current from three-dimensional hydraulic model test and field

investigation data was similar in many parts. In the test, we observed the longshore current which flows from south to north in ENE, ESE wave direction was the dominant flow pattern, and current velocity was 0.28 m/sec during ESE wave direction and 0.16 m/sec during ENE wave direction. Flows that generated from the south was moving along the beach in forms of longshore current, and it was changed into rip current at near the underwater rock, moving to offshore. Meanwhile, some currents that start from headland of north beach were moving toward to the beach and were transformed into rip current at the same place. We observed that rests were not moving to the open sea but were stagnated at harbor entrance located in the north. It proves that harbor siltation at harbor entrance was generated not only in summer but also in other seasons.

The result of the test is shown in Figure 5 and was analyzed by PIV method. Generally, beach transformation of the coast occurs daily in a short term and several years in a long term. But constant beach transformation may lead to transformations in heights and surface areas in overall coast area. Since current videos have too low resolution to monitor a beach transformation for the transformation investigation in units of centimeter, we considered the characteristics of coast and its surface to find the causes of beach transformation. VMS (video metric systems) and PIV (particle image velocimetry) methods were applied to overcome the limits of resolution and location with several camera installations. As a result, analysis of sea marker's flow state showed a velocity of moving flow of 0.12~0.28 m/sec.

Those filmed images were interpreted, compared with those results from digital model test and hydraulic model experiment for verification, and also compared with the results of field observation by Shin and Kim [12]. The interpretation of images filmed from 3D hydraulic model test showed that wave-induced current was moving from south to north with the velocity of 0.2~0.5 cm/sec, which outcomes were estimated to be similar to those from digital model test of Kim et al. [10], and also confirmed to have the same characteristic as a result of peak velocity measured at hydraulic model test. Moreover, comparison with the outcomes of field observation by Kim and Shin [12] revealed that these comparisons corresponded with the analysis results of wave-induced current by the digital image correlation technique.

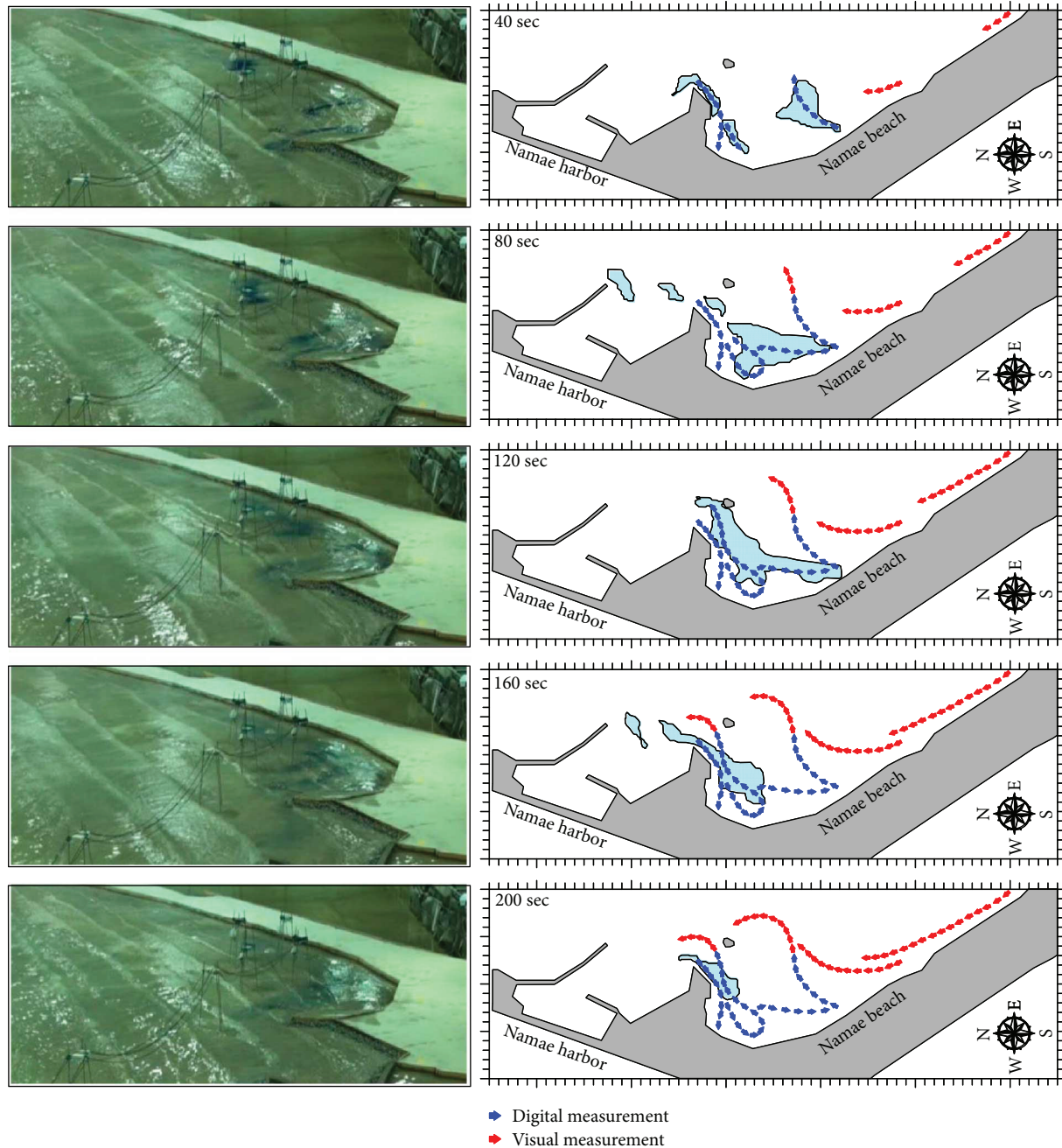


FIGURE 5: Flow patterns of wave-induced current in 3-dimensional hydraulic model test.

4. Conclusion

In this study, images obtained by unit-hour in specific time zones were extracted from the ground of images filmed by high-sensitive and high-resolution video cameras so as to improve the existing dot-unit measuring method to plane-unit measuring method. Also, those image data were geometrically corrected, which were applied for reviewing generating mechanism and moving route of wave-induced current. The interpretation of images enabled the confirmation of generation routes of longshore current and strong rip

current, which results were found to have a very similar tendency to those of point measurement at preceding hydraulic model tests, flow direction and flow velocity measured at digital model test, and plane unit at field observation.

The outcomes from interpretation of images filmed by the high-sensitive and high-resolution video camera can be utilized as a very useful analysis method for appreciating the generation mechanism and movement route of longshore current and rip current. As a result, the paths of longshore current and strong rip current were found. It is expected that the video metric system employed in this study will be

effectively utilized in field tests in the near future to further study the mechanism of wave-induced current occurrence and its paths.

Conflicts of Interest

The authors declare that they have no conflicts of interest.

References

- [1] R. A. Holman and R. T. Guza, "Measuring run-up on a natural beach," *Coastal Engineering*, vol. 8, no. 2, pp. 129–140, 1984.
- [2] R. A. Holman and T. C. Lippmann, "Remote sensing of near-shore bar systems-making morphology visible," in *Proceedings of Coastal Sediments '87*, ASCE, pp. 929–944, New York, NY, USA, 1987.
- [3] R. A. Holman, A. H. Sallenger, T. C. Lippmann, and J. W. Haines, "The application of video image processing to the study of nearshore processes," *Oceanography*, vol. 6, no. 3, pp. 78–85, 1993.
- [4] T. C. Lippmann and E. B. Thornton, "Observation of surf zone wave breaking during Duck 94," in *25th International Conference on Coastal Engineering: Book of Abstracts*, pp. 720–721, Orlando, FL, USA, 1996.
- [5] H. Liang and J. A. Puleo, "PIV measurements of surface flows in laboratory wave basins," *Journal of Flow Visualization and Image Processing*, vol. 16, no. 1, pp. 1–18, 2009.
- [6] R. G. Vos, "Observations on the formation and location of transient rip currents," *Sedimentary Geology*, vol. 16, no. 1, pp. 15–19, 1976.
- [7] G. Symonds, R. A. Homan, and B. Bruno, "Rip currents," in *Proc. Coastal Dynamics '97*, pp. 584–593, 1997.
- [8] M. Arita and I. Deguchi, "Measurement of wave surface using digital video camera," *Proceedings of the Coastal Engineering, JSCE*, vol. 54, pp. 1426–1430, 2007.
- [9] B. Jähne, *Practical Handbook on Image Processing for Scientific Applications*, CRC Press, Inc., Boca Raton, FL, USA, 1995.
- [10] K. H. Kim, H. S. Yoo, and N. Kobayashi, "Mitigation of beach erosion after coastal road construction," *Journal of Coastal Research*, vol. 274, no. 4, pp. 645–651, 2011.
- [11] K. H. Kim and J. S. Seo, "Investigation of characteristics of wave induced currents using hydraulic model experiment," in *Proceedings of the 2016 International Conference on Applied Engineering, Materials and Mechanics (ICAEMM 2016)*, pp. 267–272, Weihai, China, 2016.
- [12] B. S. Shin and K. H. Kim, "Rip current monitoring using video analysis," *Journal of Coastal Research*, vol. 72, pp. 28–32, 2014.

Research Article

Self-Powered Wireless Sensor Network for Automated Corrosion Prediction of Steel Reinforcement

Dan Su,^{1,2} Ye Xia ,¹ and Robert Yuan³

¹Tongji University, Shanghai, China

²Embry Riddle Aeronautical University, Daytona Beach, FL, USA

³Lamar University, Beaumont, TX, USA

Correspondence should be addressed to Ye Xia; yxia@tongji.edu.cn

Received 25 July 2017; Revised 31 October 2017; Accepted 16 November 2017; Published 8 January 2018

Academic Editor: Young-Jin Cha

Copyright © 2018 Dan Su et al. This is an open access article distributed under the Creative Commons Attribution License, which permits unrestricted use, distribution, and reproduction in any medium, provided the original work is properly cited.

Corrosion is one of the key issues that affect the service life and hinders wide application of steel reinforcement. Moreover, corrosion is a long-term process and not visible for embedded reinforcement. Thus, this research aims at developing a self-powered smart sensor system with integrated innovative prediction module for forecasting corrosion process of embedded steel reinforcement. Vibration-based energy harvester is used to harvest energy for continuous corrosion data collection. Spatial interpolation module was developed to interpolate corrosion data at unmonitored locations. Dynamic prediction module is used to predict the long-term corrosion based on collected data. Utilizing this new sensor network, the corrosion process can be automated predicted and appropriate mitigation actions will be recommended accordingly.

1. Introduction

Corrosion is a deterioration process that would alternate the properties of the material because of a reaction with its environment. Similar to other natural hazards and environmental attacks, corrosion can cause dangerous and expensive damage to different objects from automobiles to pipelines, bridges, and other essential infrastructure systems. Furthermore, the aging infrastructure is one of the most serious problems faced by our society today and corrosion is one of the most severe environmental attacks that affects the service life and functionality of aging infrastructure.

The corrosion of embedded steel reinforcement is one of the principal causes of deterioration of reinforced concrete. It is presumed that when the embedded steel is protected from air by a thick cover of a low permeability concrete, the corrosion problem of steel would not arise. But in reality, this may not be entirely true since many properly built reinforced and prestressed concrete structures show premature deterioration due to steel corrosion. Rebar corrosion is one of the major forms of environmental attack to reinforced concrete,

which may lead to reduction in strength, serviceability, and aesthetics of the structure, as well as affect the application of reinforcement. The corrosion of embedded steel reinforcement will greatly affect the performance, functionality, and serviceability of the structure.

The damage to concrete resulting from the corrosion of embedded steel is visible in the form of expansion, cracking, and eventual spalling of the cover [1, 2]. Besides the loss of cover, a reinforced concrete member suffers structural damage due to loss of bond between steel and concrete and loss of rebar cross-sectional area and its functionality.

Because the corrosion occurs on the embedded reinforcement, the detection of corrosion can be extremely difficult. At early ages, coring sample was the only method to detect the corrosion. However, the coring would only indicate the corrosion condition at the coring location but would not reveal the true condition of structure as a whole. Therefore, corrosion detection technologies were developed including chain drag method (ASTM D4580-12), electrochemical half-cell potential (HCP), Tafel extrapolation technique (TP), linear polarization resistance (LPR) [3–5], macrocell

current (MC) [6], radio-frequency identification (RFID), and sacrificial sensors (SS).

Over the past decades, number of researches have been performed to develop efficient monitoring methods and techniques. Electrochemical methods were investigated and examined at early stage of corrosion monitoring research [7–9]. Later, Baronio et al. [10] performed steel corrosion monitoring based on potential measurements. El-Mahdy et al. [11] conducted electrochemical corrosion monitoring under cyclic wet-dry conditions. Elsener [12] studied the microcell corrosion process of steel in concrete. Montemor et al. [13] presented an overview of chloride-induced corrosion process and monitoring techniques. Moreover, various techniques including galvanostatic pulse technique [14, 15], acoustic emission method [16–18], electrochemical impedance spectroscopy (EIS) [19, 20], and electrochemical noise analysis (ENA) method [19] were developed. Various types of sensors and reference electrodes were developed for corrosion monitoring [21–28]. Automatic system [29], remote corrosion monitoring system [30], 3-D monitoring system [31], and multielectrode system [32] were also developed recently. Performance of different corrosion monitoring techniques were reviewed, compared, and assessed [33–35]. In addition, some of the researches focused on evaluating/modeling of chloride ingress in concrete based on laboratory and field measured data [36–39].

Initiation time of steel reinforcement corrosion is another important parameter to predict and understand corrosion mechanism of steel reinforcement. Daigle et al. [36] proposed a formula to predict the time of corrosion initiation compose parameters of concrete cover, chloride threshold, and chloride concentration. There are many factors affecting the corrosion rate including temperature, oxygen supply, relative humidity, chloride concentration, alkalinity, resistivity, galvanic interaction, and rust layer formation. There are three main approaches that developed over the years to estimate the corrosion rate [40]: (1) models based on electrochemistry, (2) models related to a diffusion-limited access of oxygen, and (3) models in the form of empirical relations.

Besides corrosion detection, corrosion prediction is also very important in mitigating corrosion damage and associated with deterioration. Over the years, several corrosion prediction methods have been developed by the researchers. Among these prediction methods, some of them focus on the prediction of corrosion rate while other methods focus on prediction of service life of reinforced concrete. While prediction of service life of reinforced concrete is important, corrosion rate or section losses of reinforcement would be a more appropriate parameter to evaluate the performance of the reinforcement in resisting corrosion. As summarized in Figure 1, there are four types of approaches for prediction of corrosion rate [40]: (1) physics-based models, (2) empirical models, (3) statistical prediction models based on various statistical techniques, and (4) heuristic data model.

For physics-based models, there are several approaches that can be used to model the reinforcement corrosion based on electrochemistry, diffusion-limited access of oxygen, and volume-discretization method. The physics-based model developed based on electrochemistry is the most

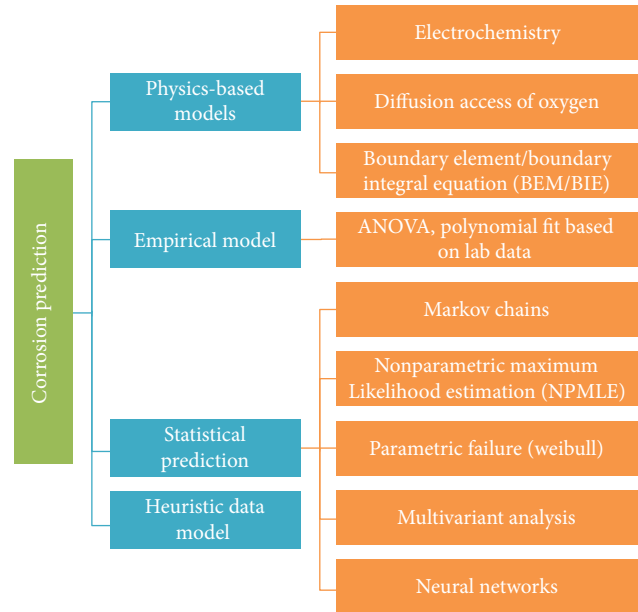


FIGURE 1: Corrosion prediction method.

common approach. Many researches have been performed to develop a complex corrosion model based on electrochemical principles and Butler-Volmer kinetics [40–43]. Advanced data filtering method and computer programs were also developed in recent years [44, 45]. However, a great amount of details are required for the utilization of these models. Thus, it is impractical for practicing engineers to apply them for the prediction of corrosion [40]. Physics-based models can also be developed based on diffusion-limited access of oxygen. It is known that the access of O_2 at the steel surface in the cathodic zone of rebars is directly related to the corrosion reaction rate. Kobayashi and Shuttoh [46] found that the moisture content of concrete greatly affects the O_2 diffusion efficient. Sudjono and Seki [47] concluded that the coefficient of O_2 diffusion decreases near linearly when the water content increased from 0 to 80%. Boundary element method/boundary integral equation (BEM/BIE) is another physics-based method. BEM/BIE uses Faraday's law for boundary motion to surface flux and uses polarization curves to fit boundary values into the integral equation. One advantage of BEM/BIE is it can incorporate other physical phenomena that impacts corrosion such as stress and impressed current cathodic protection into calculation. On the other hand, BEM/BIE needs detailed polarization curves which is site-specific to each specimen, electrolytic environment, stress, time, and other factors thus is not very practical to apply.

Corrosion prediction models can also be developed based on empirical relations. Siemes et al. [48] proposed a typical empirical model $V_{\text{corr}} = m_o/\gamma \prod F_i$, where V_{corr} is the corrosion rate, m_o is the factor given by the corrosion rate versus electrical resistivity, γ is the electrical resistivity of the concrete, and F_i is the factor influencing the local corrosion rate including chloride corrosion rate factor, galvanic effect factor, oxygen availability factor, and the oxide (rust)

factor. There are several other empirical models that have been developed based on limited data from experimental studies [49, 50]. However, these empirical models are developed based on limited experimental data and do not reflect the basic electrochemical reactions as well as the true nature of the corrosion process thus cannot be used for other cases without proper validation.

Since the reinforcement corrosion depends on many random variables such as temperature, ohmic resistance, chloride content, and exposure time, the corrosion can be predicted using statistical models. Various statistical techniques can be used including Weibull analysis, Monte Carlo simulation, Bayesian networks, Markov chains, and neural networks. However, the prediction needs to be validated and updated based on actual experimental data to ensure the accuracy of prediction. Heuristic data model is another analytical method for corrosion prediction. Heuristic models combine information from design rules, engineering lessons, and observations, and it provides another approach to predict the future corrosion trend of steel reinforcement. Recently, deep learning and machine learning methods also showed promising results in damage detection and prediction [51, 52].

Overall, these corrosion detection and monitoring techniques enable the engineers to detect and monitor the corrosion process of embedded steel reinforcement. However, the key issues related to long-term power supply, data transmission, and long-term reliability need to be addressed.

2. Critical Issues Related to Corrosion Detection and Prediction

Although there are many ways to detect corrosion and predict the corrosion rate, there are some critical issues that hinder the application of these methods in the industry level. These critical issues are as follows:

(1) Local to spatial:

all the previous researches are focused on detection of corrosion at various locations but did not provide a solution on interpolation of corrosion in a spatial scale, which is crucial when evaluating the overall global corrosion condition.

(2) Integration of detection and prediction:

the link between corrosion detection and prediction is missing. To be able to fully utilize the data collected from corrosion detection and take the mitigation action prior to severe corrosion, the corrosion detection and prediction should be integrated as one product.

(3) Data collection, transmission, and storage:

most of the corrosion detection techniques require power supply and wired connection, which greatly limited the broad application in the industrial level. With innovated wireless and energy harvesting

technology, a wireless, battery-less sensor network is desired.

(4) Static versus dynamic self-updating:

the current corrosion prediction methods are static methods that did not consider the variation of environmental conditions and structural conditions over time.

(5) Manual versus automated:

due to lack of linkage between detection data and prediction, manual inputs and modeling are required for corrosion prediction and this procedure needs to be improved; therefore, automated prediction can be performed.

Besides these general critical issues, there are many other unsolved issues related to corrosion detection and prediction. Figure 2 presents the comparison of current and proposed corrosion prediction method.

3. Proposed Wireless Sensor Network

In order to develop a corrosion monitoring and prediction system that integrates monitoring, data processing, spatial interpolation, prediction, alert triggering, and decision making, the research framework depicted in Figure 3 is adopted. It contains various modules for different functions. Experimental and analytical studies is closely integrated to achieve automated corrosion prediction for embedded steel reinforcement.

3.1. Corrosion Monitoring and Data Collection Module. Due to the critical issues presented in previous sections, there is an urgent need to develop a reliable, durable, self-powered, and wireless sensor network for long-term corrosion monitoring. A corrosion monitoring sensors that coupled with energy harvesting modules allow long-term monitoring of steel rebar corrosion with minimum maintenance requirements. It is well documented that the power requirement of SHM systems is especially a problem for structures in remote areas. It is even more critical for corrosion monitoring since corrosion of steel reinforcement takes tens of years to develop thus normal battery power cannot last that long period of time. Therefore, a self-powered wireless corrosion sensor with energy harvesting feature has been developed in this research.

The main energy harvesting sources in structures are solar, thermal gradient, wind and aeroelastic vibration, and ambient mechanical vibration. There are several emerging concepts in harvesting energy from concrete structures. Yu et al. [53] used the corrosion energy to produce electrical energy for wireless sensors. Ye and Soga [54] developed a methodology that converts water distribution system movement to electrical energy. García and Partl [55] proposed a method to harvest energy using parallel air conduits placed inside the asphalt that generates airflow to trigger wind turbines. In general, the selection of proper energy sources depends on the power requirement, the

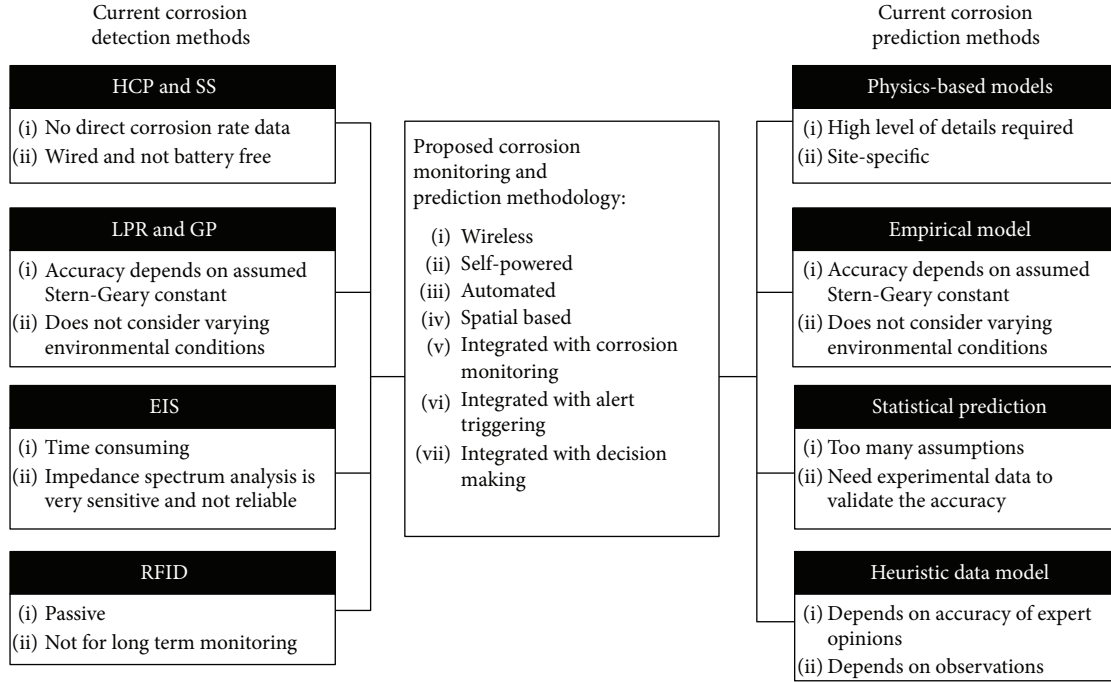


FIGURE 2: Comparison of current and proposed corrosion prediction methods.

installation location, and available ambient energy. As shown in Table 1, the power density that generates from different sources varies.

Currently, most of energy-harvesting devices (with the exception of solar panels) are in prototype phase and only have been tested under controlled laboratory conditions. Thus, in this research, a self-powered wireless sensor network with energy harvesting capability that can be used in harsh field conditions is developed.

Although there are many sources that can be used to harvest energy, considering the limited availability and lack of consistency for solar radiation and thermal gradient, ambient vibration is a good source of ambient energy that can be used to convert to usable electrical energy due to the fact that the majority of steel reinforced concrete structure subjected to dynamic loading including wind, seismic, machinery, and vehicular load. There are several types of vibration-based energy harvesters: piezoelectric vibration energy harvesters (PE-VEH), electrostatic vibration energy harvester (ES-VEH), and electromagnetic vibration energy harvester (EM-VEH) [57]. Due to usage of initial charging source and requirement of the electronic switch circuit during the operation, ES-VEH is not a good option in comparison with PE-VEH and EM-VEH. Comparing PE-VEH and EM-VEH, PE-VEH is used in this research due to its relatively better power density/acceleration performance.

As shown in Figure 4, for piezoelectric vibration energy harvester, a piezoelectric material is deposited on the surface of the steel reinforcement. When the reinforcement vibrates or deforms, the piezoelectric material is subjected to deformation as well. Due to the nature of piezoelectric material, the deformation will induce voltage. Figure 4(b) shows a

prototype self-powered wireless corrosion sensor that has been installed in reinforced concrete deck for long-term monitoring. The total potential energy can be estimated using (1) developed by Rhimi and Lajnef [58]

$$U = \frac{1}{2} \int_{V_s} S^T T dV_s + \frac{1}{2} \int_{V_p} S^T T dV_p + \frac{1}{2} \int_{V_p} E^T D dV_p + \frac{1}{2} \int_L P \left(\frac{\partial u}{\partial x} \right)^2 dx, \quad (1)$$

where S is strain, T is stress, E is electric field, D is electric displacement, and V is the volume of piezoelectric material.

The battery-free corrosion sensors coupled with wireless modules including gateway and base station enables continuous real-time data collection. Since communication of data consumes significant amount of energy. Thus, data transmission and routing are carefully designed to minimize the consumption of power. Data compression method is applied to reduce the data size. There are two compression algorithms: lossless and lossy compression. Because the lossless compression guarantees the integrity of data without distortion, lossless compression algorithm is used in this study. Comparing to the existing corrosion detection/monitoring system, the key features of this approach are (1) the use of energy harvesting instead of battery powered. Battery-powered sensors impose great limitation on the length of possible service life of the sensor since the sensor will be embedded with the steel reinforcement. Especially for the monitoring of a process as corrosion that takes long time to develop, the continuous power supply over tens of years is essential; another key feature is (2) the application of wireless technology. Taking advantage of state-of-the-art wireless technology to establish

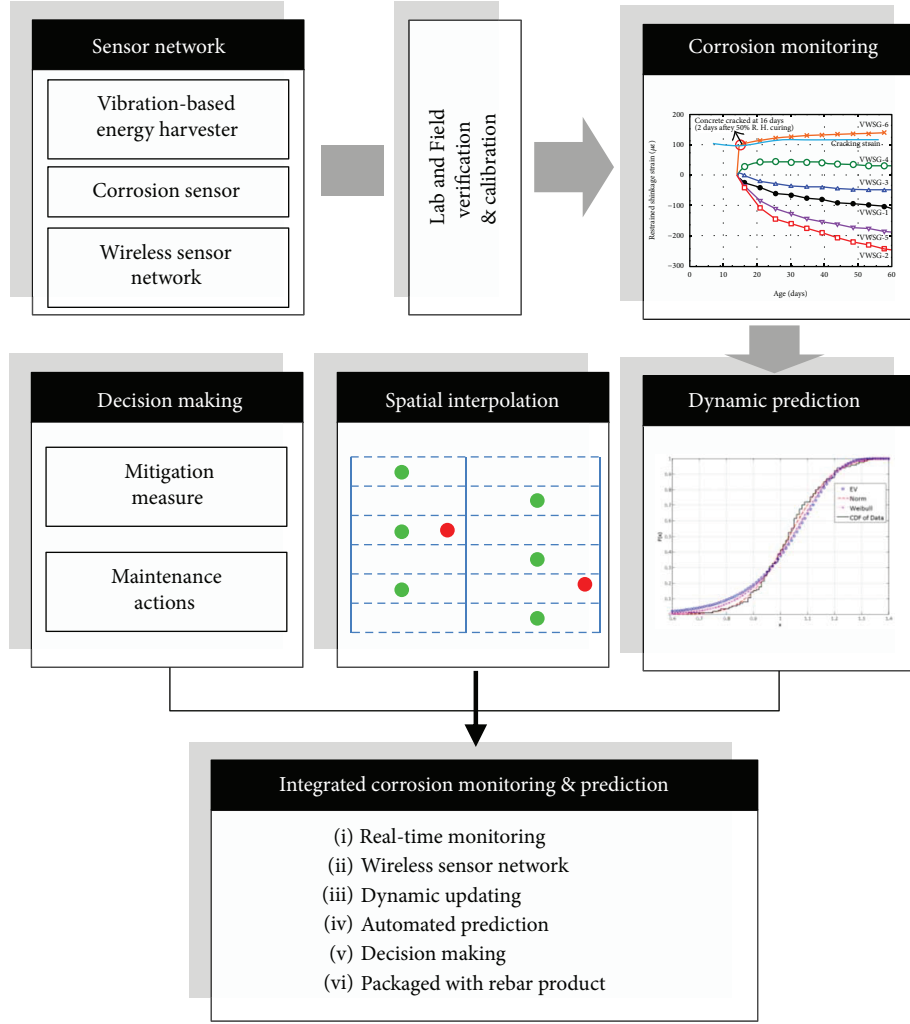


FIGURE 3: Research framework.

TABLE 1: Characteristics of various energy-harvesting techniques [56].

| | Conditions | Power density | Area or volume | Energy/day |
|-----------|------------------------------|------------------------------|-------------------|--|
| Vibration | 1 m/s ² | 100 μ W/cm ³ | 1 cm ³ | 8.64 J |
| Solar | Outdoors | 7500 μ W/cm ² | 1 cm ² | 324 J (assuming light is available for 50% of the time) |
| Solar | Indoors | 100 μ W/cm ² | 1 cm ² | 4.32 J (assuming light is available for 50% of the time) |
| Thermal | $\Delta T = 5^\circ\text{C}$ | 60 μ W/cm ² | 1 cm ² | 2.59 J (assuming light is available for 50% of the time) |

a wireless sensor network to replace the traditional wired sensor network is a significant advancing.

3.2. Spatial Interpolation Module. Because only limited number of sensors can be instrumented in the field, in order to obtain the corrosion condition from the structure level, a spatial interpolation algorithm is needed. As illustrated in Figure 5, a series of sensors will be installed at selected locations (green and purple dots). Data from some of the sensors (green dots) will be used as input for spatial interpolation model while data from other sensors (purple dots) will be used to validate the model. Various input/validation sensor combinations will be examined to identify the most accurate

interpolation model to predict the corrosion at unknown locations (red dots).

The spatial correlation of different locations will be examined by spatial statistical simulation with semivariogram. Semivariogram is a statistical tool that measures regionalized spatial variable $x(\mathbf{u}_\alpha)$, where \mathbf{u}_α is the coordinate vector at each of the observation points in a two or three dimensional space [59]. The empirical semivariogram $\gamma(\mathbf{h})$ can be calculated using

$$\gamma(\mathbf{h}) = \frac{1}{2N(\mathbf{h})} \sum_{\alpha=1}^{N(\mathbf{h})} [x(\mathbf{u}_\alpha) - x(\mathbf{u}_\alpha + \mathbf{h})]^2, \quad (2)$$

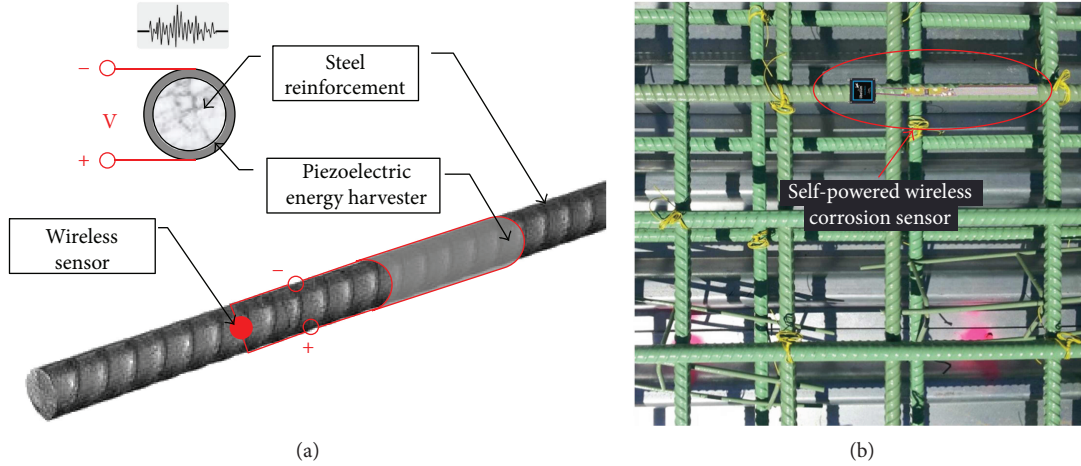


FIGURE 4: (a) Scheme for wireless corrosion sensor and (b) prototype.

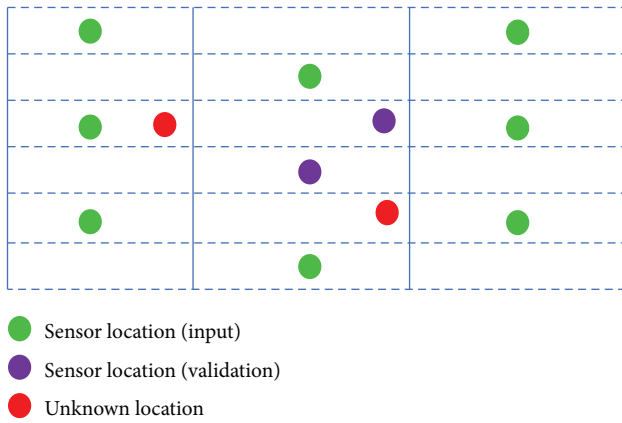


FIGURE 5: Illustration of spatial interpolation.

where $\gamma(\mathbf{h})$ is the estimated value of the semivariance for vector \mathbf{h} ; $N(\mathbf{h})$ is the number of experimental pairs separated by vector \mathbf{h} ; and $x(\mathbf{u}_\alpha)$ is a spatial variable.

Various statistical models including spherical, exponential, Gaussian, linear, and power models will be used to fit the experimental semivariograms. The model that produces the least error will be used for further analysis.

There are several spatial interpolation methods available including arithmetic mean method, the nearest neighbor method, distance weighted method, and polynomial interpolation method. Because kriging method considers the spatial structure properties and spatial correlations, kriging will be used for spatial interpolation modeling. Using the structural properties of semivariogram and the initial set of experimental data values, kriging is capable of making optimal, accurate estimates of regionalized variable at unknown locations. Spatial interpolated prediction $Z_{\text{ok}}(x_0)$ from ordinary kriging (OK) is defined as follows:

$$Z_{\text{ok}}(x_0) = \sum_{\alpha=1}^n \lambda_{\alpha}^{\text{ok}} Z(x_{\alpha}), \quad (3)$$

where $\lambda_{\alpha}^{\text{ok}}$ is the OK weights and the summation should be equal to 1. Thus, the key to an appropriate prediction is selecting appropriate weights for respective available observations. The criteria of selection are to minimize the kriging variance $\sigma_{\text{ok}}^2(x_0) = -\gamma(0) - \sum_{\alpha=1}^n \sum_{\beta=1}^n \lambda_{\alpha}^{\text{ok}} \lambda_{\beta}^{\text{ok}} \gamma(x_{\alpha} - x_{\beta}) + 2 \sum_{\alpha=1}^n \lambda_{\alpha}^{\text{ok}} \gamma(x_{\alpha} - x_0)$, where γ is the estimated value of the semivariance. This minimization process can be done using Lagrange multipliers.

3.3. Corrosion Prediction Module. Corrosion prediction can be mystical since the corrosion of steel reinforcement is a long process and it is invisible and even is not noticeable unless the concrete cover got peeled off. However, on the other hand, accurate prediction of corrosion is very important and extremely helpful for the owner to develop a more efficient maintenance plan and take mitigation measures in advance. As presented in previous sections, there are several corrosion prediction methods that have been developed. However, there are some critical issues that limited the further and wide application of these prediction methods. Furthermore, since there is no direct linkage between data collection and prediction, tremendous effects are needed to perform the corrosion prediction and there is no practical way to validate the accuracy of the prediction. Therefore, the authors developed a corrosion prediction algorithm that is automated, self-updating, and incorporated with corrosion monitoring and data collection.

For time-related variation or development, there are two quantitative forecasting methods that can be used: (1) causal models and (2) time series models. Comparing to causal models, time series models take trend, cyclical, seasonal, and irregular events into consideration and its progressive feature provides a unique updating algorithm which greatly improves the accuracy of prediction. Thus, automatic time series forecasting is used for corrosion prediction in this study. Many predictive models have been investigated including linear, quadratic, exponential, autoregressive, and state-space models. For automatic time series forecasting algorithm, if the observed corrosion rate is denoted by y_1 ,

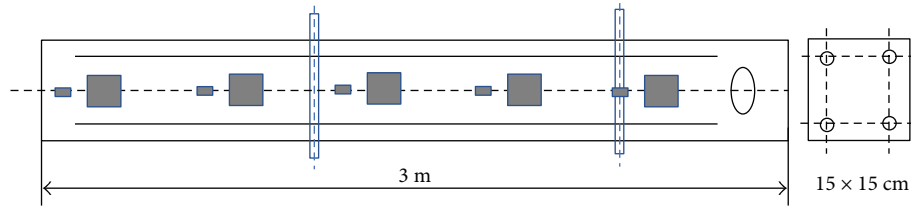


FIGURE 6: Specimens prepared for field exposure [62].

y_2, \dots, y_n . A forecast denoted as $\hat{y}_{t+h|t}$ at h periods ahead can be estimated using $\hat{y}_{t+h|t} = l_t + b_t h + s_{t-m} + h_m^+$, where m is the length of seasonality, l_t represents the level of the series, b_t represents the growth, s_t is the seasonal component, and $h_m^+ = [(h-1) \bmod m] + 1$. l_t , b_t , and s_t can be calculated using [60]

$$\begin{aligned} l_t &= \alpha(y_t - s_{t-m}) + (1 - \alpha)(l_{t-1} + b_{t-1}), \\ b_t &= \beta^*(l_t - l_{t-1}) + (1 - \beta^*)b_{t-1}, \\ s_t &= \gamma(y_t - l_{t-1} - b_{t-1}) + (1 - \gamma)s_{t-m}, \end{aligned} \quad (4)$$

where the initial state of each parameter l_0 , b_0 , and s_{1-m}, \dots, s_0 and the smoothing parameters α , β^* , and γ can be estimated from experimental data.

To evaluate the accuracy of the predictive models, measures such as mean squared error (MSE) can be applied. However, it might difficult to draw reliable conclusions because of too few out-of-sample errors. Thus, a penalized likelihood method such as Akaike's information criterion (AIC) that based on in-sample fit has been proven to be a better approach and is used in this study to evaluate the accuracy of the predictive models. The formulas for AIC method are presented in the following equations:

$$\begin{aligned} \text{AIC} &= L^*(\hat{\theta}, \hat{x}_0) + 2q, \\ L^*(\theta, x_0) &= n \log \left(\sum_{t=1}^n \varepsilon_t^2 \right) + 2 \sum_{t=1}^n \log |r(x_{t-1})|, \end{aligned} \quad (5)$$

where $L^*(\hat{\theta}, \hat{x}_0)$ is the maximum likelihood function, $\theta = (\alpha, \beta, \gamma, \phi)'$, $x_0 = (l_0, b_0, s_0, s_{-1}, \dots, s_{-m+1})'$, n is the number of observations, $\varepsilon_t = y_t - \mu_t$ is the one-step forecast error at time t . q is the number of parameters in θ plus the number of free states in x_0 . The model that produce the least AIC will be selected for corrosion prediction.

The framework for automatic prediction algorithm can be summarized as (1) for each set of experimental data, apply all models and optimize the smoothing parameters and initial state variables for each model; (2) calculate AIC and select the best model based on AIC; (3) produce prediction at various time points using the best model with optimized parameters; (4) and continuously update the prediction based on newly collected experimental data.

4. Proof of Concept

Due to the lack of reliable sensors that can be used for long-term corrosion monitoring, very limited experimental study

has been performed on long-term corrosion performance of embedded reinforcement especially under field conditions. Flint and Cox [61] investigated the resistance of stainless steel partly embedded in concrete to corrosion by seawater under lab conditions. However, no continuous data was collected on corrosion of steel. Gartner et al. [62] evaluated the long-term corrosion performance of embedded reinforcement based on monitoring data for more than five years under various conditions. Multielectrodes coupled with stainless or carbon steel electrical resistance (ER) probes were embedded in reinforced concrete columns which placed vertically in sea water under a bridge. As shown in Figure 6, corrosion was monitored at five different exposure zones: the in-water zone, the zone below the surface, the tidal zone, the splash zone, and the dry zone. The monitoring lasted for five years with measurements being taken several times a year. In order to validate the prediction algorithm that developed in this study, the long-term corrosion monitoring data collected by Gartner et al. [62] was used.

Figures 7 and 8 present the comparison between experimental data collected by Gartner et al. [62] and predicted values using the algorithm presented in this research for tidal zone and in-water zone, respectively. As shown in the comparison, using the prediction algorithm presented in this research, the prediction accurately represented the trends of corrosion at different locations for a period of 5 years. The prediction captured seasonal variation and the trends of peak values. Abnormal drop was observed in measured current at tidal zone around 1100 days (Figure 7). Since the overall trend is upward, it is suspected the drop is because of improper measurement or reading. Furthermore, due to the self-updating nature of prediction algorithm, the prediction will become even more accurate when more data is available.

5. Conclusions

Although the corrosion of embedded steel reinforcement is one of the major attacks that affects the serviceability and service life of concrete infrastructures, there is no existing technology that could provide reliable long-term monitoring data due to the limitation on battery life and data communication, let alone future prediction. In this paper, an automated corrosion prediction framework was developed for embedded steel reinforcement. With a self-powered wireless sensor network incorporated with spatial interpolation module and corrosion prediction module, the long-term corrosion of embedded reinforcement can be monitored and predicted efficiently and accurately. Prototype sensors were developed and installed in a reinforced concrete bridge deck.

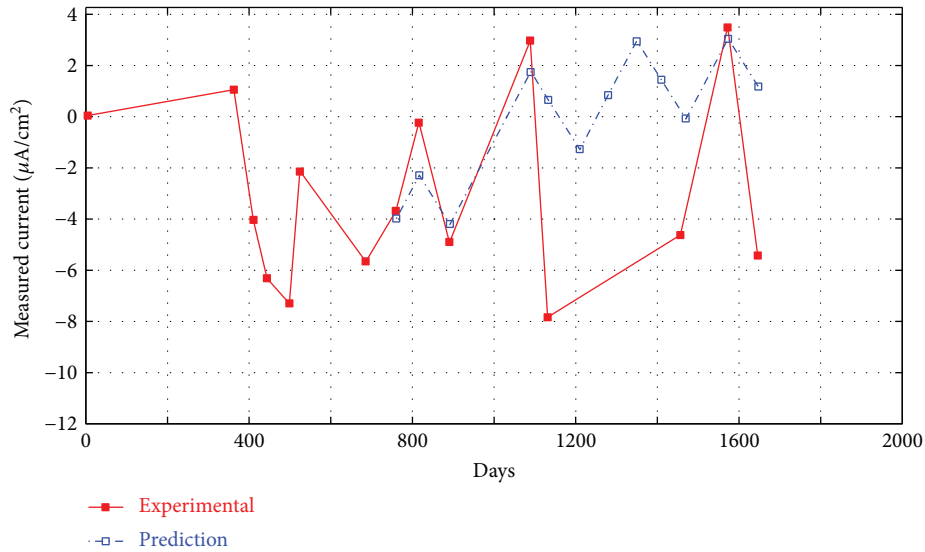


FIGURE 7: Comparison between experimental data and prediction (tidal zone).

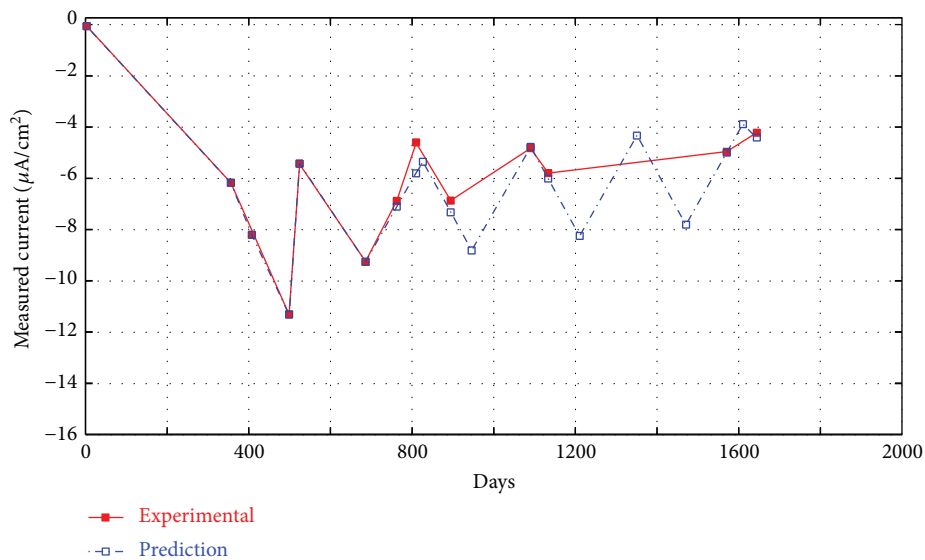


FIGURE 8: Comparison between experimental data and prediction (in-water zone).

In addition, the prediction algorithm was compared and examined using five years of monitoring data and the prediction accurately represented the trends of corrosion at different locations.

Conflicts of Interest

The authors declare that they have no conflicts of interest.

Acknowledgments

The authors would like to thank Dr. Bhaskar Yalamanchili and Gerdau Ameristeel for their valuable inputs to the research presented herein. The support for the corresponding author by National Natural Science Foundation of China (Grant No. 51508405), Ministry of Transport of the People's

Republic of China (Grant No. 2015318J38230), Science and Technology Commission of Shanghai Municipality (Grant Nos. 17DZ1204301 and 17DZ1204103), and the Fundamental Research Funds for the Central Universities is greatly acknowledged.

References

- [1] P. D. Cady, "Chapter 19—corrosion of reinforcing steel," in *Significance of Tests and Properties of Concrete and Concrete-Making Materials*, pp. 275–275-25, ASTM International, West Conshohocken, PA, USA, 1978.
- [2] Y. Xia, H. Nassif, and D. Su, "Early-age cracking in high performance concrete decks of a curved steel girder bridge," *Journal of Aerospace Engineering*, vol. 30, no. 2, article B4016003, 2017.

- [3] S. Ahmad, "Reinforcement corrosion in concrete structures, its monitoring and service life prediction—a review," *Cement and Concrete Composites*, vol. 25, no. 4-5, pp. 459–471, 2003.
- [4] N. S. Berke, V. Chaker, and D. Whiting, *Corrosion Rates in Steel in Concrete*, ASTM, West Conshohocken, PA, USA, 1990.
- [5] H. Böhni, Ed., *Corrosion in Reinforced Concrete Structures*, Elsevier, 2005.
- [6] M. Raupach, "Chloride-induced macrocell corrosion of steel in concrete—theoretical background and practical consequences," *Construction and Building Materials*, vol. 10, no. 5, pp. 329–338, 1996.
- [7] M. Pourbaix, "Applications of electrochemistry in corrosion science and in practice," *Corrosion Science*, vol. 14, no. 1, pp. 25–82, 1974.
- [8] P. R. Vassie and M. McKenzie, "Electrode potentials for on-site monitoring of atmospheric corrosion of steel," *Corrosion Science*, vol. 25, no. 1, pp. 1–13, 1985.
- [9] G. K. Glass, C. L. Page, N. R. Short, and S. W. Yu, "An investigation of galvanostatic transient methods used to monitor the corrosion rate of steel in concrete," *Corrosion Science*, vol. 35, no. 5–8, pp. 1585–1592, 1993.
- [10] G. Baronio, M. Berra, L. Bertolini, and T. Pastore, "Steel corrosion monitoring in normal and total-lightweight concretes exposed to chloride and sulphate solutions part I: potential measurements," *Cement and Concrete Research*, vol. 26, no. 5, pp. 683–689, 1996.
- [11] G. A. El-Mahdy, A. Nishikata, and T. Tsuru, "Electrochemical corrosion monitoring of galvanized steel under cyclic wet-dry conditions," *Corrosion Science*, vol. 42, no. 1, pp. 183–194, 2000.
- [12] B. Elsener, "Macrocell corrosion of steel in concrete – implications for corrosion monitoring," *Cement and Concrete Composites*, vol. 24, no. 1, pp. 65–72, 2002.
- [13] M. F. Montemor, A. M. P. Simões, and M. G. S. Ferreira, "Chloride-induced corrosion on reinforcing steel: from the fundamentals to the monitoring techniques," *Cement and Concrete Composites*, vol. 25, no. 4-5, pp. 491–502, 2003.
- [14] S. Sathiyarayanan, P. Natarajan, K. Saravanan, S. Srinivasan, and G. Venkatachari, "Corrosion monitoring of steel in concrete by galvanostatic pulse technique," *Cement and Concrete Composites*, vol. 28, no. 7, pp. 630–637, 2006.
- [15] H. W. Song and V. Saraswathy, "Corrosion monitoring of reinforced concrete structures-a," *International Journal of Electrochemical Science*, vol. 2, pp. 1–28, 2007.
- [16] M. Fregonese, H. Idrissi, H. Mazille, L. Renaud, and Y. Cetre, "Initiation and propagation steps in pitting corrosion of austenitic stainless steels: monitoring by acoustic emission," *Corrosion Science*, vol. 43, no. 4, pp. 627–641, 2001.
- [17] M. S. Weng, S. E. Dunn, W. H. Hartt, and R. P. Brown, "Application of acoustic emission to detection of reinforcing steel corrosion in concrete," *Corrosion*, vol. 38, no. 1, pp. 9–14, 1982.
- [18] P. Ziehl and M. ElBatanouny, "Acoustic emission monitoring for corrosion damage detection and classification," *Corrosion of Steel in Concrete Structures*, pp. 193–209, 2016.
- [19] G. Qiao and J. Ou, "Corrosion monitoring of reinforcing steel in cement mortar by EIS and ENA," *Electrochimica Acta*, vol. 52, no. 28, pp. 8008–8019, 2007.
- [20] A. Nishikata, Q. Zhu, and E. Tada, "Long-term monitoring of atmospheric corrosion at weathering steel bridges by an electrochemical impedance method," *Corrosion Science*, vol. 87, pp. 80–88, 2014.
- [21] Y. Chen, F. Tang, Y. Tang, M. J. O'Keefe, and G. Chen, "Mechanism and sensitivity of Fe-C coated long period fiber grating sensors for steel corrosion monitoring of RC structures," *Corrosion Science*, vol. 127, pp. 70–81, 2017.
- [22] S.-G. Dong, C.-J. Lin, R.-G. Hu, L.-Q. Li, and R.-G. Du, "Effective monitoring of corrosion in reinforcing steel in concrete constructions by a multifunctional sensor," *Electrochimica Acta*, vol. 56, no. 4, pp. 1881–1888, 2011.
- [23] G. S. Duffó and S. B. Farina, "Development of an embeddable sensor to monitor the corrosion process of new and existing reinforced concrete structures," *Construction and Building Materials*, vol. 23, no. 8, pp. 2746–2751, 2009.
- [24] A. Legat, "Monitoring of steel corrosion in concrete by electrode arrays and electrical resistance probes," *Electrochimica Acta*, vol. 52, no. 27, pp. 7590–7598, 2007.
- [25] S. Y. Li, Y.-G. Kim, S. Jung, H.-S. Song, and S.-M. Lee, "Application of steel thin film electrical resistance sensor for in situ corrosion monitoring," *Sensors and Actuators B: Chemical*, vol. 120, no. 2, pp. 368–377, 2007.
- [26] V. Maruthapandian, V. Saraswathy, and S. Muralidharan, "Development of solid state embeddable reference electrode for corrosion monitoring of steel in reinforced concrete structures," *Cement and Concrete Composites*, vol. 74, pp. 100–108, 2016.
- [27] S. Muralidharan, V. Saraswathy, L. J. Berchmans, K. Thangavel, and K. Y. Ann, "Nickel ferrite (NiFe_2O_4): a possible candidate material as reference electrode for corrosion monitoring of steel in concrete environments," *Sensors and Actuators B: Chemical*, vol. 145, no. 1, pp. 225–231, 2010.
- [28] T. Parthiban, R. Ravi, and G. T. Parthiban, "Potential monitoring system for corrosion of steel in concrete," *Advances in Engineering Software*, vol. 37, no. 6, pp. 375–381, 2006.
- [29] A. Poursaei, "Automatic system for monitoring corrosion of steel in concrete," *Advances in Engineering Software*, vol. 40, no. 11, pp. 1179–1182, 2009.
- [30] G. Qiao, G. Sun, Y. Hong, Y. Qiu, and J. Ou, "Remote corrosion monitoring of the RC structures using the electrochemical wireless energy-harvesting sensors and networks," *NDT and E International*, vol. 44, no. 7, pp. 583–588, 2011.
- [31] P.-A. Itty, M. Serdar, C. Meral et al., "In situ 3D monitoring of corrosion on carbon steel and ferritic stainless steel embedded in cement paste," *Corrosion Science*, vol. 83, pp. 409–418, 2014.
- [32] A. Brenna, L. Lazzari, and M. Ormellese, "Monitoring chloride-induced corrosion of carbon steel tendons in concrete using a multi-electrode system," *Construction and Building Materials*, vol. 96, pp. 434–441, 2015.
- [33] A. Česen, T. Kosec, and A. Legat, "Characterization of steel corrosion in mortar by various electrochemical and physical techniques," *Corrosion Science*, vol. 75, pp. 47–57, 2013.
- [34] I. Martínez and C. Andrade, "Examples of reinforcement corrosion monitoring by embedded sensors in concrete structures," *Cement and Concrete Composites*, vol. 31, no. 8, pp. 545–554, 2009.
- [35] S. P. Karthick, S. Muralidharan, V. Saraswathy, and K. Thangavel, "Long-term relative performance of embedded sensor and surface mounted electrode for corrosion monitoring of steel in concrete structures," *Sensors and Actuators B: Chemical*, vol. 192, pp. 303–309, 2014.

- [36] L. Daigle, Z. Lounis, and D. Cusson, "Numerical prediction of early-age cracking and corrosion in high performance concrete bridges - case study," in *TAC Annual Conference 2004 - Transportation Innovation-Accelerating the Pace*, pp. 1–20, Quebec City, QC, Canada, 2004.
- [37] P. Goltermann, "Chloride ingress in concrete structures: extrapolation of observations," *ACI Materials Journal*, vol. 100, no. 2, pp. 114–119, 2003.
- [38] Z. Lounis, "Probabilistic modeling of chloride contamination and corrosion of concrete bridge structures," in *Fourth International Symposium on Uncertainty Modeling and Analysis, 2003. ISUMA 2003*, pp. 447–451, College Park, MD, USA, September 2003, IEEE.
- [39] J. Paulsson-Tralla and J. Silfwerbrand, "Estimation of chloride ingress in uncracked and cracked concrete using measured surface concentrations," *ACI Materials Journal*, vol. 99, no. 1, pp. 27–36, 2002.
- [40] T. Maruya, K. Hsu, H. Takeda, and S. Tangtermsirikul, "Numerical modeling of steel corrosion in concrete structures due to chloride ion, oxygen and water movement," *Journal of Advanced Concrete Technology*, vol. 1, no. 2, pp. 147–160, 2003.
- [41] S. C. Kranc and A. A. Sagüés, "Calculation of extended counter electrode polarization effects on the electrochemical impedance response of steel in concrete," in *Electrochemical Impedance: Analysis and Interpretation*, pp. 365–365-19, ASTM International, West Conshohocken, PA, USA, 1993.
- [42] S. C. Kranc and A. A. Sagüés, "Detailed modeling of corrosion macrocells on steel reinforcing in concrete," *Corrosion Science*, vol. 43, no. 7, pp. 1355–1372, 2001.
- [43] A. Sagüés, S. C. Kranc, and B. G. Washington, "Computer modeling of corrosion and corrosion protection of steel in concrete," *Concrete 2000-Economic and Durable Construction through Excellence*, p. 1275, 1993.
- [44] Y. L. Ding, H. W. Zhao, and A. Q. Li, "Temperature effects on strain influence lines and dynamic load factors in a steel-truss arch railway bridge using adaptive FIR filtering," *Journal of Performance of Constructed Facilities*, vol. 31, no. 4, article 04017024, 2017.
- [45] B. Wei, G. L. Dai, Y. Wen, and Y. Xia, "Seismic performance of isolation system of rolling friction with springs," *Journal of Central South University*, vol. 21, no. 4, pp. 1518–1525, 2014.
- [46] K. Kobayashi and K. Shuttoh, "Oxygen diffusivity of various cementitious materials," *Cement and Concrete Research*, vol. 21, no. 2-3, pp. 273–284, 1991.
- [47] A. S. Sudjono and H. Seki, "Experimental and analytical studies on oxygen transport in various cementitious materials," *Special Publication*, vol. 192, pp. 721–738, 2000.
- [48] A. J. M. Siemes, C. Gehlen, A. Lindvall, A. Arteaga, and H. M. Ludwig, *Statistical Quantification of the Variables in the Limit State Functions*, Brite-Euram, Brussels, Belgium, 1999, Summary.
- [49] T. Liu and R. W. Weyers, "Modeling the dynamic corrosion process in chloride contaminated concrete structures," *Cement and Concrete Research*, vol. 28, no. 3, pp. 365–379, 1998.
- [50] K. A. T. Vu and M. G. Stewart, "Structural reliability of concrete bridges including improved chloride-induced corrosion models," *Structural Safety*, vol. 22, no. 4, pp. 313–333, 2000.
- [51] Y. J. Cha, W. Choi, and O. Büyükoztürk, "Deep learning-based crack damage detection using convolutional neural networks," *Computer-Aided Civil and Infrastructure Engineering*, vol. 32, no. 5, pp. 361–378, 2017.
- [52] Y. J. Cha, K. You, and W. Choi, "Vision-based detection of loosened bolts using the Hough transform and support vector machines," *Automation in Construction*, vol. 71, pp. 181–188, 2016.
- [53] Y. Yu, G. Qiao, and J. Ou, "Self-powered wireless corrosion monitoring sensors and networks," *IEEE Sensors Journal*, vol. 10, no. 12, pp. 1901–1902, 2010.
- [54] G. Ye and K. Soga, "Energy harvesting from water distribution systems," *Journal of Energy Engineering*, vol. 138, no. 1, pp. 7–17, 2011.
- [55] A. García and M. N. Partl, "How to transform an asphalt concrete pavement into a solar turbine," *Applied Energy*, vol. 119, pp. 431–437, 2014.
- [56] S. J. Roundy, *Energy Scavenging for Wireless Sensor Nodes with a Focus on Vibration to Electricity Conversion [Ph.D. thesis]*, University of California, Berkeley, Berkeley, CA, USA, 2003.
- [57] F. U. Khan and I. Ahmad, "Review of energy harvesters utilizing bridge vibrations," *Shock and Vibration*, vol. 2016, Article ID 1340402, 21 pages, 2016.
- [58] M. Rhimi and N. Lajnef, "Tunable energy harvesting from ambient vibrations in civil structures," *Journal of Energy Engineering*, vol. 138, no. 4, pp. 185–193, 2012.
- [59] V. Kumar and Remadevi, "Kriging of groundwater levels – a case study," *Journal of Spatial Hydrology*, vol. 6, no. 1, 2006.
- [60] R. J. Hyndman and Y. Khandakar, "Automatic time series forecasting: the forecast package for R," *Journal of Statistical Software*, vol. 27, no. 3, 2008.
- [61] G. N. Flint and R. N. Cox, "The resistance of stainless steel partly embedded in concrete to corrosion by seawater," *Magazine of Concrete Research*, vol. 40, no. 142, pp. 13–27, 1988.
- [62] N. Gartner, T. Kosec, and A. Legat, "Monitoring of the long-term performance of stainless steel reinforcement in saline environments," *BHM Berg- und Hüttenmännische Monatshefte*, vol. 161, no. 1, pp. 44–49, 2016.

Research Article

Neck Flexion Angle Estimation during Walking

Duc Cong Dang,¹ Quoc Khanh Dang,² Young Joon Chee,³ and Young Soo Suh¹

¹Electrical Engineering Department, University of Ulsan, Ulsan, Republic of Korea

²NAMU Inc., Ulsan, Republic of Korea

³Biomedical Engineering Department, University of Ulsan, Ulsan, Republic of Korea

Correspondence should be addressed to Young Soo Suh; yssuh@ulsan.ac.kr

Received 8 June 2017; Accepted 19 October 2017; Published 28 December 2017

Academic Editor: Yeeseok Kim

Copyright © 2017 Duc Cong Dang et al. This is an open access article distributed under the Creative Commons Attribution License, which permits unrestricted use, distribution, and reproduction in any medium, provided the original work is properly cited.

Neck pain is recently known as the fourth leading cause of disability and the number of patients is apparently increasing. By analyzing the effect of gravitational force on inertial sensor attached to the neck, this study aims to investigate the head flexion posture during walking. The estimated angle is compared with the craniovertebral angle which is measured with an optical tracker. A total of twenty subjects with no history of neck pain or discomfort were examined by walking on the treadmill inside the working range of an optical tracker. In our laboratory settings, the neck flexion angle (NFA) may have a linear relationship with the craniovertebral angle (CVA) in both static case and constant speed walking case. Therefore, inertial sensor, which is lightweight, low cost, and especially free in movement, can be used instead of a camera system. Our proposed estimation method shows its flexibility and gives a result with the mean of absolute error of estimated neck angle varying from 0.48 to 0.58 degrees, which is small enough to use in applications.

1. Introduction

Neck pain is one of the most common musculoskeletal disorders (MSDs) among both the general and working population, with an annual prevalence rate exceeding 30%, and the literature is mixed as to whether it peaks or plateaus in middle age [1]. According to [2], the head in normal posture weighs about 10 to 12 lbs., but when the head flexed forward, the force seen by the neck increases to 27 lbs. at 15°, 40 lbs. at 30°, 49 lbs. at 45°, and 60 lbs. at 60°. That huge amount of force increases loading in the joints and muscles of the cervical spine and can be a major contribution factor to neck and upper limb disorders after a prolonged period of time [3].

Recent studies show greater interest in the relationship between neck pain and digital devices, using situations such as computers at the workplace [3, 4] or handheld devices [5–7]. The widespread use of digital technology, including computers and mobile devices, is related to the prevalence of neck pain due to the head forward flexion posture. Users

tend to maintain their poor head posture even with the existence of pain symptoms or neck discomfort [5].

Besides neck pain, it is said that pedestrians may face some risk while walking or crossing road since they tend to miss visual targets or sound indications when looking down the smartphone [8, 9]. Therefore, it is important to investigate the head flexion posture during user walking.

The neck flexion angle (NFA) can be estimated by using force sensors placed on the front, left, and back side of the neck [10] or camera systems to observe the craniovertebral angle (CVA) using infrared markers attached on the neck [11, 12]. Another effective way to measure the neck flexion angle was proposed by using motion sensors to analyze the gravitational force placed on the neck [13, 14]. In previous studies, the neck flexion angle is estimated for static pose such as standing or sitting down. In this study, we used an inertial sensor to estimate the neck flexion angle (NFA) during walking. OptiTrack camera system is used to obtain the craniovertebral angle (CVA), which is used as ground truth value for the analysis. A preliminary result

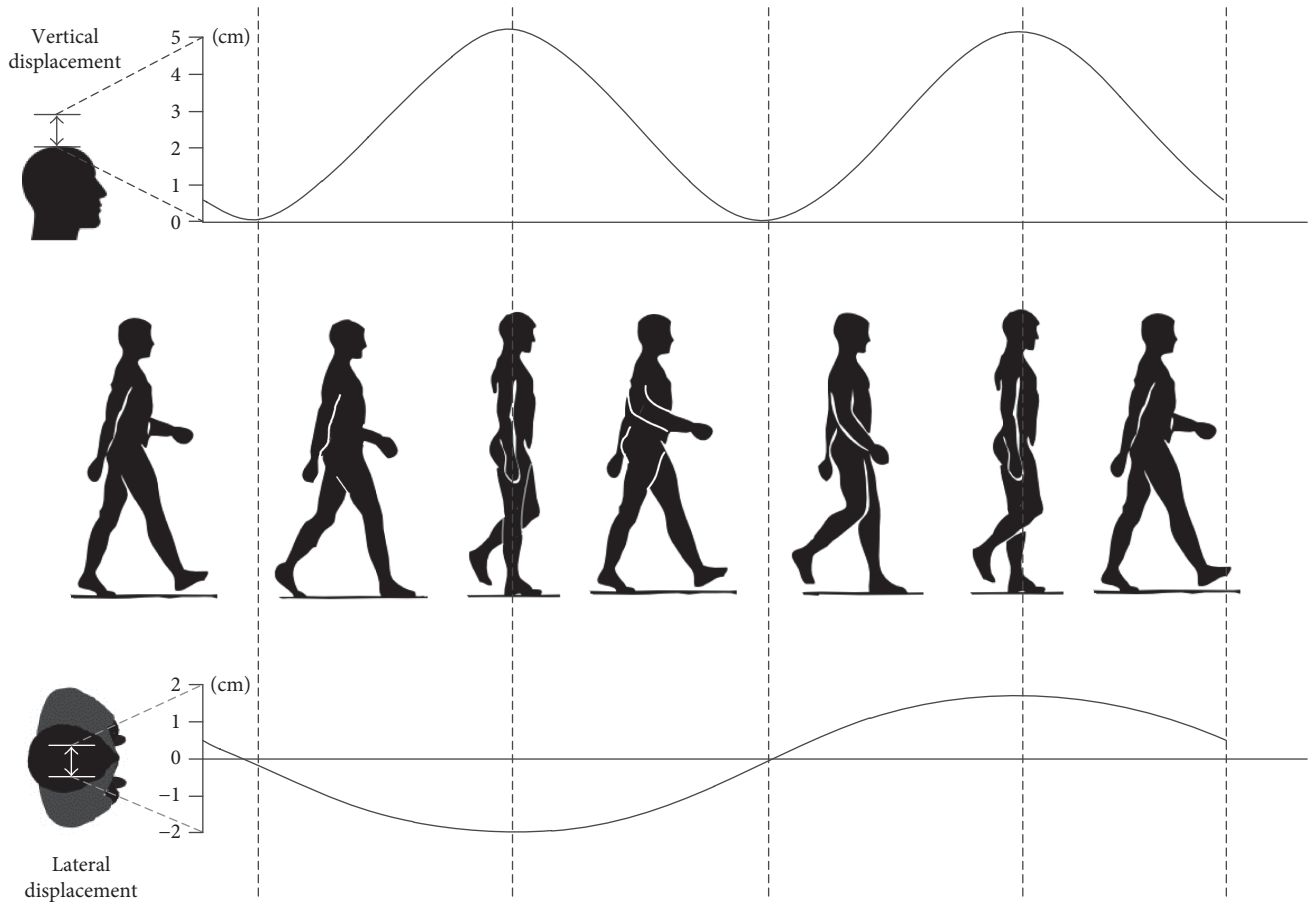


FIGURE 1: Vertical and lateral displacements of human gait.

was presented in the conference paper [15], where a basic algorithm is given without experimental verification.

2. Methods

The neck posture in this paper is estimated by analyzing the gravitational force placed on the neck using an accelerometer. During walking, the estimation is affected heavily by the walking movement since the accelerometer observes not only the gravitational force but also the external acceleration. The walking movement will be analyzed in this section together with the step detecting algorithm to propose a novel method for detecting neck angle during walking.

2.1. Human Gait Analysis. Human gait refers to locomotion achieved through the movement of human limb. During walking, the center of mass moves along the travelling direction but also has sinusoidal movements in the lateral and vertical direction [16]. The result in [16] also showed that the lateral and vertical displacements depend on the walking speed. When the nominal speed increases, the lateral displacement decreases while the vertical displacement tends to increase. However, according to a recorded data using VICON camera system from Carnegie Mellon University [17], the vertical and lateral translations are still in sinusoidal

forms where the vertical movement frequency is double the lateral movement frequency.

The human gait analysis can be seen from Figure 1. As the lower limbs act like inverted pendulums while walking, the center of mass of a pedestrian moves in sinusoidal wave form with respect to the sagittal plane. The maximum vertical displacement is around 30% and 80% of gait cycle when one leg is at mid-stance and mid-swing positions, respectively. In the meantime, the sinusoidal form of the lateral displacement is caused by the changing of center of mass onto each foot while walking. The minimum of the lateral displacement is at 30% of the gait cycle while its maximum is at 80% of the gait cycle.

Based on this fact, a simulated movement can be generated as in Figure 2 where the forward movement is assumed to be linear. To verify the theory, a real data of a walking person was recorded. In this record, an accelerometer was attached on a volunteer's neck so that the x -axis of the accelerometer points upward while the z -axis of the accelerometer coincides with the walking direction. Since we are only interested in the form of the signal, the accelerometer outputs were filtered as can be seen from Figure 2(b). The result showed that while walking, the acceleration of the pedestrian's neck movement has both vertical and lateral accelerations in sinusoidal forms, in which the frequency of the later acceleration is twice that of the vertical acceleration.

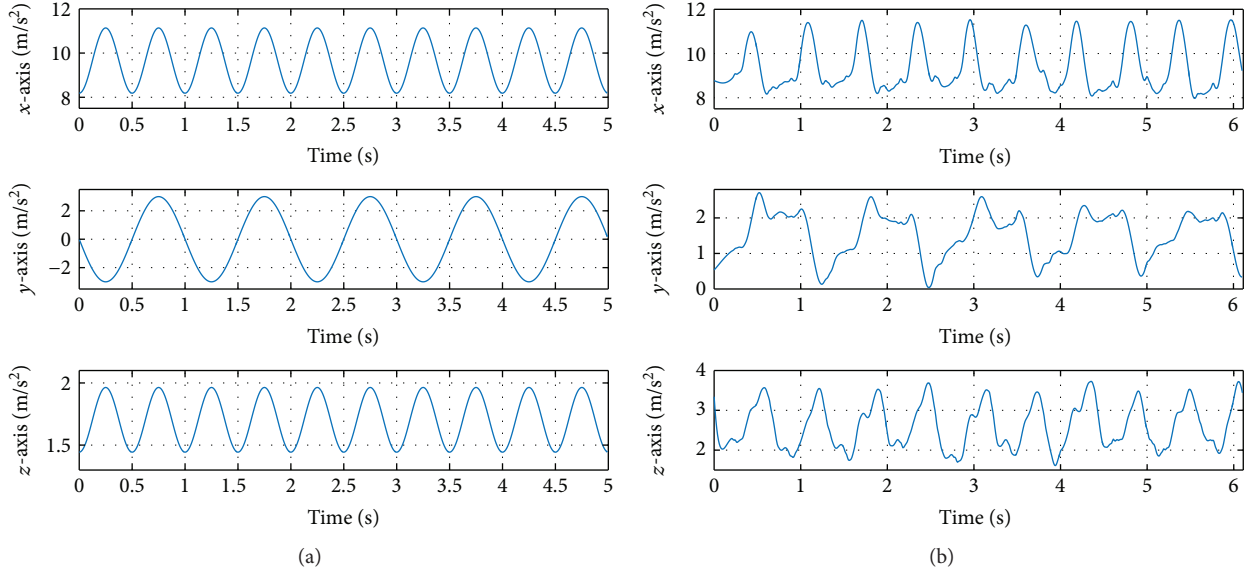


FIGURE 2: Simulated and real filtered accelerations of walking data: (a) simulated data; (b) real filtered data.

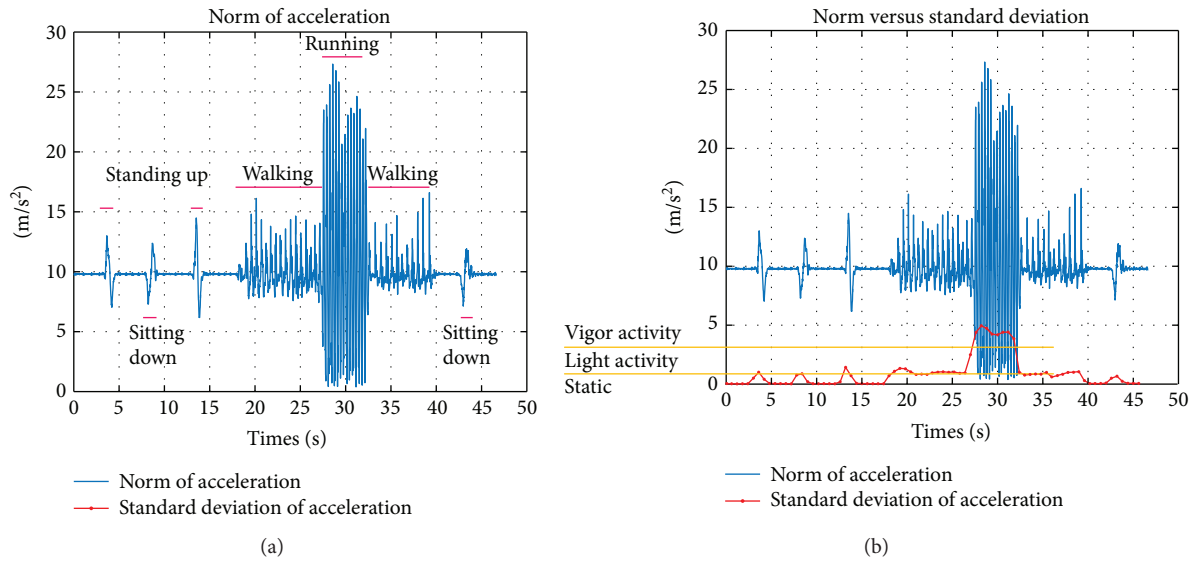


FIGURE 3: Activity classification using an accelerometer: (a) norm of acceleration; (b) norm and standard deviation of acceleration.

As can be seen from Figure 2, the peaks of the vertical acceleration were produced by the shocks yielded at the heel strike periods of the gait cycle. Based on these peaks, the steps can be detected. Since in each step the accelerations in vertical and lateral directions are close to sinusoidal forms and the forward acceleration is approximated to zero (linear forward walking), the external accelerations will be eliminated by summing the acceleration values in each axis. Or in other words, the sum of the acceleration in the x - and z -axes in each step represents the gravitational force acting upon the pedestrian's neck. By only measuring the gravitational force, the accelerometer estimates the inclination angle of the accelerometer with respect to the ground using a triad algorithm given in [18]. This inclination is also the neck angle. Therefore, to cancel out the external acceleration, a step detection algorithm is needed.

2.2. Step Detection Algorithm. As mentioned above, the estimation of the neck angle is heavily affected by the external acceleration. In the first step, we aim to classify the human activities into dynamic and static cases using standard deviation of the acceleration as the main classification criteria. The standard deviation σ_a of norm acceleration data set a_i ($1 \leq i \leq N$, N is the number of samples) is calculated as follows:

$$\sigma_a = \sqrt{\frac{1}{N} \sum_{i=1}^N (a_i - \mu)^2}, \quad (1)$$

where $\mu = (1/N) \sum_{i=1}^N a_i$ is the mean value of data set a_i .

By applying the standard deviation parameter to acceleration norm data, some human activities can be easily detected as an example in Figure 3, where a sequence

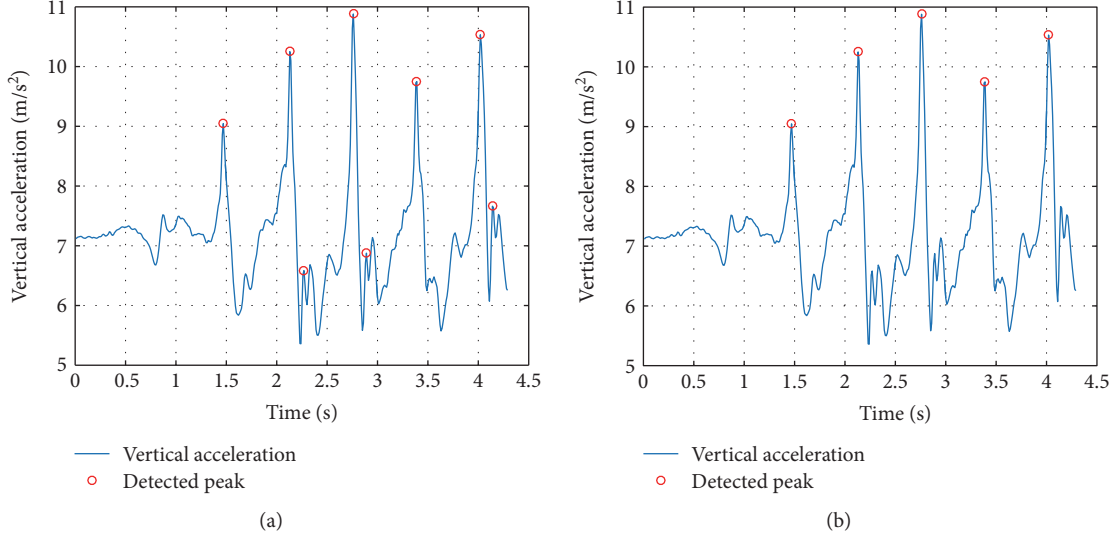


FIGURE 4: Peak detection of real walking data: (a) all peaks; (b) heel strike peaks.

data of sitting–standing up–standing–sitting down–sitting–standing up–standing–walking–running–walking–standing–sitting down–sitting was recorded.

It is easy to classify the light activity among various activity and static cases. In this experiment, the parameters to detect static and vigor activity are 0.1 and 2, respectively. Other actions such as sitting down and standing up have the same standard deviation with walking but it can be eliminated since they happen in a short time while walking activity is periodic and occurs in a long time. Our next step is to detect the walking steps based on characteristics of walking activity (long and periodic occurrence).

There are many algorithms for step detection such as threshold level [19–21], spectral analysis [22], or peak detections. The threshold-based method in [19–21] detects a walking step when the acceleration value is larger than a threshold level. This method is simple but sensitive to noise since other acceleration could cause a fluctuation in the output of the sensor. Spectral analysis in [22] is robust to noise but has a large computational load.

To provide an online step detection that can run on low speed and limited memory processors, we propose a simple peak detection algorithm using five consecutive data points.

Let $y_i \in \mathbb{R}$ be a signal from the output of the sensor at the discrete time i . Since we are only interested in detecting the peak of the signal rather than its true values, y_i is filtered by a simple three-point weighted moving average:

$$\bar{y}_i = \alpha_1 y_{i-1} + (1 - 2\alpha_1) y_i + \alpha_1 y_{i+1}, \quad (2)$$

where α_1 is the weighting factor for the low-pass filter. The significant maximum peak at the discrete time i

will be detected if one of the following conditions is satisfied:

$$\begin{aligned} & \bar{y}_{i-2} < \bar{y}_i, \\ & \bar{y}_{i-1} < \bar{y}_i, \\ & \bar{y}_i > \bar{y}_{i+1}, \\ & \bar{y}_i > \bar{y}_{i+2}, \\ & \bar{y}_i - \max(\bar{y}_{i-2}, \bar{y}_{i-1}, \bar{y}_{i+1}, \bar{y}_{i+2}) > \alpha_2, \\ & \bar{y}_{i-3} < \bar{y}_{i-2}, \\ & \bar{y}_{i-2} < \bar{y}_{i-1}, \\ & \bar{y}_{i-1} < \bar{y}_i, \\ & \bar{y}_i > \bar{y}_{i+1}, \\ & \bar{y}_i - \max(\bar{y}_{i-3}, \bar{y}_{i-2}, \bar{y}_{i-1}, \bar{y}_{i+1}) > \alpha_2, \\ & \bar{y}_{i-1} < \bar{y}_i, \\ & \bar{y}_i > \bar{y}_{i+1}, \\ & \bar{y}_{i+1} > \bar{y}_{i+2}, \\ & \bar{y}_{i+2} > \bar{y}_{i+3}, \\ & \bar{y}_i - \max(\bar{y}_{i-1}, \bar{y}_{i+1}, \bar{y}_{i+2}, \bar{y}_{i+3}) > \alpha_2, \end{aligned} \quad (3)$$

where α_2 is a threshold parameter. The sensitivity of the peak detection algorithm can be adjusted by changing the value of α_2 . If α_2 is chosen as a large value, small peaks due to noise can be ignored. However, only conspicuous peaks can be recognized. This also means that some true peaks may not be detected.

Although all peaks are detected, there might be a chance that the peak is caused by other activities or noises rather than walking. For example, as can be seen from Figure 4(a) where an extraction of a fast walking data is from an accelerometer attached on a person's neck, if only the conditions in

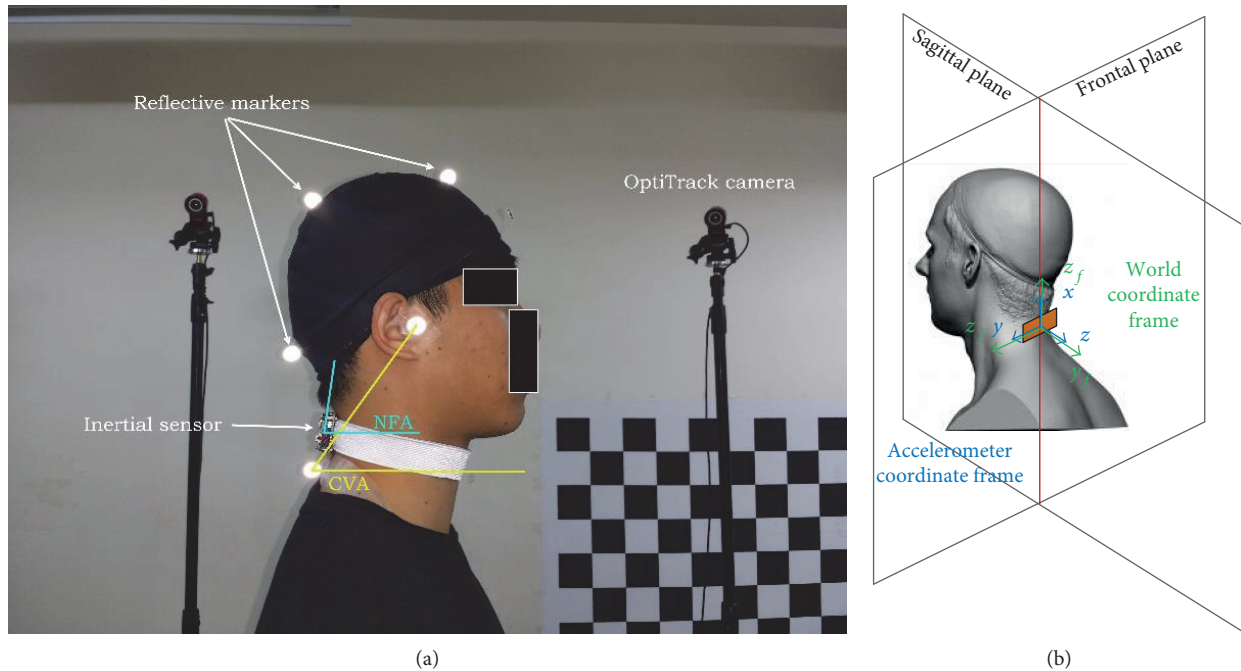


FIGURE 5: (a) Reflective markers and inertial sensor position while standing upright inside the working range of infrared camera system; (b) sensor and world coordinate frames used in this paper.

(3) are used, we obtain many peaks. Fortunately, peaks caused by the contacting shock at heel strike moments are much larger than other peaks and these peaks occur periodically. Based on this fact, we propose to detect the heel strike peaks by searching one large peak within a specific time α_3 . In detail, when a peak is detected at the time i using conditions in (3), all surrounding peaks in the range of $[i - \alpha_3, i + \alpha_3]$ are compared together. The largest value will be the true peak generated by a heel strike. By using this method, periodic peaks will be selected.

The result of applying α_3 condition is given in Figure 4(b) where all walking peaks are successfully detected. If α_3 is too large, some steps will be missed. Conversely, if we set α_3 as a small value, some peaks caused by noises will be wrongly detected as the walking peaks. However, the maximum value of α_3 can be chosen from 0.4 to 0.6 sec since the normal and fast walking speeds of a pedestrian is 100 and 150 steps per minute [23, 24], respectively. In this experiment, α_3 is chosen to be 0.4 sec.

The walking activity is only defined when at least three consecutive walking peaks are detected. Let T_j be the time interval between two consecutive peaks at $t_{i-1,j}$ and $t_{i,j}$ from N peaks ($1 \leq j \leq N$):

$$T_j = t_{i,j} - t_{i-1,j}. \quad (4)$$

Since walking activity is nearly periodic, the following condition will be satisfied:

$$\left| T_j - \frac{1}{N} \sum_{k=1}^N T_k \right| \leq \alpha_4. \quad (5)$$

If small α_4 is chosen, we obtain very periodic walking steps but the walking activity may fail to be detected since naturally not all strike cycles are the same. In contrast, if a larger α_4 is used, we have a more flexible condition in detecting walking activity. However, there could be a chance that some of the detected peaks are not the walking steps.

2.3. Neck Flexion Angle Estimation. The neck flexion angle (NFA), which is the angle of neck flexion relative to horizontal direction, is estimated by observing the angle between vertical direction and the projection of the gravitational force on the z -axis of the accelerometer. The accelerometer was attached on the body neck as shown in Figure 5(b) where its x -axis points upward and its z -axis is perpendicular to the neck when the neck is up straight. The world coordinate frame was chosen so that its z -axis is upward, while the x - and y -axes can be chosen arbitrarily. When the neck is bended, the inclination angle of the neck can be calculated by using the following equation [25]:

$$\beta = \tan^{-1} \frac{a_x}{\sqrt{a_y^2 + a_z^2}}, \quad (6)$$

where $a = [a_x \ a_y \ a_z]^T \in \mathbb{R}^3$ is the output of the accelerometer.

Equation (6) is only applied for static cases where the external accelerations are absent. In walking scene, the external due to walking activity is considerable. As can be seen from Figure 1 and Figure 2(b), the projection of the gravitational force on the x - and z -axes of the accelerometer are sinusoidal in each walking step. Since x -axis of the

TABLE 1: CVA and NFA in static case (unit: degrees).

| Static case | 10 sec no change | Level 1 | Level 2 | Level 3 | Level 4 | Level 5 |
|------------------|------------------|---------|---------|---------|---------|---------|
| Mean (NFA) | 83.6211 | 82.4773 | 76.2310 | 66.1847 | 58.4557 | 45.9955 |
| Mean (CVA) | 49.3835 | 48.5494 | 40.7722 | 30.2919 | 22.7974 | 9.2151 |
| Mean (NFA – CVA) | 34.2376 | 33.9280 | 35.4588 | 35.8928 | 35.6582 | 36.7804 |
| Var (NFA – CVA) | 0.0632 | 0.0461 | 0.0518 | 0.0273 | 0.0340 | 0.0681 |

accelerometer points upward while its z -axis is on walking direction, the inclination on the neck in each walking step can be estimated using the following equation:

$$\beta = \tan^{-1} \frac{\bar{a}_x}{\bar{a}_z}, \quad (7)$$

where \bar{a}_x and \bar{a}_z are the average value of accelerometer output in the x and z direction within each walking step, respectively.

3. Experiments

A total of 20 subjects, ranging from 24 to 32 years old with the mean age of 26.8, were recruited for the study. All participants had no difficulties in using smartphones while standing or walking and had at least 15 minutes walking to be familiar with the treadmill (running machine).

We conducted all trials with participants in two separated experiments.

During the whole process, subjects were asked to wear a swimming cap having three reflective markers attached in the sagittal plane parallel to the direction of view. Two more markers were placed on the skin at the position of C7 bone and tragus.

An Xsens MTi1 sensor with the customized board having Bluetooth communication was put on subjects' neck using an elastic band. Both two experiments were conducted inside the working range of 6 cameras in the OptiTrack infrared camera system (Figure 5(a)). The system was configured to extract 3D position data of the markers, 3-axis acceleration, and angular velocity of the inertial sensor at the sampling rate of 100 Hz.

At the beginning of the first experiment, each subject's data was recorded while they were standing up straight (upright position) as they usually did for 10 seconds. Then each participant intentionally performed "text-neck" posture [26] changes with 5 levels from upright position and the lowest position within about 10 seconds each. These levels were chosen by each subject, whichever make themselves comfortable.

Before the second experiment started, participants were asked to get acquainted with different speed levels of the treadmill. Each subject then sequentially performed walking tasks with regular constant walking speed of 3, 4, and 5 km/h. During each task, the subject also did the 5 levels of "text-neck" changes, each level within 30 seconds. At least 30 seconds of rest break was given after finishing each task to minimize the risk of neck pain.

Position data of markers and output of inertial sensor were synchronized before using for analysis. The craniocervical angle (CVA) and the neck flexion angle (NFA or the neck angle) can be derived using the following procedure:

- (a) The CVA, which is the angle between a line connecting C7 to tragus and the horizontal line through the spinous process of C7 [27] can be calculated by projection of both C7 and tragus markers into the sagittal plane.
- (b) The neck angle NFA in the static pose can be calculated by observing the angle between the vertical direction and the projection of the gravitational force at each sample of time on the z -axis of the accelerometer using (6), which is called "direct computation method." However, in the walking case, the center of mass has sinusoidal movements in lateral and vertical direction [16], the external acceleration in that two directions are close to sinusoidal forms. The forward acceleration is approximately zero (linear forward walking), then we can eliminate the external accelerations by summing the accelerometer output in each axis within each walking step, and the inclination angle with respect to the ground can be calculated using (7).

To evaluate the relationship between the CVA and the NFA, we inspected the mean and variation of the difference between that two angles. Our estimation algorithm performance is also examined by comparing with the "direct computation method" and "fixed interval average method," where the acceleration data in each axis is summed over a fixed period. We chose that fixed interval to be 0.5, 0.75, and 1 second due to the common walking step time.

4. Results and Discussions

The main contributions of this study include the relationship between CVA and NFA in both static and walking cases. The experimental results of a subject showed in Tables 1 and 2 imply that the estimated neck angles (NFA) have a linear relationship with the CVA, where there is a "nonchanging" offset value between the two angles in both static and walking cases. Also in Figure 6, we can clearly see the similar trends and amount of changes between different levels among these angles. It means the NFA, which can be derived by our simple, flexible, and cost-effective method, can be used instead of the CVA in applications, and from the estimated angle and a calibration step, the true neck angle can be

TABLE 2: CVA and NFA in walking case (unit: degrees).

| Walking case | | Level 1 | Level 2 | Level 3 | Level 4 | Level 5 |
|--------------|------------------|---------|---------|---------|---------|---------|
| 3 km/h | Mean (NFA) | 81.4722 | 74.4427 | 71.6546 | 65.7486 | 58.8117 |
| | Mean (CVA) | 45.3579 | 37.3134 | 34.1081 | 28.1364 | 21.5184 |
| | Mean (NFA – CVA) | 36.1144 | 37.1292 | 37.5465 | 37.6123 | 37.2933 |
| | Var (NFA – CVA) | 0.3312 | 0.1863 | 0.1491 | 0.3100 | 0.5335 |
| 4 km/h | Mean (NFA) | 82.7458 | 75.8507 | 69.3977 | 65.0855 | 60.2854 |
| | Mean (CVA) | 46.0182 | 38.7697 | 31.8672 | 27.5250 | 22.9371 |
| | Mean (NFA – CVA) | 36.7277 | 37.0810 | 37.5305 | 37.5605 | 37.3483 |
| | Var (NFA – CVA) | 0.9034 | 0.4096 | 0.7186 | 0.8024 | 0.5123 |
| 5 km/h | Mean (NFA) | 82.0928 | 74.7623 | 69.1052 | 64.1363 | 58.7212 |
| | Mean (CVA) | 45.9104 | 37.4357 | 31.0791 | 26.0616 | 21.2336 |
| | Mean (NFA – CVA) | 36.1824 | 37.3266 | 38.0261 | 38.0747 | 37.4876 |
| | Var (NFA – CVA) | 0.2328 | 0.3207 | 0.1990 | 0.4291 | 0.6641 |

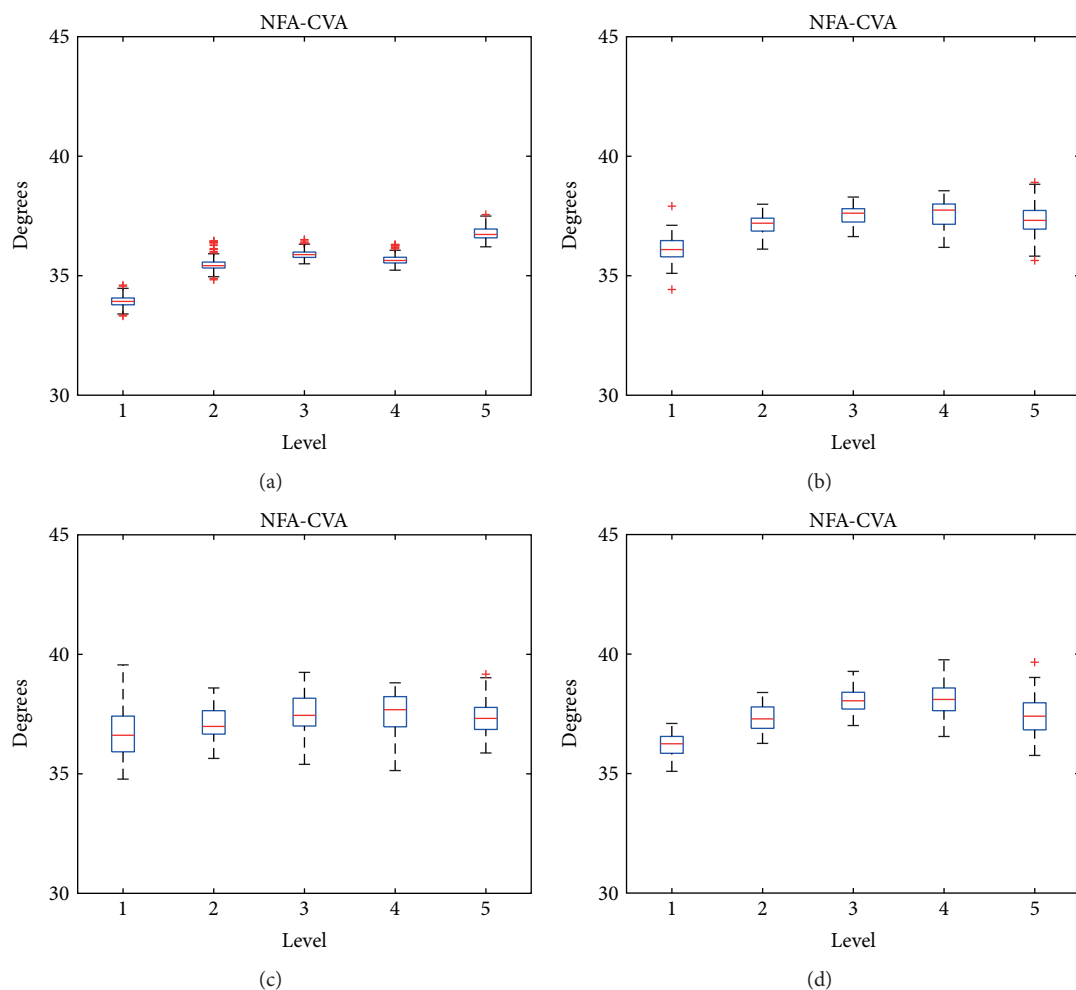


FIGURE 6: Relationship between CVA and NFA in (a) static case; (b) 3 km/h walking; (c) 4 km/h walking; (d) 5 km/h walking.

derived. The calibration step can be done using the following simple process:

- (a) The calibrated angle is obtained when the candidate sits upright.
- (b) This upright angle is assumed to be 90 degrees for the estimated neck angle at that moment.
- (c) The difference between the real estimated and upright angle is added into each estimated neck angle value.

TABLE 3: Mean of absolute error of the estimated neck angle after calibration steps (unit: degrees).

| Walking case | Direct computation method | Fixed interval $T = 0.5$ sec | Fixed interval $T = 0.75$ sec | Fixed interval $T = 1$ sec | Proposed flexible interval | |
|--------------|---------------------------|---------------------------------|----------------------------------|-------------------------------|----------------------------|---------------|
| 3 km/h | Level 1 | 1.8637 | 0.5419 | 0.5403 | 0.4982 | 0.4836 |
| | Level 2 | 1.8715 | 0.5579 | 0.5356 | 0.4999 | 0.4826 |
| | Level 3 | 1.7772 | 0.5449 | 0.4932 | 0.4780 | 0.4545 |
| | Level 4 | 1.8539 | 0.5632 | 0.5650 | 0.4928 | 0.4793 |
| | Level 5 | 2.0296 | 0.6462 | 0.6297 | 0.5337 | 0.5074 |
| | Mean | 1.8792 | 0.5708 | 0.5528 | 0.5005 | 0.4815 |
| 4 km/h | Level 1 | 2.4324 | 0.7696 | 0.7460 | 0.8390 | 0.6590 |
| | Level 2 | 2.2248 | 0.6280 | 0.6395 | 0.5494 | 0.5222 |
| | Level 3 | 2.2666 | 0.7383 | 0.6646 | 0.6376 | 0.5636 |
| | Level 4 | 2.2077 | 0.8018 | 0.5846 | 0.6797 | 0.5552 |
| | Level 5 | 2.2607 | 0.6116 | 0.6482 | 0.6276 | 0.5534 |
| | Mean | 2.2784 | 0.7099 | 0.6566 | 0.6667 | 0.5707 |
| 5 km/h | Level 1 | 2.6015 | 0.5970 | 0.6359 | 0.5893 | 0.5434 |
| | Level 2 | 2.5488 | 0.6479 | 0.6007 | 0.5484 | 0.5537 |
| | Level 3 | 2.3671 | 0.5444 | 0.5038 | 0.5273 | 0.4856 |
| | Level 4 | 2.3915 | 0.5932 | 0.6272 | 0.6478 | 0.5585 |
| | Level 5 | 2.5111 | 0.6832 | 0.6684 | 0.7290 | 0.5866 |
| | Mean | 2.4840 | 0.6131 | 0.6072 | 0.6084 | 0.5456 |

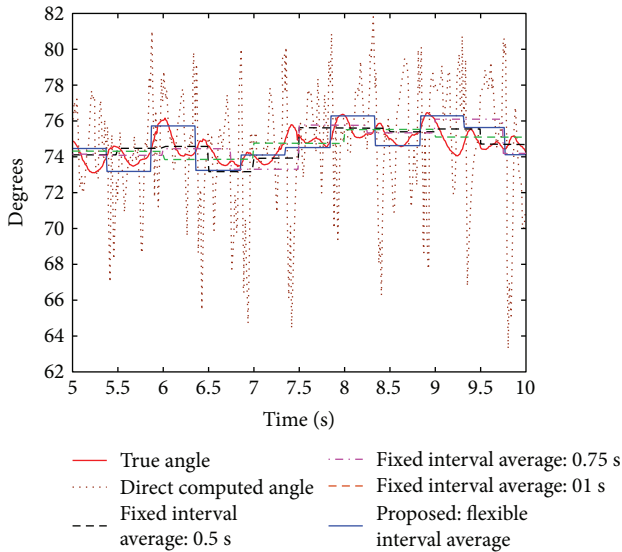


FIGURE 7: Estimated neck angle of different methods at 3 km/h.

Experiment data from all candidates were also included to examine the performance of our proposed neck angle estimation method. Table 3 shows the mean of absolute errors of the estimated neck angle which belong to the “direct computation method” (calculate angles at each sample of data), our proposed walking step time-based “flexible interval average method” (calculate angles based on average of acceleration between consecutive walking steps), and the “fixed interval average method” (calculate angles based on average of acceleration during a fixed time interval of 0.5,

0.75, and 1 second). The true neck flexion angle (NFA) was obtained through a calibration step from the craniovertebral angle (CVA) measured by OptiTrack camera system. An example of visual comparison between methods above is presented in Figure 7.

The result from Table 3 shows that our proposed method provides better result in all contexts in comparison with others. More specifically, the “direct computation method” at each sample of data gives an acceptable result with mean of absolute error of estimated angle varying from 1.88 to 2.49 degrees. Since the external accelerations in forward and vertical directions can be canceled out by taking average in each walking step, our proposed method presents better result in comparison to other methods with mean of absolute error from 0.48 to 0.57 degrees. Moreover, the walking step length and the human gait while walking at each speed are personal dependent parameters, and the proposed method shows its flexibility that we can use for personal independent parameters.

Conflicts of Interest

The authors declare no conflict of interest.

Authors' Contributions

Duc Cong Dang, Quoc Khanh Dang, Young Joon Chee, and Young Soo Suh conceived and designed this study. Duc Cong Dang and Quoc Khanh Dang performed the experiments. Duc Cong Dang wrote the paper. Young Soo Suh reviewed and edited the manuscript.

Acknowledgments

This work was supported by National Research Foundation of Korea grant funded by the Korean Government (no. 2016R1D1A1A09918657).

References

- [1] S. P. Cohen, "Epidemiology, diagnosis, and treatment of neck pain," *Mayo Clinic Proceedings*, vol. 90, no. 2, pp. 284–299, 2015.
- [2] K. K. Hansraj, "Assessment of stresses in the cervical spine caused by posture and position of the head," *Surgical Technology International*, vol. 25, pp. 277–279, 2014.
- [3] G. P. Szeto, L. Straker, and S. Raine, "A field comparison of neck and shoulder postures in symptomatic and asymptomatic office workers," *Applied Ergonomics*, vol. 33, no. 1, pp. 75–84, 2002.
- [4] L. Korpinen, R. Paakkonen, and F. Gobba, "Self-reported neck symptoms and use of personal computers, laptops and cell phones among Finns aged 18–65," *Ergonomics*, vol. 56, no. 7, pp. 1134–1146, 2013.
- [5] J. E. Gold, J. B. Driban, N. Thomas, T. Chakravarty, V. Channell, and E. Komaroff, "Postures, typing strategies, and gender differences in mobile device usage: an observational study," *Applied Ergonomics*, vol. 43, no. 2, pp. 408–412, 2012.
- [6] X. Guan, G. Fan, Z. Chen et al., "Gender difference in mobile phone use and the impact of digital device exposure on neck posture," *Ergonomics*, vol. 59, no. 11, pp. 1453–1461, 2016.
- [7] S. Lee, H. Kang, and G. Shin, "Head flexion angle while using a smartphone," *Ergonomics*, vol. 58, no. 2, pp. 220–226, 2015.
- [8] C. H. Basch, D. Ethan, P. Zybert, and C. E. Basch, "Pedestrian behavior at five dangerous and busy Manhattan intersections," *Journal of Community Health*, vol. 40, no. 4, pp. 789–792, 2015.
- [9] S. Haga, A. Sano, Y. Sekine, H. Sato, S. Yamaguchi, and K. Masuda, "Effects of using a smart phone on pedestrians' attention and walking," *Procedia Manufacturing*, vol. 3, pp. 2574–2580, 2015.
- [10] C. Demmans, S. Subramanian, and J. Titus, "Posture monitoring and improvement for laptop use," in *In CHI '07 Extended Abstracts on Human Factors in Computing Systems*, pp. 2357–2362, ACM, San Jose, CA, USA, 2007.
- [11] L. M. Straker, J. Coleman, R. Skoss, B. A. Maslen, R. Burgess-Limerick, and C. M. Pollock, "A comparison of posture and muscle activity during tablet computer, desktop computer and paper use by young children," *Ergonomics*, vol. 51, no. 4, pp. 540–555, 2008.
- [12] J. G. Young, M. Trudeau, D. Odell, K. Marinelli, and J. T. Dennerlein, "Touch-screen tablet user configurations and case-supported tilt affect head and neck flexion angles," *Work*, vol. 41, no. 1, pp. 81–91, 2012.
- [13] S. Jeong, T. Song, H. Kim, M. Kang, K. Kwon, and J. W. Jeon, "Human neck's posture measurement using a 3-axis accelerometer sensor," in *Computational Science and its Applications - ICCSA 2011: International Conference*, pp. 96–109, Santander, Spain, June 2011, Proceedings, part V.
- [14] P. P. Breen, A. Nisar, and G. O'laighin, "Evaluation of a single accelerometer based biofeedback system for real-time correction of neck posture in computer users," *2009 Annual International Conference of the IEEE Engineering in Medicine and Biology Society*, 2009, pp. 7269–7272, Minneapolis, MN, USA, 2009.
- [15] D. C. Dang, Q. K. Dang, Y. J. Chee, and Y. S. Suh, "Motion sensor based neck posture estimation during walking," in *Proceedings of 22nd International Symposium on Artificial Life and Robotics (AROB)*, pp. 904–908, Beppu, Japan, January 2017.
- [16] M. S. Orendurff, A. D. Segal, G. K. Klute, J. S. Berge, E. S. Rohr, and N. J. Kadel, "The effect of walking speed on center of mass displacement," *Journal of Rehabilitation Research & Development*, vol. 41, no. 6, pp. 829–834, 2004.
- [17] Carnegie Mellon University, "Cmu graphics lab motion capture database," NSF Grant #0196217, May 2017, <http://mocap.cs.cmu.edu>.
- [18] H. D. Black, "A passive system for determining the attitude of a satellite," *AIAA Journal*, vol. 2, no. 7, pp. 1350–1351, 1964.
- [19] Y. W. Bai, C. H. Yu, and S. C. Wu, "Using a three-axis accelerometer and gps module in a smart phone to measure walking steps and distance," in *Electrical and Computer Engineering (CCECE), 2014 IEEE 27th Canadian Conference*, pp. 1–6, Toronto, ON, Canada, May 2014.
- [20] T. Kinh, L. Tu, and D. Tien, "A high-accuracy step counting algorithm for iphones using accelerometer," in *2012 IEEE International Symposium on Signal Processing and Information Technology (ISSPIT)*, pp. 213–217, Ho Chi Minh City, Vietnam, 2012.
- [21] M. Yamamoto and E. Kamioka, "Location Estimation System using Acceleration Sensor," *The Institute of Electronics, Information, and Communication Engineers Technical Report, Mobile Network and Applications*, vol. 110, no. 40, pp. 139–144, 2010.
- [22] H. Ookura, H. Yamamoto, and K. Yamazaki, "Development and evaluation of walking path estimation system using sensors of android device and vector map matching," in *The International Conference on Information Network*, pp. 25–29, Bali, Indonesia, February 2012.
- [23] M. Stanten, "Stepping up fitness: walking 5 miles a day is easier than you think!," November 2011, <https://www.prevention.com/fitness/fitness-tips/stepping-fitness>.
- [24] S. J. Marshall, S. S. Levy, C. E. Tudor-Locke et al., "Translating physical activity recommendations into a pedometer-based step goal: 3000 steps in 30 minutes," *American Journal of Preventive Medicine*, vol. 36, no. 5, pp. 410–415, 2009.
- [25] K. Tuck, *Tilt Sensing Using Linear Accelerometers*, Freescale Semiconductor: Application Note AN3461, Tempe, AZ, 2007.
- [26] S. Shoshany, "A Modern Spine Ailment: Text Neck," November 2015, <http://www.spine-health.com/blog/modern-spine-ailment-text-neck>.
- [27] P. Nejati, S. Lotfian, A. Moezy, A. Moezy, and M. Nejati, "The relationship of forward head posture and rounded shoulders with neck pain in Iranian office workers," *Medical Journal of the Islamic Republic of Iran*, vol. 28, p. 26, 2014.

Research Article

Impedance Based Health Monitoring Technique with Probabilistic Neural Network for Possible Wall Thinning Detection of Metal Structures

Wongi S. Na¹ and Jongdae Baek²

¹Future Strategy & Convergence Research Institute, Korea Institute of Civil Engineering & Building Technology, Gyeonggi-do 10223, Republic of Korea

²Highway & Transportation Research Institute, Korea Institute of Civil Engineering & Building Technology, Gyeonggi-do 10223, Republic of Korea

Correspondence should be addressed to Wongi S. Na; wongi84@naver.com

Received 18 July 2017; Accepted 27 August 2017; Published 9 October 2017

Academic Editor: Young-Jin Cha

Copyright © 2017 Wongi S. Na and Jongdae Baek. This is an open access article distributed under the Creative Commons Attribution License, which permits unrestricted use, distribution, and reproduction in any medium, provided the original work is properly cited.

Corrosion of structures and wall thinning of pipes can severely affect the mechanical strength as wall thickness is reduced. Thus a cost effective structural health monitoring technique plays an important role when managing a structure. The electromechanical impedance (EMI) method is a local method that has limited sensing range, resulting in a high cost when covering large areas. In this study, a reattachable EMI method is investigated using a stack of multiple metal plates to conduct an experiment involving thickness reduction. In addition, the main problem of the impedance signatures changing subjected to reattaching the piezoelectric transducer is solved by using the probabilistic neural network algorithm presented for the study. The proposed approach successfully identifies the thickness of two different structures with high accuracy.

1. Introduction

Corrosion and wall thinning can reduce the mechanical strength of a steel structure as it can affect the metal thickness. Also, it is one of the most vital factors when dealing with life cycle costs of a structure. In this respect, nondestructive testing (NDT) plays an important role when creating an efficient health monitoring system for infrastructures. Although various NDT methods exist for damage detection, most of these methods require experts with expensive tools which can be quite heavy. To help overcome this problem, a portable monitoring system with a piezoelectric (PZT) material based device that can be attached and reattached for detecting wall thickness loss is investigated using one of the structural health monitoring techniques known as the electromechanical impedance (EMI) method. In general, a single PZT patch is attached directly to the surface of a target structure to perform the EMI method where the method was first introduced by Liang et al. [1]. In their study, the 1D model

in (1) shows the coupled relationship between the electrical admittance (inverse of impedance) of the PZT element $Y(\omega)$ to the mechanical impedance of the structure $Z_s(\omega)$, proving that any changes in $Z_s(\omega)$ will affect the electrical impedance of the attached PZT element.

$$Y(\omega) = i\omega a \left(\varepsilon_{33}^T (1 - i\delta) - \frac{Z_s(\omega)}{Z_s(\omega) + Z_a(\omega)} d_{3x}^2 \bar{Y}_{xx}^E \right). \quad (1)$$

Up to date, various authors have utilized the EMI method for damage detection [2–13]. Yu et al. [2] introduced chemical corrosion using hydrochloric acid onto a pipe structure where it was detected by performing the EMI method in the frequency range of 200 to 2000 kHz using the HP4194A impedance analyzer. The corrosion process was repeated 11 times until complete failure of the pipe surface where the changes in the real part of the impedance were evaluated using the damage index algorithm introduced in the study. Talakokula et al. [3] investigated detecting and quantifying the carbonation induced rebar corrosion level by bonding

a PZT patch onto the surface of the rebar where the reinforced concrete specimen was exposed to carbon dioxide for over 230 days. The CO_2 penetration depth was related to the equivalent stiffness parameter where the results were compared with scanning electron microscope images to show successful recognition of carbonation induced rebar corrosion in reinforced concrete. Simmers Jr. et al. [4] used an aluminum beam of 184 cm in size with 2.54 cm in width to introduce corrosion damage in 5 different places where the changes in the measured impedance signatures were quantified using the root mean square deviation (RMSD) equation. The results indicated that light corrosion can be identified up to 1.5 meters while tracking the progression of damage.

Virtually all the studies related to corrosion and damage detection using the EMI method involve permanently attaching the PZT material to a surface where the cost of the monitoring system would be high when dealing with large infrastructures. In addition, the wiring and PZT attachment on the surfaces can make the structure visually unattractive possibly raising another problem of managing the brittle PZT patch when exposed to the environment for a long time. Thus in this study, a PZT material based device that does not need to be permanently attached to a host structure is utilized [5], allowing one to easily attach and reattach to a steel structure without leaving any trail of monitoring. Due to the high sensitivity of the impedance signature, the impedance signature completely changes when reattached. This is solved by applying the probabilistic neural network (PNN) algorithm to the EMI method.

To induce the effect of wall thickness reduction for this study, multiple layers of thin metal plates of identical thickness were stacked for the experiment where removing each layer was considered as damage. With this approach, it becomes possible for one to reduce the thickness of a structure with the exact same thickness each time. Although it would be ideal to use a corrosive solution for reducing the test specimen, the EMI method is highly sensitive to small changes in the host structure and avoiding the effect of the impedance signatures changing due to the miniscule differences in the plate thickness compared to one another was considered important for this study. Thus the work presented in this study focused on the possibility of using the reattachable EMI method with the PNN technique against wall thickness reduction where this research will be continued further in a future study subjected to real corrosive environment.

2. Electromechanical Impedance Method Setup

For conducting the EMI method, a laptop is connected to the AD5933 evaluation board and then to the test specimen as shown in Figure 1. The evaluation board has been approved by the manufacturer (Analog Devices Inc.) of its ability to measure the real and imaginary part of the impedance up to 100 kHz with a maximum number of 511 data points. The positive and negative sides of PZT materials are connected to the board for measuring the impedance. The equipment is fully powered by a USB cable where data is also transmitted

TABLE 1: Properties of the PZT used for the study.

| Parameter | Symbol | Value |
|-----------------------------------|----------|------------------------------|
| Relative dielectric constant | K_3^T | 1800 |
| Piezoelectric strain coefficient | d_{33} | 390×10^{-12} m/V |
| | d_{31} | -190×10^{-12} m/V |
| Piezoelectric voltage coefficient | g_{33} | 24.0×10^{-3} V m/N |
| | g_{31} | -11.6×10^{-3} V m/N |
| Coupling coefficient | k_{33} | 0.72 |
| | k_{31} | 0.35 |

though this line. The PZT model of PSI-5A4E with the thickness of 0.508 mm was purchased (Piezo Systems Inc.) and used throughout the study where some of its properties can be seen in Table 1. Upon measuring the impedance signature, root mean square deviation (RMSD) technique is applied to analyze the data for quantifying the intensity of damage. The RMSD equation (2) shown below uses two impedance signatures in general where before $(Z_k)_i$ and after $(Z_k)_j$ damage signatures are inserted into the equation for the analysis. For this study, the real part of the impedance was used as it has been known to perform better and to be less prone to signature changes subjected to temperature variations compared to the imaginary part of the impedance [14].

$$\text{RMSD} = \left(\frac{\sum_{k=1}^N [\text{Re}(Z_k)_j - \text{Re}(Z_k)_i]^2}{\sum_{k=1}^N [\text{Re}(Z_k)_i]^2} \right)^{1/2}. \quad (2)$$

3. Repeatability Performance of the Reattachable PZT Devices

A conventional method of conducting the EMI method is to permanently attach a small piece of a PZT transducer to a surface of the target structure using a commercial adhesive. One of the issues with permanent installation is that, with large infrastructures, the cost of attaching the required number of PZT transducers for covering the target structure would be extremely high. In addition, managing such system would also be costly, as some places would be difficult for one to access (tall buildings, top of a bridge, etc.). Thus in this study, the idea of a reattachable PZT device introduced by Na et al. [5] was used which allows one to attach and reattach the PZT device to a steel structure without any adhesive. Figure 2 shows the reattachable device for this study where a magnet disc of 25 mm diameter and 5 mm thickness is used with the 15 mm square PZT transducer attached to top of its surface using a commercial adhesive (Loctite quickset epoxy). Then after 48 hours of adhesive curing, the same adhesive was used to cover the top of the PZT for protection purposes as the high frequency usage of the EMI method makes it very sensitive to signature variations. So to observe how sensitive the impedance signatures are, a simple test involving the PZT device with a square metal plate of a size 100 mm with 0.3 mm thickness was used. Here, the impedance signature

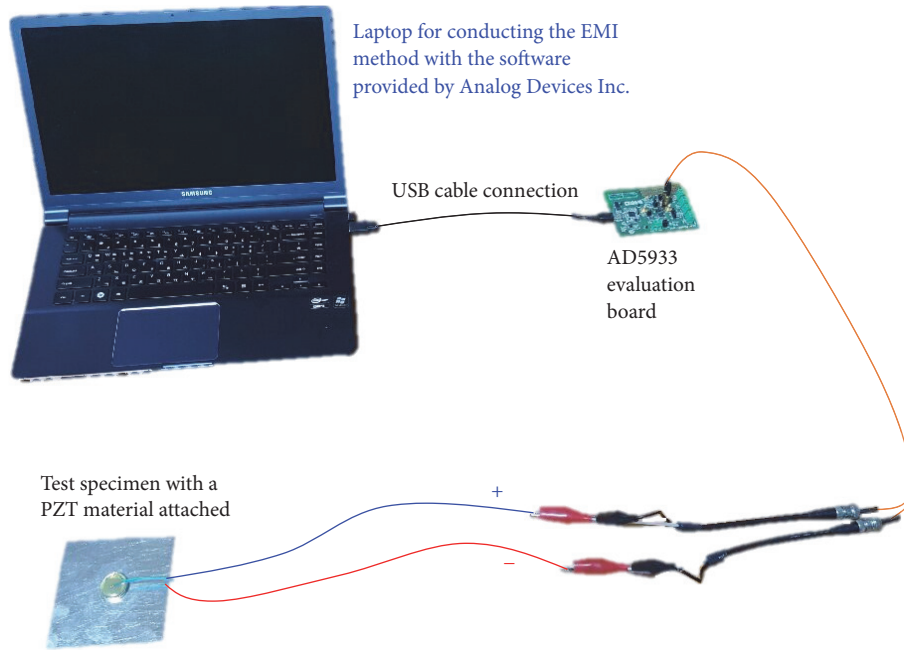


FIGURE 1: Photo of the AD5933 evaluation board.

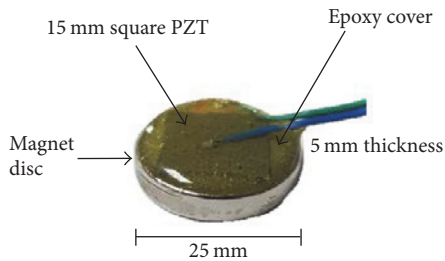


FIGURE 2: Reattachable PZT device.

was measured after attaching the PZT device to the plate, and then another measurement was made after detaching the PZT device. Since the PZT device was made out of a magnet, the magnetic force alone was strong enough to be attached to the metal plate without any adhesive. This process (shown in Figure 3) was repeated until 10 impedance signatures were acquired where the PZT device was attached to the center of the plate each time, visually checking its placement to simulate a real testing environment. The results of this test are plotted in Figure 4 showing how sensitive it is subjected to the reattachments. The signatures shift in either the left or right direction with the shape of the peak changing randomly. Under this circumstance, it is difficult for one to analyze if a host structure is damaged as the impedance signatures change although the actual host structure is undamaged. Thus one needs to distinguish the impedance signature changes of a damaged structure from the signature changes caused by reattaching the PZT device. To achieve this, a probabilistic neural network (PNN) algorithm was used.

4. Application of the PNN Algorithm

To overcome the problem of repeatability as shown in the previous section, PNN introduced by Specht [15] is used in conjunction with the RMSD equation. The training process is known to be relatively faster compared to other artificial neural network techniques and is guaranteed to converge to an optimal classifier with the increase in the size of the representative training set. One can also add or remove training samples without any extensive retraining making the PNN algorithm suitable as the integrity of a host structure can be damaged (changed) due its surrounding environment with time.

Figure 5 shows the classification algorithm with 5 categories in the pattern layer with each category representing the thickness of the host structure (5 metal plate layers = 5 categories) with 10 trained data. Each node in this layer contains the Gaussian function (see (3)) where the data from the input layer (500 point impedance signature data) is calculated into a single number to be processed onto the summation layer. The categories (pattern layer) with the least difference compared to the input impedance signature will result in a low value where a large difference between the input and categories (pattern layer) will result in a higher value. The output layer then identifies the structure thickness by choosing the node with the lowest value.

$$P = f(x_k) = e^{(\sum_{k=1}^N (x_k - (x_k)_T)^2 / (\sigma^2 \cdot \sum_{k=1}^N (x_k)_T^2))}. \quad (3)$$

For the Gaussian function in (3), x_k and $(x_k)_T$ represent the input data and the trained data, respectively. σ of 0.5 is used for this study which is the constant controlling the width of the function requiring an educated guess based on the data.



FIGURE 3: Attachment and reattachment of the PZT device.

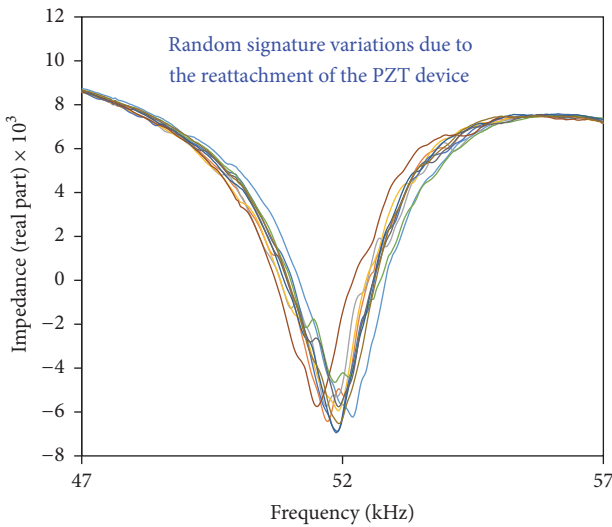


FIGURE 4: Impedance signatures from the reattachment test.

Once the training is complete, the PNN algorithm is ready for predicting the thickness of the host structure. Thus with a single measurement, it will predict the thickness of the target structure.

5. Data Training and Experimental Setup

5.1. Training the PNN Algorithm. The pattern layer of the PNN algorithm must be trained for it to correctly identify the thickness of a target structure. To achieve this, 10 impedance signatures are measured to be used as training data for each of the 5 categories. For the signature measurements, the PZT device is attached to the middle of a stack with 5 square metal plates (100 mm length with either 0.15 mm or 0.3 mm thickness) where then the signature is measured. Afterwards, the PZT device is completely detached and attached again in the middle of the stack. This process is identical to the process shown in Figure 3 with the impedance signatures being measured until 10 signatures are acquired to be inserted into the first category as the training data (from nodes $P_{(5,1)}$ to $P_{(5,10)}$). The next set of training data is measured after removing a metal plate and then measuring the impedance signatures by attaching and detaching the PZT device until

10 signatures are obtained again (from nodes $P_{(4,1)}$ to $P_{(4,10)}$). Training is complete once the impedance signatures are measured with the last metal plate, totaling 50 impedance signatures to be used as the training data for nodes $P_{(5,1)}$ to $P_{(1,10)}$.

For attaching the PZT device to the middle of the metal plate, this was achieved manually to simulate a real field environment as it is virtually impossible to reattach the device to the exact same spot. Thus the presented study brings one step close for the EMI method to be used for practical applications. Figure 6 shows the impedance signatures measured for the training data used for the next section (Section 5.2) using a metal plate of 0.15 mm thickness. Figures 6(a)–6(e) shows 10 signature measurements from a single layer to 5 layers of metal plates and Figure 6(f) shows all the signatures combined to illustrate the overall trend of the impedance signatures. By observation, Figure 6(a) shows impedance signature variations mainly in the resonance frequency range between 52 kHz and 55 kHz where the downward peak goes in the up or down direction and shifting in the left or right direction. Similar observations are made for the rest of the figures from Figures 6(b)–6(e) where the impedance signature changes are focused in the resonance frequency region. Another observation made here is that the impedance signatures from Figure 6(e) seem to change more severely compared to Figure 6(a) with the existence of multiple small peaks. In addition, the downward peak for Figure 6(e) has decreased further down compared to Figure 6(a) to around 8000 ohms. Such reason can be due to the loss in metal thickness causing the weight to be lost where the structure becomes more prone to a higher level amplitude excitation. In Figure 6(f), combining all 50 impedance signatures shows a clear trend where the loss in the thickness causes the signature to shift in the left direction with the peaks decreasing towards the downward direction in general. Thus with these 50 pieces of training data inserted into the pattern layer of the PNN algorithm, it is now set to predict the thickness of the metal stack introduced in the following subsection.

5.2. Thickness Prediction Experiment Using 0.15 mm Thick Metal Plates. To predict the thickness of a metal stack subjected to thickness loss, 5 square metal plates with 100 mm length and 0.15 mm thickness are used. With this approach, one can reduce the thickness of the target structure with

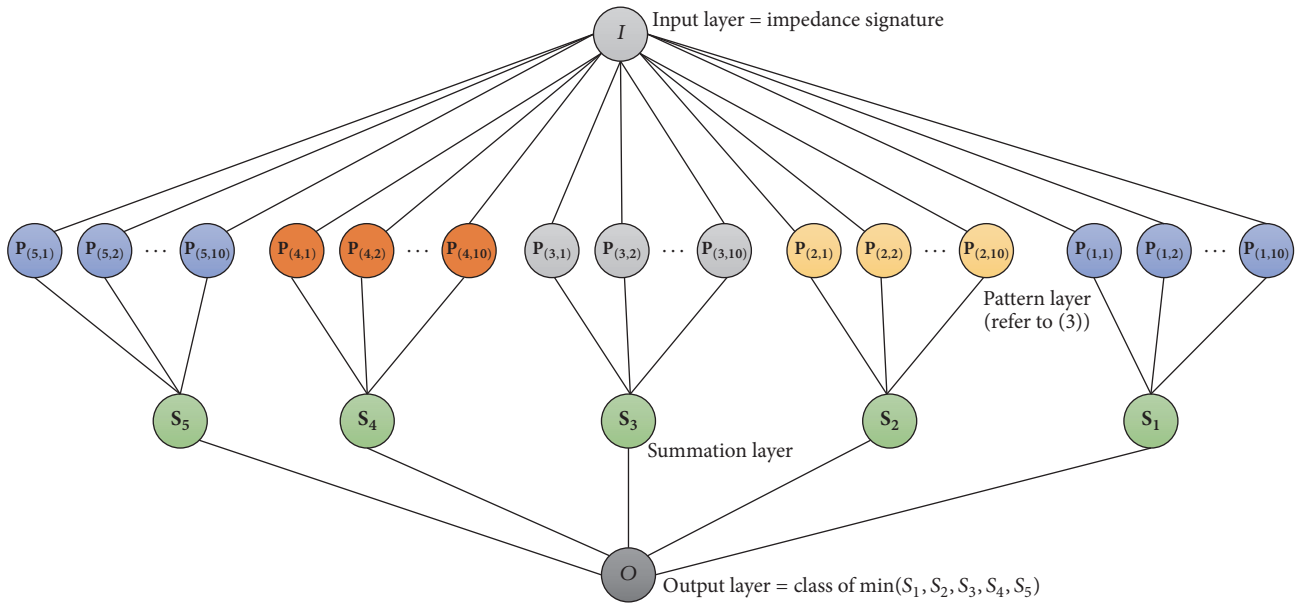


FIGURE 5: PNN algorithm created for the study.

an exact same thickness each time. Thus the 5 metal plates are stacked on top of one another and removing a single layer (0.15 mm) is defined as thickness loss damage. The PZT device is attached to the middle of the plate where the plates are held together by the magnetic force of the PZT device (Figure 7(a)). First, the impedance signature is measured with all 5 metal plates stacked together with the PZT device attached on top of the stack. This will be referred to as case “0.15T_5” where the acquired signature is inserted into the PNN algorithm for the thickness prediction of the metal stack. The next case, “0.15T_4” is achieved by removing a single plate from “0.15T_5” and then detaching and reattaching the PZT device, measuring impedance afterwards. Again, the acquired impedance signature is inserted into the PNN algorithm for a thickness prediction. The next case “0.15T_3” is conducted by removing another plate and measuring the impedance where this process is continued until the impedance signature is measured for the last metal plate (cases “0.15T_2” and “0.15T_1”). Conducting these 5 test cases (0.15T_5 to 0.15T_1) will be referred to as “Test_#x” where x represents the n th number of Test_#. The reason for defining Test_# is to check the reliability performance of the algorithm used in this study by repeating the experiment which is discussed in the later section. Figure 7(b) shows 5 signatures measured for 0.15T_5 case where the variations in the signatures can be easily observed. Although reattaching the PZT device significantly changes the impedance signature, the PNN algorithm is assumed to correctly identify the thickness of the structure. Thus once the algorithm is equipped with enough training data, it becomes possible for one to use the reattachable PZT device to identify the thickness without any trail of sensor installation under the condition that magnets can be attached to the host structure.

5.3. Thickness Prediction Experiment Using 0.3 mm Thick Metal Plates. In this part of the experiment, 5 square metal plates of 100 mm in length and 0.3 mm thickness are used to conduct an experiment identical to the previous section. Again, the impedance signature is measured with all 5 metal plates stacked together as shown in Figure 8(a), referred to as case 0.3T_5 where the impedance signature is inserted into the input layer of the PNN algorithm for a thickness prediction. Then, impedance signature is measured after removing a metal plate until the last plate is remaining (cases 0.3T_4 to 0.3T_1). For evaluating the repeatability performance of the proposed approach, 5 consecutive measurements are conducted by detaching and reattaching the PZT device for each of the 5 cases, totaling 25 impedance signatures. The 5 signature measurements for 0.3T_5 case can be seen in Figure 8(b) where the variations can be observed with peaks shifting in all 4 directions. After the completion of the proposed tests, the impedance signatures from Sections 5.2 and 5.3 are briefly compared to seek for differences in its trend with the use of the metal plates with different thicknesses.

6. Results and Discussions

6.1. Thickness Prediction of the 0.15 mm Metal Layer Stack. Table 2 shows the results of the PNN algorithm from the 0.15T_5 case in Section 5.2 where the 5 impedance signatures measured for this case were inserted into the algorithm. Each row in the table represents the number of metal layers (labeled “ x ”) in the stack and the columns represent the calculated values for the pattern layer. The last column represents the summation layer obtained from summing all the values in each row. The italic number (output layer) in this column is the minimum value from the column as the PNN algorithm

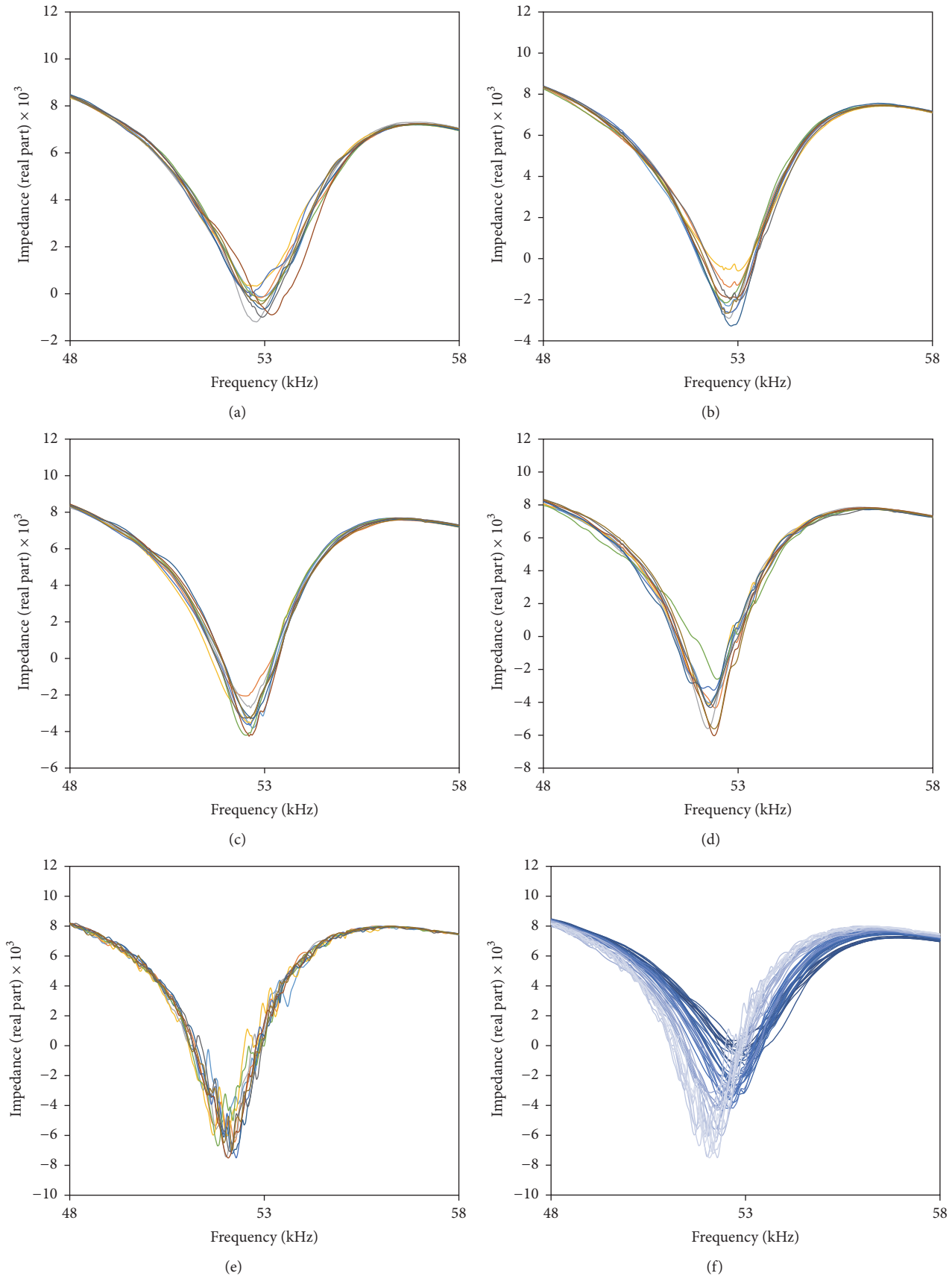
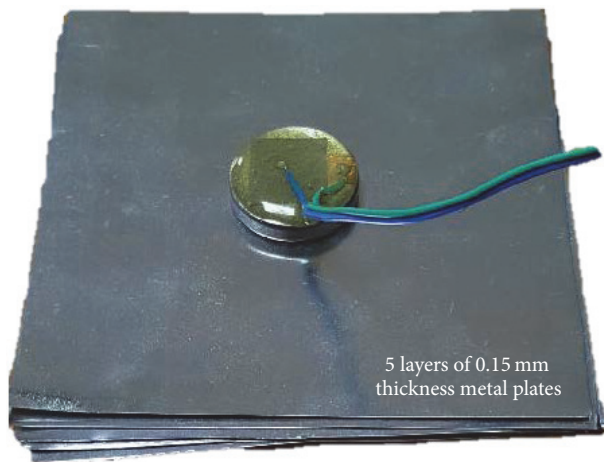
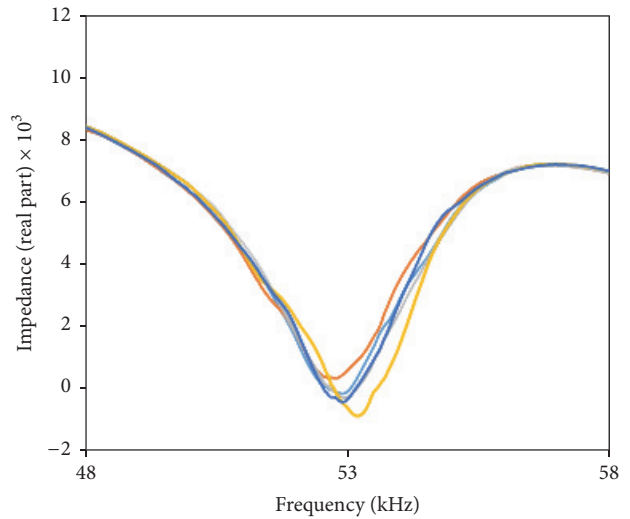


FIGURE 6: Impedance signatures of training data for (a) 5 metal plates, (b) 4 metal plates, (c) 3 metal plates, (d) 2 metal plates, (e) 1 metal plate, and (f) all results combined.

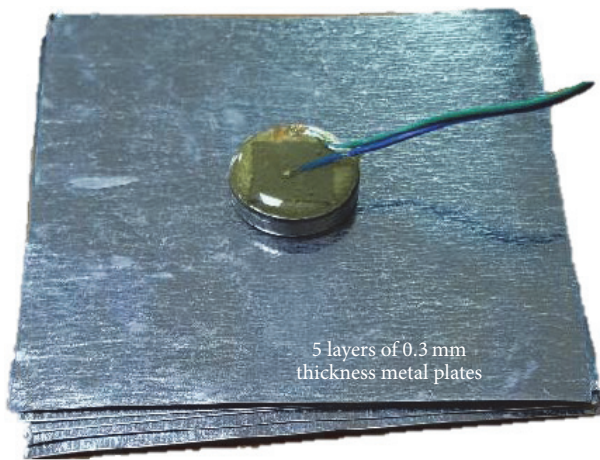


(a) 0.15-A case setup using the reattachable PZT device

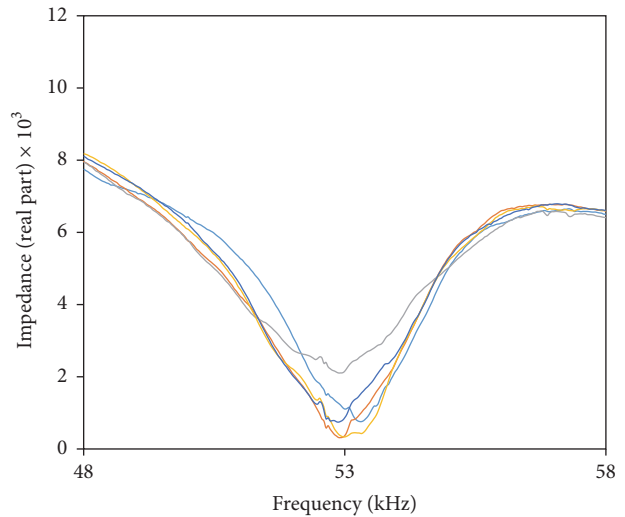


(b) 5 consecutive measurements for 0.15-A case

FIGURE 7



(a) 0.3-A case setup using the reattachable PZT device



(b) 5 consecutive measurements for 0.3-A case

FIGURE 8

selects the minimum value and predicts that row as the “x” number of metal layer(s) remaining from the stack. Thus with the first test, the italic number is 12.7, indicating that the stack has 5 metal layers, correctly identifying the status of the tested stack. Observing at the rest of the tests for 0.15T_5 case, the results (italic numbers) are 11.5, 11.4, 12.1, and 11.4 where a wrong prediction is made with the 12.1 value indicating that 4 metal layers are left in the stack. Out of the 5 tests from 0.15T_5 case, 4 predictions were correct showing 80% accuracy for this part of the test.

To identify the predictions made by the PNN algorithm for all the tests (Test_#x for 0.15T_x cases), a bar graph is plotted in Figure 9. y-axis is the values obtained of the summation layer nodes of the PNN algorithm and x-axis is the test cases from 0.15T_5 to 0.15T_1. The numbers in the

circle (⑤, ④, ③, ②, ①) are the predicted number of plates remaining from the metal stack (the output layer value of the PNN algorithm). This is defined by selecting the lowest summation value from each case. Since Test_#1 to Test_#5 are conducted by detaching one plate at a time, it would be ideal for the PNN algorithm to predict the number of metal plates in the order of 5, 4, 3, 2, and 1 for each Test_#x. This result can be seen for Test_#1, Test_#2, and Test_#3 where Test_#4 and Test_#5 have one wrong prediction each (0.15T_5 and 0.15T_2). Thus with the 25 output layer values from the 5 cases, 2 predictions were incorrect, resulting in 92% (23/25) accuracy of the PNN algorithm.

6.2. Thickness Prediction of the 0.3 mm Metal Layer Stack. Figure 10 shows the bar plot for Test_#x for 0.3T_x case

TABLE 2: PNN algorithm results of case 0.15_A.

| | $P(x, 1)$ | $P(x, 2)$ | $P(x, 3)$ | $P(x, 4)$ | $P(x, 5)$ | $P(x, 6)$ | $P(x, 7)$ | $P(x, 8)$ | $P(x, 9)$ | $P(x, 10)$ | S_x |
|--------------------|-----------|-----------|-----------|-----------|-----------|-----------|-----------|-----------|-----------|------------|-------|
| First measurement | | | | | | | | | | | |
| $x = 5$ | 1.2 | 1.3 | 1.3 | 1.4 | 1.4 | 1.2 | 1.2 | 1.2 | 1.2 | 1.3 | 12.7 |
| $x = 4$ | 1.5 | 1.4 | 1.5 | 1.3 | 1.5 | 1.5 | 1.6 | 1.4 | 1.3 | 1.5 | 14.5 |
| $x = 3$ | 1.8 | 1.8 | 1.8 | 2.1 | 2.0 | 2.1 | 1.7 | 1.8 | 1.9 | 1.7 | 18.7 |
| $x = 2$ | 2.6 | 2.6 | 3.0 | 2.8 | 2.6 | 2.1 | 2.9 | 2.9 | 2.5 | 2.6 | 26.6 |
| $x = 1$ | 3.3 | 3.7 | 4.0 | 3.8 | 3.8 | 3.6 | 3.7 | 3.9 | 3.5 | 3.7 | 37.0 |
| Second measurement | | | | | | | | | | | |
| $x = 5$ | 1.1 | 1.2 | 1.1 | 1.3 | 1.2 | 1.1 | 1.1 | 1.2 | 1.1 | 1.1 | 11.5 |
| $x = 4$ | 1.4 | 1.2 | 1.4 | 1.2 | 1.4 | 1.4 | 1.5 | 1.3 | 1.2 | 1.4 | 13.4 |
| $x = 3$ | 1.7 | 1.6 | 1.6 | 1.9 | 1.8 | 1.9 | 1.6 | 1.7 | 1.7 | 1.6 | 17.1 |
| $x = 2$ | 2.4 | 2.4 | 2.8 | 2.5 | 2.4 | 1.9 | 2.6 | 2.6 | 2.3 | 2.4 | 24.3 |
| $x = 1$ | 3.1 | 3.4 | 3.7 | 3.6 | 3.5 | 3.3 | 3.4 | 3.6 | 3.2 | 3.4 | 34.2 |
| Third measurement | | | | | | | | | | | |
| $x = 5$ | 1.1 | 1.1 | 1.2 | 1.2 | 1.2 | 1.1 | 1.1 | 1.2 | 1.1 | 1.1 | 11.4 |
| $x = 4$ | 1.5 | 1.3 | 1.5 | 1.2 | 1.5 | 1.5 | 1.6 | 1.5 | 1.4 | 1.5 | 14.5 |
| $x = 3$ | 1.8 | 1.7 | 1.7 | 2.0 | 1.9 | 2.0 | 1.7 | 1.9 | 1.9 | 1.7 | 18.3 |
| $x = 2$ | 2.4 | 2.5 | 2.8 | 2.5 | 2.4 | 1.9 | 2.7 | 2.7 | 2.4 | 2.5 | 24.8 |
| $x = 1$ | 3.1 | 3.5 | 3.7 | 3.6 | 3.5 | 3.4 | 3.5 | 3.6 | 3.3 | 3.4 | 34.6 |
| Fourth measurement | | | | | | | | | | | |
| $x = 5$ | 1.3 | 1.3 | 1.2 | 1.4 | 1.3 | 1.3 | 1.2 | 1.4 | 1.2 | 1.3 | 12.9 |
| $x = 4$ | 1.2 | 1.2 | 1.2 | 1.2 | 1.2 | 1.2 | 1.3 | 1.2 | 1.2 | 1.2 | 12.1 |
| $x = 3$ | 1.5 | 1.4 | 1.4 | 1.7 | 1.6 | 1.6 | 1.4 | 1.5 | 1.5 | 1.4 | 15.0 |
| $x = 2$ | 2.1 | 2.1 | 2.4 | 2.2 | 2.1 | 1.7 | 2.3 | 2.3 | 2.0 | 2.1 | 21.3 |
| $x = 1$ | 2.7 | 3.0 | 3.2 | 3.2 | 3.0 | 2.9 | 2.9 | 3.1 | 2.8 | 2.9 | 29.7 |
| Fifth measurement | | | | | | | | | | | |
| $x = 5$ | 1.1 | 1.1 | 1.2 | 1.1 | 1.1 | 1.1 | 1.1 | 1.3 | 1.2 | 1.1 | 11.4 |
| $x = 4$ | 1.6 | 1.3 | 1.6 | 1.3 | 1.6 | 1.5 | 1.7 | 1.5 | 1.4 | 1.5 | 15.0 |
| $x = 3$ | 1.9 | 1.7 | 1.7 | 2.1 | 2.0 | 2.0 | 1.8 | 1.9 | 1.9 | 1.8 | 18.8 |
| $x = 2$ | 2.4 | 2.5 | 2.8 | 2.5 | 2.4 | 1.9 | 2.6 | 2.7 | 2.3 | 2.5 | 24.6 |
| $x = 1$ | 3.0 | 3.4 | 3.7 | 3.5 | 3.5 | 3.3 | 3.5 | 3.6 | 3.3 | 3.4 | 34.2 |

experiments where the numbers in the circle represent the number of metal layers left in the stack (output layer values). Again, it would be ideal to predict the number of plates decreasing from 5 to 1 for each Test_# x . Here, only Test_#4 and Test_#5 have correctly predicted all the results with one wrong prediction resulting from Test_#1 to Test_#3. Thus with the 25 output layer values from the 5 cases, 3 predictions were incorrect, resulting in 88% (22/25) accuracy of the PNN algorithm.

To investigate the impedance signatures for the metal stack used in the previous section with the stack used in this section, Figure 11 is plotted using the 50 training data used for the PNN algorithm. In the figure, each of the impedance signatures is created by averaging 10 of the training data at each category. By observation, the amplitude of the peak in Figure 11(a) decreases within the range of 1000~2000 ohms each time the metal plate is removed with the signatures shifting in the left direction. Left shifting movement is also observed for Figure 11(b) where the peak decreases with much smaller amplitude for the top 4 impedance signatures. The last impedance signature representing a stack with one metal

layer shows a large decrease in the amplitude. Comparing the two figures, a clear difference in the impedance signatures can be observed for the middle 3 signatures (stacks with 4, 3, and 2 metal layers) where the amplitudes are much smaller for Figure 11(b). One possible reason is due to the thicker metal layers (0.3 mm versus 0.15 mm) which affects the attachment strength as weaker magnetic force is experienced with increase in the distance. Since this study focusses on the possibility of reattaching the PZT device with the application of a neural network technique, a detailed investigation on the effect of magnetic attachment strength on impedance signatures will be dealt in a possible future work. An important fact here is that, regardless of the magnetic strength effect and the difference in the metal thickness, the proposed approach can successfully identify the thickness of the metal stack with high accuracy.

6.3. Improving the Accuracy of the PNN Algorithm. From the results of Sections 6.1 and 6.2, the accuracy of the PNN algorithm subjected to 5 cases tested were 92% and 88%, respectively. Since each case involved measuring the

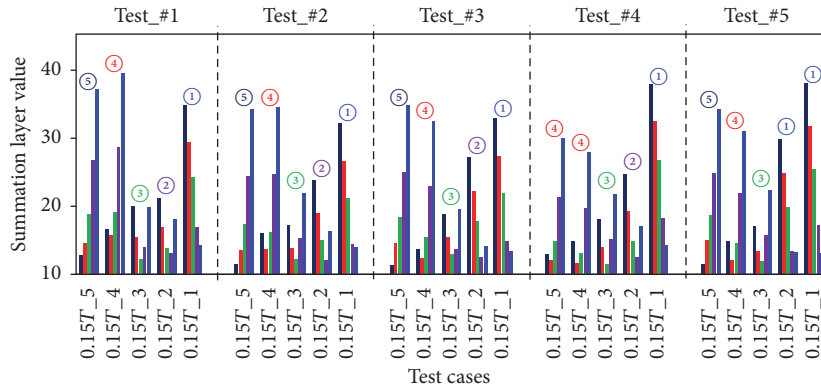


FIGURE 9: Summation and output layer results for Section 6.1.

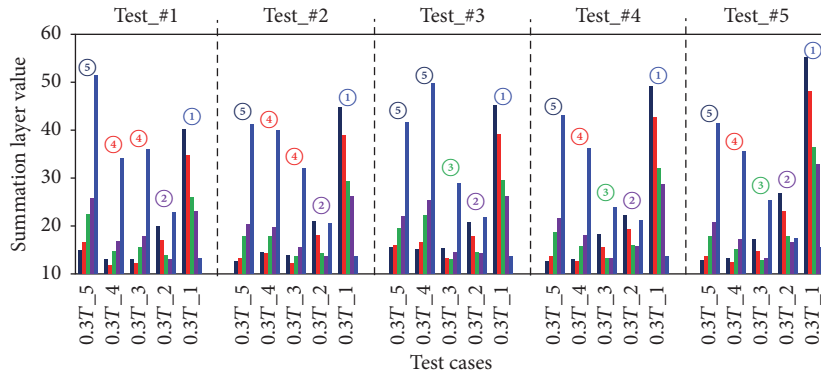


FIGURE 10: Summation and output layer results for Section 6.2.

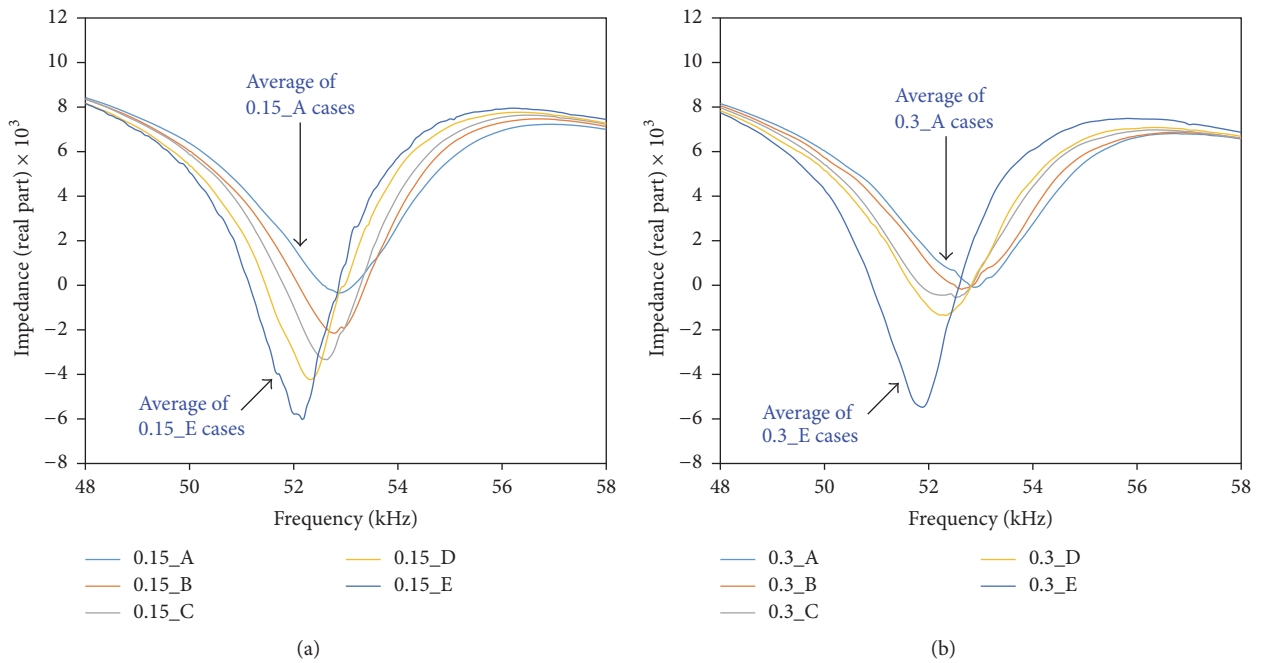


FIGURE 11: Averaged training data for (a) 0.15 mm thickness cases and (b) 0.3 mm thickness cases.

impedance signature of the target structure 5 times, the method of improving the accuracy of the PNN algorithm can be easily achieved by selecting the output layer value that appears the most out of these 5 measurements. For an example, the 0.15T_5 case resulted in 5 predictions where 4 of the predictions correctly identified the number of the metal layers in the stack (5 layers). Thus, out of the 5 measurements, choosing the most frequently appeared result (5 layers for this case) will result in improving the prediction accuracy of the PNN algorithm. By applying this approach, this results in 100% accurate prediction for all the cases (0.15T_5, 0.15T_4, 0.15T_3, 0.15T_2, 0.15T_1, 0.3T_5, 0.3T_4, 0.3T_3, 0.3T_2, and 0.3T_1) conducted in this study.

7. Conclusions

In this study, a reattachable EMI method was used to identify the reduction in the metal layer thickness. Since the impedance signatures are highly sensitive subjected to any change in the property of a host structure, detaching and then reattaching the PZT transducer can significantly change the impedance signature. This can cause difficulty when identifying damage as the EMI method heavily relies on signature variations. Thus to overcome this problem, a neural network technique, PNN algorithm, was used to identify a stack of metal plates against reduction in thickness. The test was to evaluate the performance of the reattachable EMI method in conjunction with the PNN algorithm introduced in this study using two metal plate stacks with different thicknesses.

The first part of the test involved stacking 5 metal layers with 0.15 mm thickness where the reattachable PZT was attached in the middle of the stack for the experiment. Before the actual experiment, the PNN algorithm was trained, where the PZT device was attached and reattached 10 times while acquiring the impedance signatures. After the 10th measurement, a single layer from the metal stack was removed and another 10 impedance measurements were acquired until only one metal plate was left in the stack. 50 pieces of trained data were inserted into the pattern layer of the PNN algorithm to begin the experiment. Afterwards, Test_#1 to Test_#5 were conducted for the 5 cases (0.15T_5, 0.15T_4, 0.15T_3, 0.15T_2, and 0.15T_1) where 25 output layer node values were obtained. Out of the 25 predictions, the PNN algorithm correctly predicted 23 outcomes, resulting in 92% accuracy of the test.

The second part of the test involved using 5 metal layers with an increased thickness of 0.3 mm. Again, 50 pieces of training data were obtained and Test_#1 to Test_#5 were conducted for the 5 cases (0.3T_5, 0.3T_4, 0.3T_3, 0.3T_2, and 0.3T_1) where 25 output layer node values were obtained. Out of the 25 predictions, the PNN algorithm correctly predicted 22 outcomes, resulting in 88% accuracy of the test. Afterwards, 10 pieces of trained data measured at different metal layers were averaged for all cases to investigate any existence of trend between the two different thickness metal stacks where a clear difference in the signatures were observed. Although the amplitude of the impedance signatures decreased with each removal of the

metal plate, the thicker stack (0.3 mm layers) experienced smaller decrease in the peak amplitude compared to the thinner stack (0.15 mm layers). Nevertheless, the introduced PNN algorithm successfully identified the thickness of the metal stack with high accuracy. For increasing the accuracy of the PNN algorithm introduced in this study, an approach was stated by selecting the outcome that appeared the most out of the 5 measurements for each of the cases. Since 5 impedance signatures were measured for each of the cases, selecting the most frequent results from the PNN algorithm resulted in 100% accuracy for both of the metal stacks.

8. Future Work

Bridges and buildings are usually inspected using NDT methods where the increase in complexity and height of the structure cause difficulty during inspection. Such work can be time-consuming and to overcome this problem, this work is to contribute towards a possibility of conducting an inspection using drones. One of the major disadvantages of a local method such as the EMI method is the small sensing range, and this could be solved by using a drone which can easily fly onto virtually any surfaces of a structure. A possible next step in this research would be to install an impedance measuring device onto a drone and conduct the reattachable EMI method against real damage scenarios. In addition, with the ability of the drones to be able to fly, a solar energy harvesting device will also be considered to create a drone that can self-recharge to create a system that requires zero energy input.

Conflicts of Interest

The authors declare that there are no conflicts of interest regarding the publication of this paper.

Acknowledgments

The research was supported by a grant from “Development of Infrastructure Technology for Hyper Speed Transportation System (20170095-001)” funded by Korea Institute of Civil Engineering and Building Technology (KICT), South Korea.

References

- [1] C. Liang, F. P. Sun, and C. A. Rogers, “Coupled electro-mechanical analysis of adaptive material systems—determination of the actuator power consumption and system energy transfer,” *Journal of Intelligent Material Systems and Structures*, vol. 5, no. 1, pp. 12–20, 1997.
- [2] L. Yu, V. Giurgiutiu, and P. Pollock, “A multi-mode sensing system for corrosion detection using piezoelectric wafer active sensors,” in *Proceedings of the The 15th International Symposium on: Smart Structures and Materials & Nondestructive Evaluation and Health Monitoring*, p. 69322H, 2008.
- [3] V. Talakokula, S. Bhalla, R. J. Ball et al., “Diagnosis of carbonation induced corrosion initiation and progression in reinforced concrete structures using piezo-impedance transducers,” *Sensors and Actuators, A: Physical*, vol. 242, pp. 79–91, 2016.

- [4] G. E. Simmers Jr., H. A. Sodano, G. Park, and D. J. Inman, "Detection of corrosion using piezoelectric impedance-based structural health monitoring," *ALAA Journal*, vol. 44, no. 11, pp. 2800–2803, 2006.
- [5] S. Na, R. Tawie, and H.-K. Lee, "Electromechanical impedance method of fiber-reinforced plastic adhesive joints in corrosive environment using a reusable piezoelectric device," *Journal of Intelligent Material Systems and Structures*, vol. 23, no. 7, pp. 737–747, 2012.
- [6] W. S. Na, "Progressive damage detection using the reusable electromechanical impedance method for metal structures with a possibility of weight loss identification," *Smart Materials and Structures*, vol. 25, no. 5, Article ID 055039, 2016.
- [7] G. Park, H. H. Cudney, and D. J. Inman, "Impedance-based health monitoring of civil structural components," *Journal of Infrastructure Systems*, vol. 6, no. 4, pp. 153–160, 2000.
- [8] Y. Yang and Y. Hu, "Electromechanical impedance modeling of PZT transducers for health monitoring of cylindrical shell structures," *Smart Materials and Structures*, vol. 17, no. 1, Article ID 015005, 2008.
- [9] R. Shanker, S. Bhalla, A. Gupta, and M. Praveen Kumar, "Dual use of PZT patches as sensors in global dynamic and local electromechanical impedance techniques for structural health monitoring," *Journal of Intelligent Material Systems and Structures*, vol. 22, no. 16, pp. 1841–1856, 2011.
- [10] S. Na and H. K. Lee, "Neural network approach for damaged area location prediction of a composite plate using electromechanical impedance technique," *Composites Science and Technology*, vol. 88, pp. 62–68, 2013.
- [11] G. Park, C. R. Farrar, F. L. Di Scalea, and S. Coccia, "Performance assessment and validation of piezoelectric active-sensors in structural health monitoring," *Smart Materials and Structures*, vol. 15, no. 6, pp. 1673–1683, 2006.
- [12] V. G. M. Annamdas and M. A. Radhika, "Electromechanical impedance of piezoelectric transducers for monitoring metallic and non-metallic structures: a review of wired, wireless and energy-harvesting methods," *Journal of Intelligent Material Systems and Structures*, vol. 24, no. 9, pp. 1021–1042, 2013.
- [13] S. Na and H. K. Lee, "A multi-sensing electromechanical impedance method for non-destructive evaluation of metallic structures," *Smart Materials and Structures*, vol. 22, no. 9, Article ID 095011, 2013.
- [14] F. P. Sun, Z. Chaudhry, C. Liang, and C. A. Rogers, "Truss structure integrity identification using PZT sensor-actuator," *Journal of Intelligent Material Systems and Structures*, vol. 6, no. 1, pp. 134–139, 1995.
- [15] D. F. Specht, "Probabilistic neural networks," *Neural Networks*, vol. 3, no. 1, pp. 109–118, 1990.

Research Article

The Research on Information Representation of Φ -OTDR Distributed Vibration Signals

Yanzhu Hu,¹ Song Wang,¹ Zhaoyang Wang,² and Yixin Zhang³

¹Automation College, Beijing University of Posts and Telecommunications, Beijing 100876, China

²Automation College, Beijing Institute of Technology, Beijing 100080, China

³Institute of Optical Communication Engineering, Nanjing University, Nanjing 210093, China

Correspondence should be addressed to Song Wang; wongsangwongsang@163.com

Received 25 June 2017; Revised 7 August 2017; Accepted 13 August 2017; Published 18 September 2017

Academic Editor: Taesun You

Copyright © 2017 Yanzhu Hu et al. This is an open access article distributed under the Creative Commons Attribution License, which permits unrestricted use, distribution, and reproduction in any medium, provided the original work is properly cited.

This paper mainly focuses on the representable problem of Φ -OTDR distributed vibration signals. The research included a signal extraction part and a signal representation part. Firstly, in order to extract the better Φ -OTDR signal, the time-domain data should be fully preserved. The 2D-TESP method is used to extract data in this paper. There are 29 characters in the traditional TESP method. The characters' number is reduced from 29 to 13 and the characters' dimension is expanded from 1 to 2 in the 2D-TESP method. Secondly, in order to represent Φ -OTDR signal better, the characteristics of Φ -OTDR data and damped vibration signals are combined in the paper. The EMD method and the NMF method are combined to form the new method in the paper. Some parameters in the proposed method are optimized and adjusted by GA method. After Φ -OTDR data is represented by the proposed method, there is excellent performance both on the length dimension and on the time dimension. Lastly, some experiments are carried out according to the physical truth in this paper. The experiments are carried out in the semianechoic room. The methods of the paper have better performance. The methods are proved to be effective through these experiments.

1. Introduce

Φ -OTDR (phase sensitive optical time-domain reflectometer) was put forward by Taylor and Lee in 1993. It serves as a typical technique for monitoring distributed vibrations. At present, it has a wide range of applications in the field of large building structure, health monitoring [1], perimeter security of important places [2], and so on. However, we hope to grasp its monitoring state more accurately, understand its vibration mode better, and enhance the monitoring efficiency. Therefore, it is of great significance for a standard time-domain analytic expression of the Φ -OTDR data. The Φ -OTDR data is a distributed vibration signal. In order to standardize the time-domain analytic expression, we need to extract and represent useful signals.

In signal extraction, the feature extraction methods in time domain mainly include probability analysis method, time series method, correlation function analysis method, and time-domain waveform feature analysis. Potočnik and Govekar analyzed probabilistic statistics of vibration signals.

They combined probability statistical analysis, feature extraction, and principal component analysis. The combined method is used for evaluating the performance of multiple classifiers [3]. Delpha et al. also combined probability statistical analysis, feature extraction, and principal component analysis. The combined method is used for condition monitoring and fault diagnosis [4]. Ma et al. used the time series model to extract features of vibration signals. The fault signals and nonfault signals are identified effectively by the method [5]. Liu et al. used multiplex detection to eliminate trend correlation analysis. The feature extraction is achieved finally [6]. Alhazza analyzed the waveform of the signal. Alhazza used waveforms to control the system [7]. In a word, the time series, correlation function, and waveform analysis are all based on the condition of obvious signals. But for the condition of poor SNR (signal-to-noise ratio), the probability analysis method has incomparable advantages to other methods because of its unique statistical characteristics. In signal expression, some scholars focused on the NMF (nonnegative matrix factorization) method and

its expansion methods. Gao et al. combined TDF method and NMF method. The combined method is used to diagnose faults [8]. Li et al. combined the S transformation method, NMF method, mutual information method, and multiobjective evolutionary algorithm [9]. Li et al. also, respectively, combined generalized S transform method to NMF method and 2DNMF method [10, 11]. Some other scholars focused on the EMD (empirical mode decomposition) method and its expansion methods. Rai and Upadhyay combined EMD method and K -means method to process the signal [12]. Liu et al. put EMD method into the process of multiplex detection to eliminate trend correlation analysis [6]. In conclusion, NMF and the related methods pay more attention to data model. These researches proceed from the fitting curve of signal separation but ignore the research of vibration mechanism. EMD and the related methods pay more attention to mechanism model. These researches simply proceed from the vibration mechanism and the expression curve but ignore the research of data features.

A summary of the above signal extraction studies is presented. When the SNR is weak, there will be some errors in the extraction of signals. Φ -OTDR technique monitors the vibration of an optical fiber. The shape of optical fiber is a line. There will be weak SNR on the farther point of the optical fiber with the attenuation of signal propagation. Therefore, a signal extraction method which is more suitable for the condition of weak SNR is needed. On the other hand, it is more necessary for data driven and mechanism driven organic combination for the representation of Φ -OTDR distributed vibration signals. The combined method can not only reflect the real situation of data but also reflect the real state of vibration. This paper is divided into two parts. The first part uses the 2D-TESP method to extract the signal. The 2D-TESP method has a more appropriate coding interval and also takes into account the first derivative and the two derivatives. It has good effect on signal extraction under weak SNR. The second part uses the GAEMD-NMF method to express the signal. It combines the EMD method and the NMF method. Some parameters are optimized by GA (genetic algorithm) after the two methods are combined. It can better solve the relative standard time-domain expression problem of distributed vibration signals.

2. Time-Domain Signal Extraction Based on 2D-TESP Algorithm

Signal extraction aims at better signal representation. Signal extraction requires full preservation of signal data prototypes in the time domain. Because of the characteristics of Φ -OTDR technology, it is hoped that effective signals can be extracted on the point with weak SNR. Therefore, the 2D-TESP method is selected to extract the features of the signal.

2.1. TESP Algorithm. TESP (time encoded signal processing) algorithm has two main features [13–16]. The first feature is that the algorithm is based on the time domain which directly processes the signal. The second feature is to convert signals into probabilistic models that contain finite elements. Simply

put, the method is to reencode the signal in the time domain. Typical time-frequency domain analysis algorithms include FFT, WT, and HHT. These algorithms have a long operation time and are also unsuitable for the poor SNR. They are not suited for distributed vibration data characteristics. TESP algorithm has the advantages of intuitive, small computation and simple implementation process. The traditional TESP algorithm is suitable for the feature extraction of speech signals [13]. The TESP method was improved by Wang's team in 2014. They apply the method to feature extraction of sound signals [14]. Wang et al. used it to develop two-dimensional feature extraction. They applied the improved algorithm to signal feature extraction in a complex environment [15, 16]. The specific implementation steps of TESP algorithm are as follows.

(1) The window is divided into time-domain signals on each length node of the optical fiber. In each window, the zero crossing rate of the signal is calculated. The interval between two adjacent zero points is a time period. According to the rule of TESP algorithm, each time period is called meta.

(2) There are two indexes in the meta. One is the duration; it is usually expressed in D . The other one is the signal form; it is usually expressed in S . At the same time, the following information is obtained according to these two indexes:

- (a) The number of sampling points existing in each element is the duration.
- (b) In each element's duration, the data is derived one by one. The extreme number in each element is obtained.
- (3) The matrix is constructed by using D and S as two dimensions. Each element is coded according to the elements in the matrix.

(4) The probability of each code in the matrix is compiled statistically. Finally, the probability distribution is used as a feature to be inserted into a classifier or cluster.

2.2. Feature Extraction Based on 2D-TESP Algorithm. There are only 29 characters because of the limitations of the encoding principle in traditional TESP algorithms. At the same time, the traditional TESP method achieves higher recognition rate in recognition. This paper focuses on the study of damped vibration. The encoding of 29 characters has far exceeded the requirements of damped vibration in the Φ -OTDR technique. Therefore, the D - S matrix is extended to D - S_1 and D - S_2 matrices in the paper at first. Secondly, the coding principle for each matrix is reduced from 29 to 13. Lastly, the D - S_1 and D - S_2 matrices are encoded together with joint probability distribution statistics to form the A matrix.

2.2.1. The Reduced TESP Symbol Table. In the traditional TESP algorithm, S only represents the first derivative. There may be mutual influence between points in Φ -OTDR technology. Therefore, further analysis of the Φ -OTDR signal is needed. The concept of the inflection point of the two-order derivative is introduced in the traditional method. In this paper, the S matrix that is the extreme point is set as D - S_1 , and the S matrix that is the inflection point is set as D - S_2 .

TABLE 1: The standard 29-symbol encoding table of D -S1 matrix.

| D | S | | | | | |
|-----|-----|-----|-----|-----|-----|-----|
| | 1 | 2 | 3 | 4 | 5 | >5 |
| 1 | 1 | | | | | |
| 2 | 2 | 2 | | | | |
| 3 | 3 | 3 | 3 | | | |
| 4 | 4 | 4 | 4 | 4 | | |
| 5 | 5 | 5 | 5 | 5 | 5 | |
| 6 | 6 | 6 | 6 | 6 | 6 | 6 |
| ... | ... | ... | ... | ... | ... | ... |
| 34 | 24 | 25 | 26 | 27 | 28 | 29 |
| 35 | 24 | 25 | 26 | 27 | 28 | 29 |

TABLE 2: The shrunk 13-symbol encoding table of D -S1 matrix.

| D | S | | | |
|-----|-----|-----|-----|-----|
| | 1 | 2 | 3 | >3 |
| 1 | 1 | | | |
| 2 | 1 | 1 | | |
| 3 | 1 | 2 | 2 | |
| 4 | 2 | 2 | 3 | |
| 5 | 3 | 3 | 3 | |
| 6 | 3 | 3 | 4 | 4 |
| ... | ... | ... | ... | ... |
| 34 | 11 | 12 | 13 | 13 |
| 35 | 11 | 12 | 13 | 13 |

TABLE 3: The standard 29-symbol encoding table of D -S2 matrix.

| D | S | | | | | |
|-----|-----|-----|-----|-----|-----|-----|
| | 1 | 2 | 3 | 4 | 5 | >5 |
| 3 | 1 | | | | | |
| 4 | 2 | 2 | | | | |
| 5 | 3 | 3 | 3 | | | |
| 6 | 4 | 4 | 4 | 4 | | |
| 7 | 5 | 5 | 5 | 5 | 5 | |
| 8 | 6 | 6 | 6 | 6 | 6 | 6 |
| ... | ... | ... | ... | ... | ... | ... |
| 34 | 24 | 25 | 26 | 27 | 28 | 29 |
| 35 | 24 | 25 | 26 | 27 | 28 | 29 |

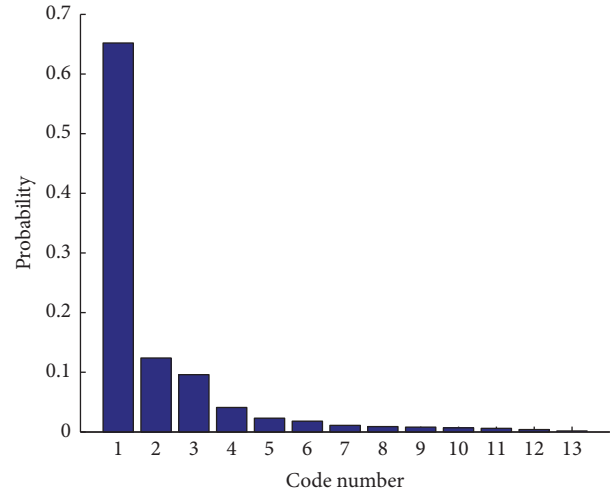
Because of the characteristics of the Φ -OTDR technology, the two indicators named D and S do not require such many codes. The new method employs 13 coded representations. Tables 1 and 2 represent the standard 29 encoded and the shrunk 13 encoded D -S1 matrices, respectively.

From Tables 1 and 2, the longest continuous sampling point is still 35. The statistics of first-order extreme points are reduced from six classes to four classes. And the encoding is reduced from 29 symbols to 13 symbols. Tables 3 and 4 are statistics of the two-order inflection point and the encoding result is reduced to 13 codes too.

By comparing Tables 2–5, it can be seen that the features represented are coarser with the codes' decrease. Actually, the

TABLE 4: The shrunk 13-symbol encoding table of D -S2 matrix.

| D | S | | | | |
|-----|-----|-----|-----|-----|-----|
| | 1 | 2 | 3 | >3 | |
| 3 | 1 | | | | |
| 4 | 1 | 1 | | | |
| 5 | 1 | 2 | 2 | | |
| 6 | 2 | 2 | 3 | | |
| 7 | 3 | 3 | 3 | | |
| 8 | 3 | 3 | 4 | 4 | |
| ... | ... | ... | ... | ... | ... |
| 34 | 11 | 12 | 13 | 13 | |
| 35 | 11 | 12 | 13 | 13 | |

FIGURE 1: The histogram of D -S1 coding's probability distribution in a signal.

probability distribution of encoded high numbers is almost zero, so it is possible to reduce the encoding to 13 characters.

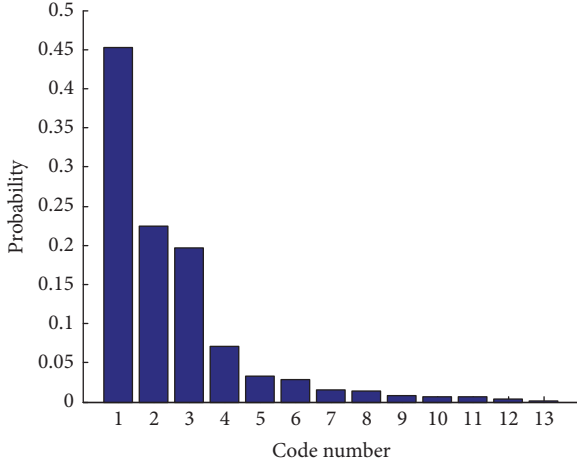
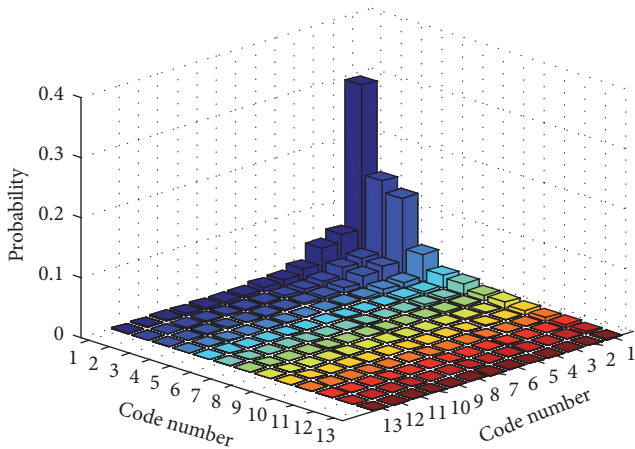
2.2.2. The Improved 2D-TESP Algorithm. After the original algorithm reduces to 13 characters, the feature of the algorithm is further represented as a two-dimensional A matrix. The two dimensions of the A matrix are the 13 codes in the shrunk D -S1 and in the shrunk D -S2 matrix. The values of the A matrices are the joint distribution probabilities of D -S1 and D -S2. We select a window of the signal to be encoded in accordance with the improved 2D-TESP algorithm. Figures 1 and 2 are histograms of probability distributions for D -S1 and D -S2. Figure 3 is a histogram of the A matrix with the joint distribution probability of D -S1 and D -S2. The A matrix is shown in Figure 3.

2.3. The Analysis of the Algorithm. In this paper, the improved 2D-TESP algorithm is mainly considered as follows.

(1) Because the damping vibration signal is encoded by TESP, the higher the coding number is, the more the probability drops. In this paper, the original 29-character encoding is reduced to 13-character encoding.

TABLE 5: Comparison of correct rates under different SNRs and different coding methods.

| Number | Name | Poor SNR | | | Good SNR | | |
|--------|------------------|-----------------|-------------------------|---------------------|-----------------|-------------------------|---------------------|
| | | <i>K</i> -means | Hierarchical clustering | Spectral clustering | <i>K</i> -means | Hierarchical clustering | Spectral clustering |
| (1) | <i>D</i> -S1(29) | 84.76% | 85.97% | 86.72% | 94.16% | 95.97% | 96.32% |
| (2) | <i>D</i> -S1(13) | 84.67% | 85.21% | 86.34% | 93.87% | 95.21% | 96.14% |
| (3) | <i>D</i> -S2(29) | 82.31% | 83.41% | 84.91% | 94.01% | 95.41% | 96.41% |
| (4) | <i>D</i> -S2(13) | 81.74% | 82.92% | 83.34% | 93.74% | 95.12% | 96.34% |
| (5) | <i>A</i> | 93.12% | 94.22% | 96.12% | 94.72% | 96.12% | 96.82% |

FIGURE 2: The histogram of *D*-S2 coding's probability distribution in a signal.FIGURE 3: The histogram of *A* coding's probability distribution in a signal.

(2) The Φ -OTDR technology has its own characteristics. Therefore, the signal is expressed not only by extreme points but also by inflection points.

(3) After the reduction of characters, the 13-character coding must be slightly rougher than the 29-character coding. Some experiments are carried out in *K*-means, hierarchical clustering, and spectral clustering. The effect of 13-character coding has not declined.

3. Time-Domain Signal Representation Based on GAEMD-NMF

Because of the presence of 3D data in the Φ -OTDR technique, the signal representations of “time dimensional” and “length dimensional” need to be required. In the representation of the time axis and length axis, it is necessary to consider the signal's physical model and actual data characteristics in a rational representation. Therefore, the paper combines two aspects of knowledge about the prior vibration model and the actual signal data decomposition. The new method is combined by EMD and NMF. The combined method is optimized by GA method. The parameters of the method are effectively corrected and finally good results are achieved.

3.1. *The EMD of Damped Vibration.* In the time amplitude plane, a damping vibration model is established because the data conforms to the law of damping vibration. The model is shown in

$$f_1(t) = A_1 e^{-t/\tau} \sin(\omega_1 t + \varphi_1) + B_1. \quad (1)$$

In the length amplitude plane, a SA model is established because the data conforms to the law of SA signal. The model is shown in

$$f_2(l) = A_2 \frac{\sin(\omega_2 l + \varphi_2)}{\omega_2 l + \varphi_2} + B_2. \quad (2)$$

After the superposition of signals, the model is shown in

$$F(t, l) = f_1(t) \cdot f_2(l). \quad (3)$$

According to the two models above, the original signal corresponds to the model to determine the various parameters. The concrete steps are as follows.

(1) The absolute maximum value of the signal amplitude on the time axis is A_1 . A_2 is identified as 1.

(2) The peak value points are fitted to a curve. The damping attenuation coefficient is obtained according to the fitted curve. The damping attenuation coefficient is recorded as τ .

(3) ω_1 is determined according to the number of zero crossings on the time axis.

(4) When the signal starts, it must start from zero. The parameter φ_1 is determined as 0 or 1.

(5) The parameters B_1 and B_2 are determined as 0 according to the actual data.

(6) The parameter w_2 is determined by the number of zero crossings on the length axis.

(7) When the signal starts, it must be the maximum. The parameter φ_2 is determined as 0.

3.2. *NMF*. NMF (nonnegative matrix factorization) was proposed by Lee and Seung in 1999. It is a new matrix decomposition method published in Nature magazine [17]. It is widely used in image analysis, data mining, speech processing, and other fields. In recent years, scholars have made some modifications on the basis of the original NMF algorithm and achieved many results [18, 19]. The advantages of NMF algorithm are two main points. Firstly, its decomposition form and results are very explanatory because it requires matrix elements to be nonnegative. Secondly, the result of matrix decomposition usually has natural sparsity. Its results not only are easy to express, but also reduce the space occupation. Since the value of the vibration signal is positive, the vibration data are processed by using nonnegative matrix factorization to meet the requirements of the algorithm.

The nonnegative matrix factorization algorithm is defined as follows. A nonnegative matrix X_+ is set. It is decomposed into the product of two nonnegative matrices named W_{+d} and H_{+d} :

$$X_+ \approx W_+ \cdot H_+. \quad (4)$$

Here, subscript “+” stands for nonnegative constraints. The parameter d is a low dimensional spatial dimension that approximately describes the raw data. d should meet the requirement “ $(m+n)d < mn$.” For the solution of formula (4), the product of matrices W and H is approached gradually by the original matrix X . Euclidean distance is usually used to represent the error between WH and X . The error function is shown in

$$\begin{aligned} E(X \parallel WH) &= 0.5 \cdot \|X - W \cdot H\|_F^2 \\ &= 0.5 \cdot \sum_{ij} (X_{ij} - W_i \cdot H_j)^2. \end{aligned} \quad (5)$$

Here, the matrices X , W , and H are nonnegative matrices. When the minimum of formula (5) is obtained, the error between matrix X and matrix WH is minimum. Lee and Seung gave the iterative rules of the corresponding upper formula such as

$$\begin{aligned} W_{ik} &\leftarrow W_{ik} \cdot \frac{X \cdot H^T}{W_{ik} \cdot H \cdot H^T}, \\ H_{ik} &\leftarrow H_{ik} \cdot \frac{W^T \cdot X}{W \cdot W^T \cdot H_{ik}}. \end{aligned} \quad (6)$$

W and H are iterated over the two formulas above. The iteration ends when WH converges. NMF method is completed. However, the traditional NMF method cannot meet the needs of signal representation. The new iterative method needs to be carried out according to the actual situation.

3.3. *GAEMD-NMF*. The accuracy of the traditional NMF method is not satisfactory. Therefore, this paper uses the combination of EMD and NMF algorithm for signal representation.

The objective function is redefined as follows:

$$\begin{aligned} E_1(\widehat{X}_t \parallel f(t)) &= 0.5 \cdot \|X_t - f(t)\|_F^2 \\ &= 0.5 \cdot \sum_{ij} (X_{ij} - f(t))^2, \\ E_2(\widehat{X}_l \parallel f(l)) &= 0.5 \cdot \|X_l - f(l)\|_F^2 \\ &= 0.5 \cdot \sum_{ij} (X_{ij} - f(l))^2. \end{aligned} \quad (7)$$

In order to facilitate the convergence calculation, the rotation matrix is defined by the four-element number. It is as shown in

$$R = \begin{bmatrix} 1 - (q_2^2 + q_3^2) & 2(q_1q_2 - q_3q_0) & 2(q_1q_3 + q_2q_0) \\ 2(q_1q_2 + q_3q_0) & 1 - (q_1^2 + q_3^2) & 2(q_2q_3 - q_1q_0) \\ 2(q_1q_3 - q_2q_0) & 2(q_2q_3 + q_1q_0) & 1 - (q_1^2 + q_2^2) \end{bmatrix}. \quad (8)$$

Here, $Q = q_0 + q_1 \cdot i + q_2 \cdot j + q_3 \cdot k$. Q represents quaternion. By adjusting an expression, formula (9) is as follows:

$$\widehat{X} = \begin{bmatrix} f_\infty(t) \\ f_\infty(l) \\ F_\infty(t, l) \\ 1 \end{bmatrix}^T = \begin{bmatrix} f(t) \\ f(l) \\ F(t, l) \\ 1 \end{bmatrix}^T \cdot \begin{bmatrix} & \Delta f(t) \\ R & \Delta f(l) \\ & \Delta F(t, l) \\ 0 & 0 & 0 & 1 \end{bmatrix}. \quad (9)$$

The GA method is used to optimize the processing of the EMD-NMF method.

(1) Each row or column of the signals X and \widehat{X} is regarded as a population.

(2) The entire matrix is normalized.

(3) The variation convergence step of $\Delta f(t)$, $\Delta f(l)$, and $\Delta F(t, l)$ is 0.01. The convergence step of q_0 , q_1 , q_2 , and q_3 is 0.1.

(4) According to the sample input, we establish the fitness function as shown in

$$J = 0.5E_1 + 0.5E_2, \quad (10)$$

where J is fitness.

(5) If the fitness is reduced, it will inherit the parameter results. If the fitness is enhanced, it will change the parameter results.

4. Experiments

The Φ -OTDR instrument in this paper is the NBX-S3000 instrument from the Japanese Nebrex company. The instrument is shown in Figure 4.

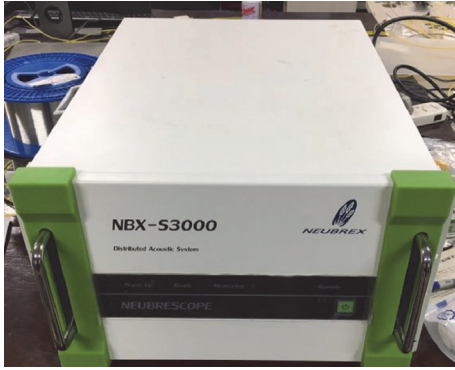


FIGURE 4: Physical picture of Φ -OTDR instrument.



FIGURE 5: A physical picture of five hammers on a knocker.

The actual parameters of the device are as follows:

- (1) Sampling rate: 4000 Hz
- (2) Recording time: 10 s
- (3) Spatial resolution: 0.1 m
- (4) Recording distance: 10 m

The vibration source uses standard vibratory equipment.

Figure 5 is a physical picture of 5 percussion hammers on the knocker. Figure 6 is a physical picture of the knocker.

In order to restrain the environmental noise and ensure the good vibration effect, the anechoic chamber is selected to test. The specific experimental environment is shown in Figures 7 and 8. In Figure 7, the fiber clings to the ground. The instrument is placed on the damping table in Figure 8.

The effects in each observation position on the fiber are shown in Figure 9.

4.1. Signal Extraction Experiment. After encoding and extracting features by the 2D-TESP method, the results are used in the popular clustering algorithms. Popular clustering algorithms are K -means clustering, hierarchical clustering, and spectral clustering. The main work of the first half of this paper is signal extraction. Therefore, clustering targets are limited to two cases: "signal" and "no signal." We compare the effects of the 5 cases. These five situations are "extreme value 29 characters," "extreme value 13 characters," "inflection point 29 characters," "inflection point 13 characters," and "extreme point + inflection point matrix." The clustering accuracy of each case is shown in Table 5. Part 1 in Table 5 is the average accuracy of the signals from 4.4 to 4.6 meters and from 5.9 to 6.1 meters on the fiber. Part 2 in Table 5 is the signal on the fiber from 4.7 meters to 5.8 meters.

Some conclusions can be drawn from the accuracy of Table 5. The 2D-TESP algorithm is the best of the five



FIGURE 6: A physical picture of a knocker.



FIGURE 7: Scene of laying fiber.

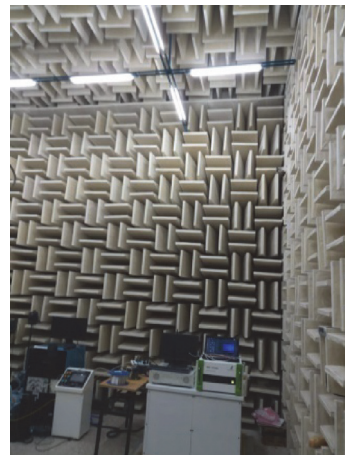


FIGURE 8: Scene of lab.

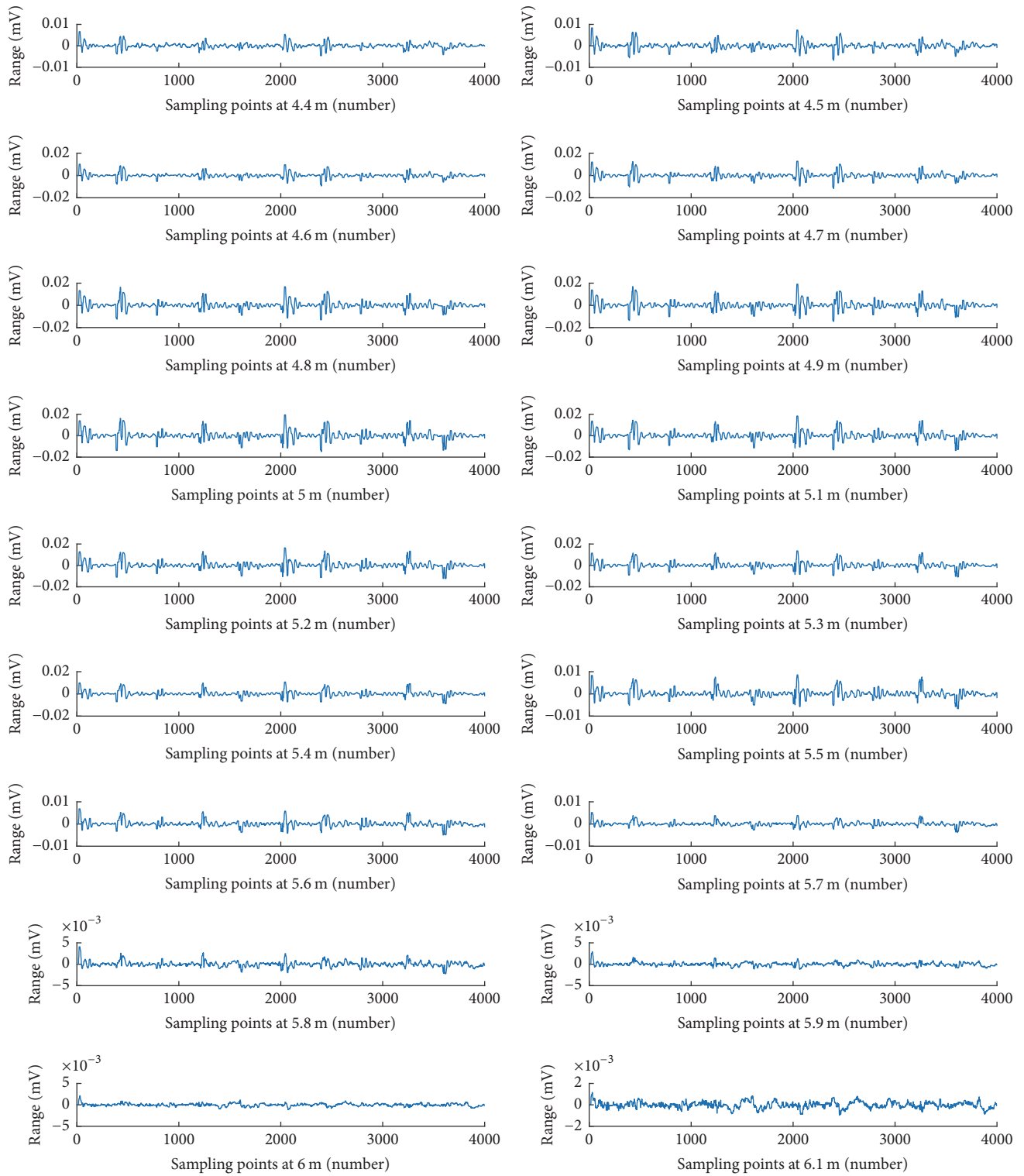


FIGURE 9: Time-domain vibration signals of each point in the effective range.

encoding methods. Spectral clustering is the best of the three clustering methods. In the case of good SNR, the accuracy of the 2D-TESP algorithm is about 0.5% higher than that of the traditional TESP algorithm. But in the case of poor SNR, the accuracy of the 2D-TESP algorithm is about 8% higher

than that of the traditional TESP algorithm. In the case of strong and weak SNR, the accuracies of 2D-TESP algorithm are relatively close. They differ by about 1 percentage point.

In this section, what is the best sort of coding in the improved TESP? The results obtained are shown in Figure 10.

TABLE 6: Comparison of correct rates under different SNRs and different methods.

| Number | Name | Poor SNR | | | Good SNR | | |
|--------|---------|----------|-------------------------|---------------------|----------|-------------------------|---------------------|
| | | K-means | Hierarchical clustering | Spectral clustering | K-means | Hierarchical clustering | Spectral clustering |
| (1) | 2D-TESP | 93.12% | 94.22% | 96.12% | 94.72% | 96.12% | 96.82% |
| (2) | FFT | 87.21% | 87.95% | 88.45% | 92.14% | 92.71% | 93.25% |
| (3) | WT | 89.37% | 89.79% | 90.12% | 92.72% | 92.99% | 93.65% |
| (4) | HHT | 90.25% | 90.97% | 91.85% | 92.84% | 93.12% | 93.89% |

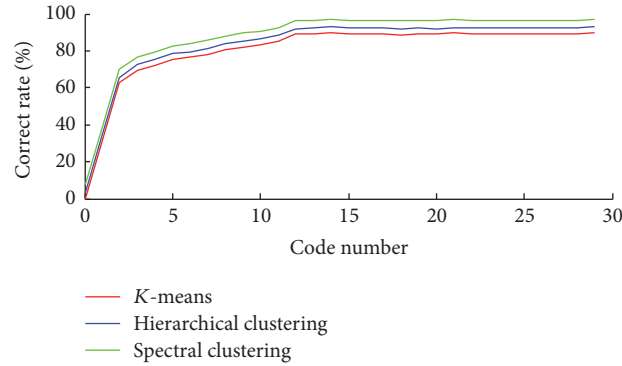


FIGURE 10: Comparison of the number of coded characters.

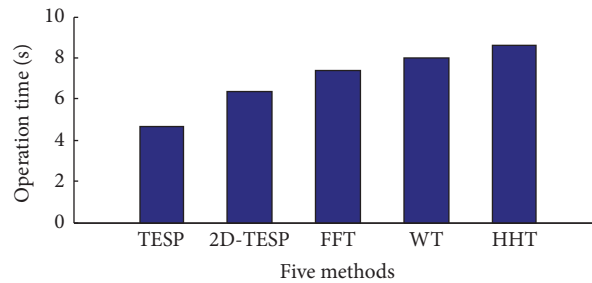


FIGURE 11: Operation time comparison among different methods.

From Figure 10, the correct rate between 13 and 29 characters is almost the same. But in 13 characters, it will have a certain effect on the accuracy. The accuracy rate tends to decrease linearly within 3 characters.

In order to verify the quality of this method, the method and another three methods are compared in the paper. Comparison is also made between three clustering methods and two different SNR situations. The results are shown in Table 6.

Some conclusions can be drawn from the accuracy of Table 6. The 2D-TESP algorithm is the best of the four methods. Spectral clustering is still the best of the three clustering methods. In the case of good SNR, the accuracy of the 2D-TESP algorithm is about 1.5% higher than that of the other algorithms. But in the case of poor SNR, the accuracy of the 2D-TESP algorithm is about 4% higher than that of the other algorithms. The method not only has better accuracy, but also has shorter operation time. The same set of signals is made in the experiments. The signal's size is 1 MB. The PC has 1.6 GHz * 4 clocked CPU and 8 G memory. Matlab software is used on this PC. The results are shown in Figure 11.

As shown in Figure 11, the method in this paper is superior to several other methods. Because the method is only computing in the time domain, its operation time is about 1 s higher than FFT, about 1.2 s higher than WT, and about 1.5 s higher than HHT.

4.2. Signal Expression Experiment. Since the Φ -OTDR signal is 3D data, the expression of the signal needs to be seen from the length axis and the time axis.

4.2.1. Positioning Problem on Length Axis. Figure 12 shows the state of the fiber with one vibration source. The vertical intersection point between the vibration source and the optical fiber is the strongest point of vibration.

There are five hammers with equal intervals on the knocker. The striking distance between two strikes is 10 cm. The five signals are not the same on the time axis. Five different signals need to be separated. The result is shown in Figure 13.

The spacing of the two hammers on the length axis is fixed as 10 cm. The five hammers have four pitches. The specific values of the four distances under the four methods are

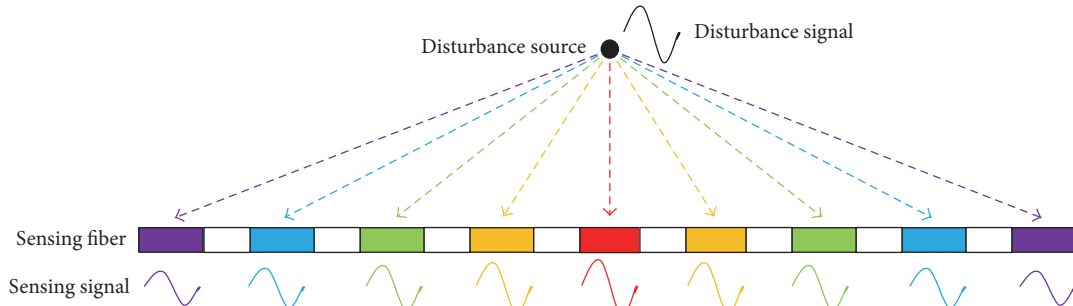


FIGURE 12: Perceptual model on length axis.

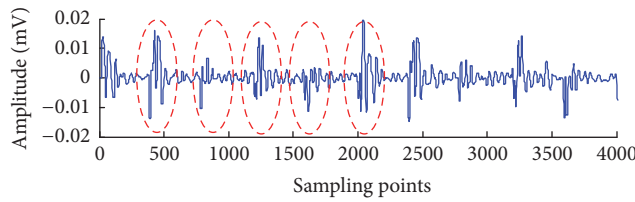


FIGURE 13: Five different signals of hammers.

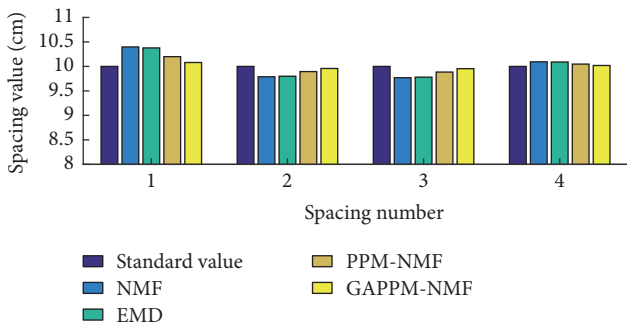


FIGURE 14: Comparison of positioning performance of four different methods on length axis.

compared. The result is shown in Figure 13. The four methods are NMF, EMD, EMD-NMF, and GAEMD-NMF.

As you can see from Figure 14, the GAEMD-NMF method works best. The EMD-NMF method has good performance and the NMF and EMD methods have the worst performance. After 100 sets of trial and error, the error range between the four methods is as shown in Figure 15.

From Figure 15, the GAEMD-NMF method in this paper is the best method for the four spacings. At the same time, the range of error fluctuation is also minimum. The range of error fluctuations in GAEMD-NMF is reduced by half compared with EMD-NMF and by 1/3 compared with NMF and EMD. The error range of the GAEMD-NMF method at 4 distances is from -0.1 cm to 0.1 cm.

4.2.2. Vibration Modes of Signals on Time Axis. The most important thing about the performance of signal on time axis is whether the spectrum analysis is consistent or not. In this

paper, a high-precision vibration sensor is arranged along the fiber. The sensor signal, the original signal, NMF, EMD, EMD-NMF, and GAEMD-NMF are compared in power spectrum. The result is shown in Figure 16. The method which compares the power spectrum similarity between different signals in this paper is as follows.

- Step 1.* Each ten Hz are noted as a frequency segment.
- Step 2.* The accumulated energy per frequency segment is calculated.
- Step 3.* The total energy of signal is calculated.
- Step 4.* Each energy is divided by the total energy. The corresponding percentage of each segment is got.
- Step 5.* The probability fluctuation of each segment between two signals is calculated.
- Step 6.* These probability fluctuations are summed by absolute values.
- Step 7.* The sum of the fluctuation probability is reduced by 1. The result is probability value of the similarity.

From Figure 16, several experimental results are as follows.

- (1) There is large high-frequency noise in the original signal. The same performance is in the treated signal by NMF method and EMD method. This shows that the signal-to-noise separation is poor.
- (2) There is no high-frequency noise in the EMD-NMF and GAEMD-NMF. This shows that the signal separation is in good condition.

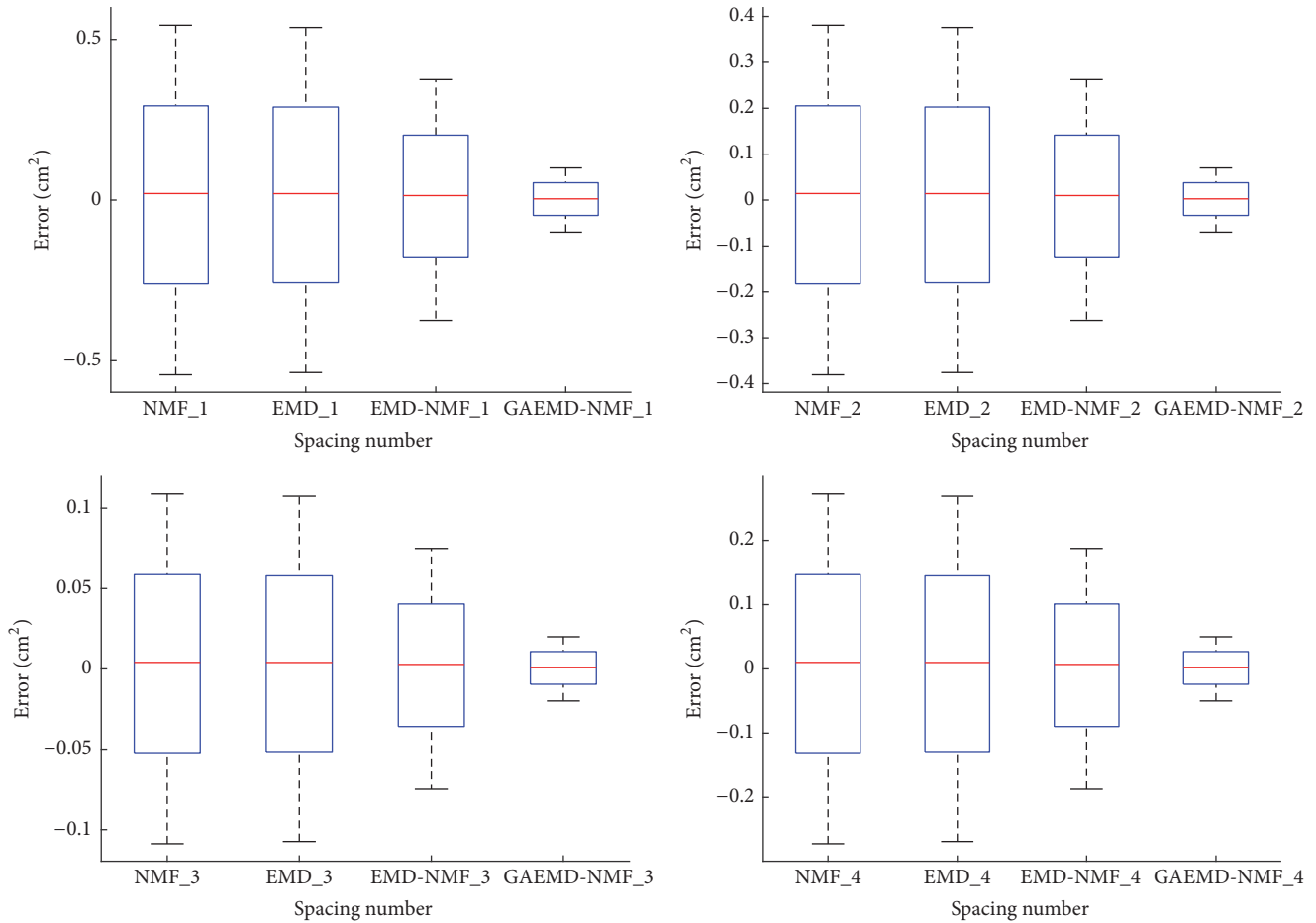


FIGURE 15: Error fluctuation on four distances by four different methods.

(3) The trends of the spectrogram of EMD-NMF, GAEMD-NMF, and sensor signals are consistent. This shows the validity of this method.

(4) The spectrograms of the original signal, the EMD method, and the NMF method are not quite consistent with the other three classes. This shows that the signal expression method is not ideal.

(5) Because the device is different, there may be a difference in the effective value of the power spectrum. Therefore, each frequency segment of the power spectrum is normalized. The similarity between GAPPN-NMF and sensor is 95.63%. The similarity between GAEMD-NMF and sensor is 95.63%. The similarity between EMD-NMF and sensor is 90.74%. This shows that the GAEMD-NMF method is 5.11% higher than the EMD-NMF method.

5. Conclusion

In this paper, we study the information representation of Φ -OTDR distributed vibration signals, and the main conclusions are as follows.

(1) The improved 2D-TESP signal extraction method has good signal extraction effect. The number of coded characters is reduced and the dimension is extended. This will effectively reduce redundancy and increase effectiveness. Particularly, it

has good signal extraction effect on the fiber point with poor SNR.

(2) The improved GAEMD-NMF signal expression method has a good expression effect on the length axis. Because the new method takes into account the characteristics of data model, it is easier to locate the strongest point of the signal in the positioning process. The positioning error effect is effectively suppressed.

(3) The improved GAEMD-NMF signal expression method has good expression effect on the time axis. Because the new method takes into account the characteristics of mechanism model, the vibration model is closer to the theoretical model. The result is compared with the high-precision sensor, and the spectrogram has a great similarity.

Conflicts of Interest

The authors declare that there are no conflicts of interest regarding the publication of this paper.

Acknowledgments

This work was partially supported by the National Natural Science Foundation of China (no. 61627816 and no. 61503034), the National Key Technology R&D Program

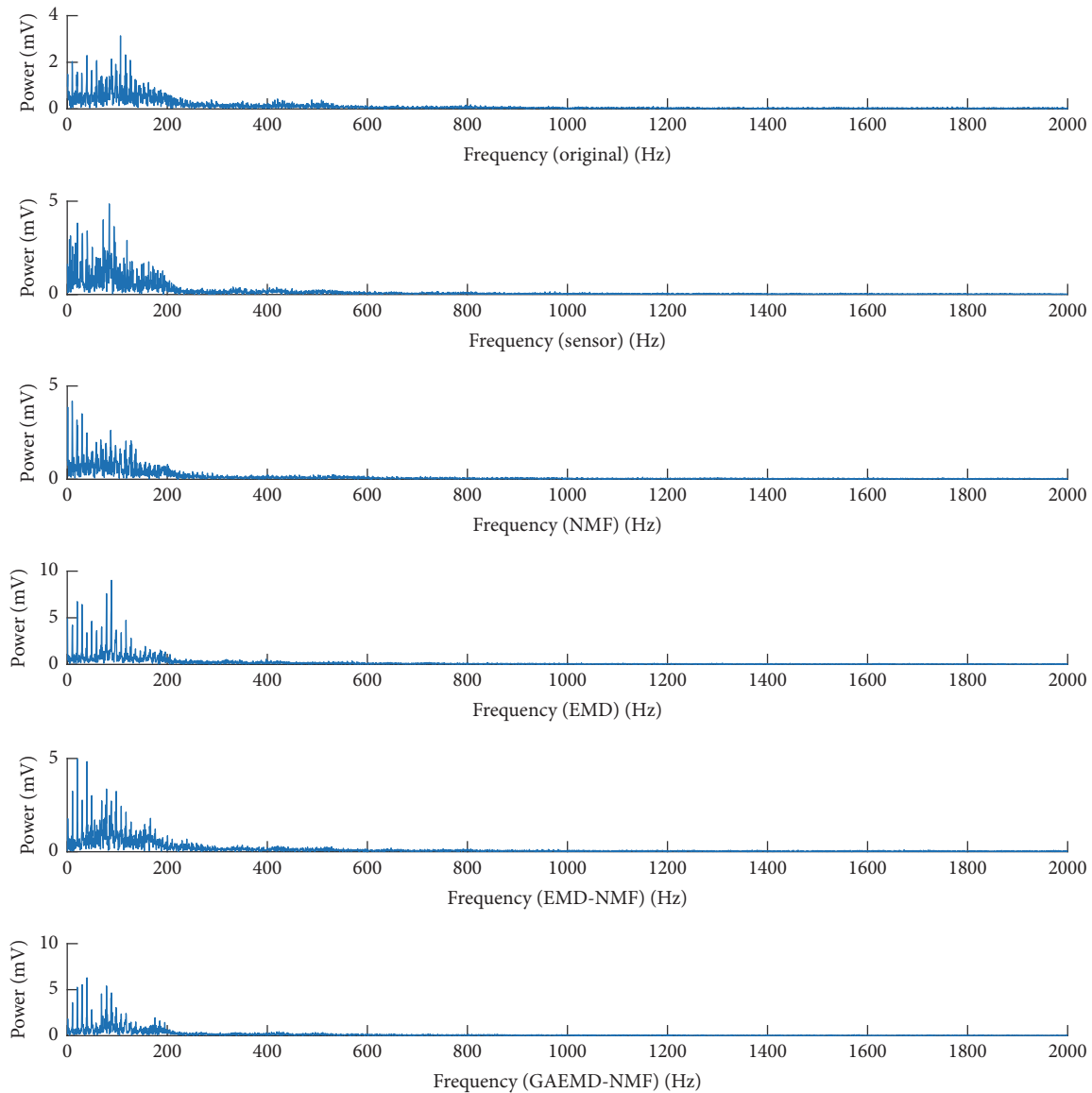


FIGURE 16: Comparison of power spectrum between four different methods, sensor signal, and original signal.

of China (no. 2015BAK40B03 and no. 2016YFC0701309), and Subproject of Key Project of Beijing, China (no. D161100004916002 and no. Z171100002417022).

References

- [1] J. A. Bucaro and E. F. Carome, "Single fiber interferometric acoustic sensor," *Applied Optics*, vol. 17, no. 3, pp. 330–331, 1978.
- [2] J. C. Juarez, E. W. Maier, K. N. Choi, and H. F. Taylor, "Distributed fiber-optic intrusion sensor system," *Journal of Lightwave Technology*, vol. 23, no. 6, pp. 2081–2087, 2005.
- [3] P. Potočník and E. Govekar, "Semi-supervised vibration-based classification and condition monitoring of compressors," *Mechanical Systems and Signal Processing*, vol. 93, pp. 51–65, 2017.
- [4] C. Delpha, D. Diallo, and A. Youssef, "Kullback-Leibler Divergence for fault estimation and isolation: Application to Gamma distributed data," *Mechanical Systems and Signal Processing*, vol. 93, pp. 118–135, 2017.
- [5] J. Ma, F. Xu, K. Huang, and R. Huang, "GNAR-GARCH model and its application in feature extraction for rolling bearing fault diagnosis," *Mechanical Systems and Signal Processing*, vol. 93, pp. 175–203, 2017.
- [6] H. Liu, J. Zhang, Y. Cheng, and C. Lu, "Fault diagnosis of gearbox using empirical mode decomposition and multi-fractal detrended cross-correlation analysis," *Journal of Sound and Vibration*, vol. 385, pp. 350–371, 2016.
- [7] K. A. Alhazza, "Adjustable maneuvering time wave-form command shaping control with variable hoisting speeds," *Journal of Vibration and Control*, vol. 23, no. 7, pp. 1095–1105, 2017.
- [8] H. Gao, L. Liang, X. Chen, and G. Xu, "Feature extraction and recognition for rolling element bearing fault utilizing short-time fourier transform and non-negative matrix factorization," *Chinese Journal of Mechanical Engineering*, vol. 28, no. 1, pp. 96–105, 2015.

- [9] B. Li, P.-L. Zhang, H. Tian, S.-S. Mi, D.-S. Liu, and G.-Q. Ren, "A new feature extraction and selection scheme for hybrid fault diagnosis of gearbox," *Expert Systems with Applications*, vol. 38, no. 8, pp. 10000–10009, 2011.
- [10] B. Li, P.-L. Zhang, D.-S. Liu, S.-S. Mi, G.-Q. Ren, and H. Tian, "Feature extraction for rolling element bearing fault diagnosis utilizing generalized S transform and two-dimensional non-negative matrix factorization," *Journal of Sound and Vibration*, vol. 330, no. 10, pp. 2388–2399, 2011.
- [11] B. Li, P.-L. Zhang, S.-B. Liang, Y.-T. Zhang, and H.-B. Fan, "Feature extraction for engine fault diagnosis utilizing the generalized S-transform and non-negative tensor factorization," *Proceedings of the Institution of Mechanical Engineers Part C: Journal of Mechanical Engineering Science*, vol. 225, no. 8, pp. 1936–1949, 2011.
- [12] A. Rai and S. H. Upadhyay, "Bearing performance degradation assessment based on a combination of empirical mode decomposition and k-medoids clustering," *Mechanical Systems and Signal Processing*, vol. 93, pp. 16–29, 2017.
- [13] M. Sher, N. Ahmad, and M. Sher, "TESPAR feature based isolated word speaker recognition system," in *Proceedings of the 18th International Conference on Automation and Computing (ICAC '12)*, pp. 318–321, September 2012.
- [14] Y. Wang, X. Wu, X. Li, and J. Zhou, "Vehicle type recognition in sensor networks using improved time encoded signal processing algorithm," *Mathematical Problems in Engineering*, vol. 2014, Article ID 142304, 8 pages, 2014.
- [15] Y. Wang, W. Li, Y. Zhang, W. Zhang, Z. Li, and J. Zhou, "Vehicle sound signal recognition in border surveillance based on improved TESP algorithm," *Journal of Sichuan University*, vol. 46, no. 2, pp. 122–127, 2014.
- [16] Y. Wang and J. Zhou, "Vehicle type recognition in WSN based on ITESP algorithm," in *Proceedings of the 10th IEEE International Conference on Ubiquitous Intelligence and Computing, UIC 2013 and 10th IEEE International Conference on Autonomic and Trusted Computing (ATC '13)*, pp. 668–671, December 2013.
- [17] D. D. Lee and H. S. Seung, "Learning the parts of objects by non-negative matrix factorization," *Nature*, vol. 401, no. 6755, pp. 788–791, 1999.
- [18] S. Shon, S. Mun, D. Han, and H. Ko, "Non-negative matrix factorisation-based subband decomposition for acoustic source localisation," *Electronics Letters*, vol. 51, no. 22, pp. 1723–1724, 2015.
- [19] A. Ozerov and C. Fevotte, "Multichannel nonnegative matrix factorization in convolutive mixtures for audio source separation," *IEEE Transactions on Audio, Speech and Language Processing*, vol. 18, no. 3, pp. 550–563, 2010.

Research Article

Impact of Pyrotechnics over the Architectonic Heritage

Angel T. Lloret,¹ Sandra Sendra,^{2,3} Jaime Lloret,³ Miguel Louis Cereceda,¹ and Jesus Alba⁴

¹Universidad de Alicante, Carretera San Vicente del Raspeig, s/n, 03690 San Vicente del Raspeig, Spain

²Signal Theory, Telematics and Communications Department (TSTC), Universidad de Granada, C/Periodista Daniel Saucedo Aranda, s/n, 18071 Granada, Spain

³Integrated Management Coastal Research Institute, Universitat Politècnica de València, C/Paranimf, No. 1, Grao de Gandia, 46730 Gandia, Spain

⁴Centre for Physics Technologies, Universitat Politècnica de València, Av. de Los Naranjos, s/n, 46022 Valencia, Spain

Correspondence should be addressed to Jaime Lloret; jlloret@dcom.upv.es

Received 31 May 2017; Accepted 24 July 2017; Published 29 August 2017

Academic Editor: Taesun You

Copyright © 2017 Angel T. Lloret et al. This is an open access article distributed under the Creative Commons Attribution License, which permits unrestricted use, distribution, and reproduction in any medium, provided the original work is properly cited.

The use of pyrotechnics near to the historical heritage such as walls, facades, church, or fortifications of a city is nowadays a topic of discussion. There is not a clear legislation about the use of pyrotechnics near to these buildings and how they can be affected by the expansive wave generated by the use of harquebusiers, fireworks, and cannons during the simulation of a battle. For this reason, this paper presents some practical tests that measure the vibroacoustic effect when these types of pyrotechnics are used near to the architectural heritage. In order to collect these data, we have used several sound level meters and accelerometers placed on two different scenarios. The first one was placed near to the beach and the other one was placed in a building of a narrow alley. The tests were carried out during the festival of Moors and Christians of Villajoyosa (Spain) which is a famous festival. Along these tests, we reproduce the worse cases that may affect the building, using harquebusiers shots, fireworks, and cannons shots. Results show that the house placed near to the beach does not suffer important vibroacoustic impacts. However, the old building placed in the alley is very affected.

1. Introduction

Along the Mediterranean coast, we can find hundreds of fortifications, walls, castles, and watchtowers for the defense of their territories. These elements, built around the XIV and XVIII centuries, are nowadays part of the historical heritage and, therefore, we should plead for their conservation and protection.

Due to the importance of historical events, many cities where these architectural elements are located generally hold parties that reproduce some of the battles to commemorate them. These recreational activities are usually carried out in the historical center of the city, taking advantage of the beauty of the landscape which is, at the same time, a tourist attraction that brings great economic benefits to them [1, 2].

The reproduction of these battles is often done using different types of pyrotechnics, ranging between fireworks, firecrackers, handguns, and small guns. The explosion and

the deflagration of this type of pyrotechnic generally generate a displacement in form of mechanical wave that impact the facades. Nevertheless, in the related literature, its effect on the old buildings has not been quantified.

In order to quantify these effects, distributed sensor networks can be used over throughout the monitoring area. A sensor or transducer [3] is an electronic device which is capable of translating the variation of a physical parameter into electrical signals that are processed by the sensor nodes. Many of these nodes allow us to implement a wireless sensor network (WSN) [4]. WSNs are nowadays a hot topic due to their wide range of applications. They can be used for environmental monitoring, military applications, precision agriculture, domestic applications or tracking people and objects, and buildings monitoring [5]. A set of sensors deployed in a home can give us many types of information such as the structural aging, fatigue and damage materials, gas leaks, fires, inadequate humidity, and temperature values.

An exhaustive measurement process can provide valuable information to the researchers for preventing building problems [6] and allow us to take decisions about our habits, so as not to worsen the situation of a building or to maintain its level of conservation, as the case of the historical heritage. Analyzing the existing literature, we can affirm that there are very few initiatives related to the deployment of sensor networks for the monitoring of historical heritage. However, the sensors are widely used in the processes of surveillance and conservation of art [7] and fresh [8].

Therefore, the effect of the use of pyrotechnic near to these buildings must be monitored and quantified. This paper presents a practical study to determine the impact that harquebuses and fireworks can generate on the historical heritage. In order to do it, we have selected two different scenarios where these kinds of pyrotechnics are used. From these tests, we measure both the acoustic and vibration effect over the buildings. On the one hand, the acoustic impact can be understood as the magnitude of mechanic wave that impacts the building. Because these waves displace the air present in the medium, the building registers some small structural movements. To measure these, we can use accelerometers placed along the surface under study and then process the data to extract the vibration levels. With these 2 parameters, we can evaluate the vibroacoustic effect as a function of the facade height. The selected city is Villajoyosa (Spain), which is famous because of its festival of Moors and Christians. To measure these effects, we used several sound meters and vibration sensors installed on the façade. For the first scenario, which is a house placed near to the beach, three different sound sources were used: cannons, shots from harquebusiers, and shots from boats. The second scenario is an old building placed in a narrow alley. In this case, 6 harquebuses and blunderbusses were used to perform the shots. With the results, we sketch the maps of the acoustic effect and the vibration effect over the facade. The results show that the impact over the facade depends on the place where there is a shot and the building height.

The rest of this paper is structured as follows. Section 2 presents several related papers where researchers performed some studies about the impact of acoustic waves over buildings. Section 3 explains the features of the scenarios used to carry out the tests, as well as the tools, sensors, materials, and sound meters used to perform our tests. Section 4 defines the experiments carried out and their results. Finally, Section 5 shows the conclusion and future research line to continue our research.

2. Related Works

Generally, WSNs in buildings are used for monitoring indoor variables, for taking care of their inhabitants [9], and for developing applications related to Internet of Things (IoT) [10]. There are very few practical studies about old buildings monitoring. We have only found few old studies about the use of harquebuses and some acoustic impact analyses on buildings related to the insulation characteristics of dwellings to ensure the well-being of its inhabitants [11]. This section

shows some previous work in which the authors have analyzed the effect of the sound pressure on buildings.

Firstly, the acoustic characteristics of harquebuses and blunderbusses used in this type of festivities are analyzed. The work was carried out by Marco Sanjuán in 1996 [12]. He performed several measures in relation to the sound levels of these types of weapons. The study only covered certain explosives and weapons' calibers. However, these results offer us a basic indicator to start our study of the received sound pressure over the buildings.

Regarding the deployment of networks in buildings, Bennett et al. [13] presented a sensor network deployed in a building to monitor the structural movement of the buildings generated by the passage of undergrounds and trams located in London and Prague. The document identifies the critical factors that should be taken into account in the design of a WSN in terms of energy constraints and communication issues between nodes. Throughout the work, the authors identified the problems in the deployment of the network in both locations and try to demonstrate with their tests the feasibility and advantages of using WSNs in underground environments.

Späh et al. [14] conducted a study about the impact of acoustic waves on houses made of wood. In this case, the authors did not use a sensor network to perform their measurements, but they show the effect suffered by these types of dwellings. In fact, these measures were carried out under the AcuWood project, whose main objective was to find technical descriptors for different sound sources taking into account construction traditions and cultural differences of several European countries. In order to obtain the results, the authors used correlation techniques to relate the different technical descriptors of the different types of constructions with the obtained acoustic results. The results can be used as a reference model in the evaluation of certain noise sources.

Finally, Yu and Kang [15] presented a study to characterize the effects of the acoustic impact on different materials used in architecture. The study was conducted in various houses with different structural characteristics. For each building, the authors compared different types of materials commonly used in wall covering and different types of glazing. The results showed the importance of considering the environmental sustainability of acoustic materials when building a house.

There are very few works where the effects of vibration are contemplated, in addition to the acoustic impact. In fact, the only work we have found is the one presented by Klos in [16]. In this case, the author carried out a study that analyzed the vibroacoustic response of buildings due to exposure to a sonic pump. In the experiment, more than 100 transducers were installed in various bedrooms of a house. In addition, accelerometers were randomly placed on walls, windows, and ceilings at rooms and around the house. With the results, the author was able to characterize the response of the different materials in terms of reverberation time and isolation level.

We have not found any study that relates the use of gun replicas in this type of centenary celebrations and its effect on the cultural built heritage. We believe that it is important to keep these celebrations. Moreover, we also believe that it



FIGURE 1: Moorish troops navigating near the coast.

is necessary to preserve the monumental remains and our historical heritage and, therefore, we wish to analyze and characterize how historical buildings may be affected by the use of these types of fireworks in order to propose corrective measures.

3. Scenario and Material Description

In order to carry out our test bench, two different scenarios have been selected. The first scenario is placed on the beach where it recreated the night battle during which the Moorish troops land on the beach and the Christian troops try to repel them. The second scenario has been specially selected for reproducing the worst case, where Moorish and Christian weapons are shot near the old buildings. For each case, different materials are used. This section explains the details of each scenario and the material used.

3.1. Scenario 1: Night Battle. The night battle takes place throughout the night. During the night, the Moorish troops navigate with their ships near the coast and make different shots towards the coast (Figure 1).

These shots are acoustically imperceptible due to the distance (Figure 2(a)). In response, from the sand, several shots are fired by cannons (Figure 2(b)) and harquebusiers (Figure 2(c)). Cannons and harquebusiers are perceived from homes and, therefore, we want to measure the acoustic impact on them.

In the sand of the beach, we can distinguish 2 different zones. There are 3 cannons (see Figure 3) whose characteristics and dimensions are shown in Table 1. Cannon is a hollow piece of metal or another material that forms a cane, used in artillery, which has great length with respect to its caliber. Formerly, they were used to shoot bullets and shrapnel but they serve nowadays to reproduce shots in celebrations exclusively using gunpowder that produces great blares. In addition, we also distinguish a battle area where the harquebusiers with their guns are placed. Figure 4 shows the battle area and the cannons' area with the distance up to the position of measurement.

3.2. Scenario 2: Shots in the Narrow Alley. The second part of these tests is performed in an uninhabited house placed in a pedestrian street in the historic city center. The historic city center contains many historical sights of the city. These include defensive walls built between 1551 and 1565 to repel Berber attacks, a watchtower built around the 15th century, and several colorful and old buildings that characterize this

TABLE 1: Size of cannons.

| | Length of cannon | Inner length of cannon | Caliber |
|-----------|------------------|------------------------|---------|
| Cleopatra | 85 cm | 78 cm | 12 cm |
| Art Mora | 106 cm | 68 cm | 18 cm |
| Art Islam | 60 cm | 46 cm | 11 cm |

city. Figure 5 shows a section of Villajoyosa city (in Alicante province, Spain) and the area of the second scenario where the tests have been carried out.

The building selected for the second test is an old rectangular-base building. The foundation of this dwelling sits exactly at the base of the dwelling, while the structural support is made in load walls which have thick walls above normal. The structural system of the surface based on the walls of load has been made with the masonry mortar. The load walls that form the outer faces have a mortar of cement and sand and it is covered by a typical plaster of concrete and sand. The load-bearing thickness walls decrease as the height of the building increases. Finally, the building presents a staircase that communicates with the floors. Figure 6 shows the image of the building where the measurements were taken.

Figure 7 shows the scale drawing of the scenario where the tests are performed. This image also shows the position of the harquebusiers and the positions where the sound level meters and vibration sensors are located. Each harquebusier is identified as "Harquebusier_X" where X indicates the harquebusier. The distance between harquebusiers is 2 m and the distance between the building and harquebusiers is 3 m. Sound level meters are identified as "Sono_Y" where Y indicates the device. This nomenclature is used in the rest of the paper.

Regarding the location of the sensors, the 4 sound level meters (Sono_3, Sono_4, Sono_5, and Sono_6) are located inside the building, at 2 meters from the inside of the facade, window, or access door. With this distance we ensure that the reflections of the reflecting surfaces of the building do not affect the measurement records. Additionally, Sono_2 is used as dosimeter, that is, to measure vibrations. This dosimeter has been used to check some strange movement in the building which could jeopardize the integrity of the researchers and collaborators who were helping during the tests.

The vibration sensors take measurements of the three axes. They are fixed to the outside of the facade with a support that gives freedom of movement to the sensors. Figure 7 also shows the location of the vibration sensors by small red blocks. Finally, we can see that the section of surface that is monitoring comprises a space of 6 m height per 6 m width.

To perform the shots, 6 different weapons have been used. Table 2 shows the features of each weapon as well as their sizes and brands.

3.3. Materials and Tools. This subsection explains the features of the weapons, the features of the black gunpowder used with these weapons, and the instruments and sensors used to

TABLE 2: Features of weapons used during these tests.

| | Harquebuses | | | | | |
|--------------------|----------------|-------------|----------------|----------------|-------------|-------------|
| | 1 | 2 | 3 | 4 | 5 | 6 |
| Kind of weapon | Muzzle-loading | Blunderbuss | Muzzle-loading | Muzzle-loading | Blunderbuss | Blunderbuss |
| Brand | BOPE | ARDESA | BOPE | GIL | BOPE | ARDESA |
| Caliber (mm) | 62 | 62 | 28 | 28 | 60 | 62 |
| Barrel length (cm) | 50 | 50 | 41 | 40 | 50 | 50 |

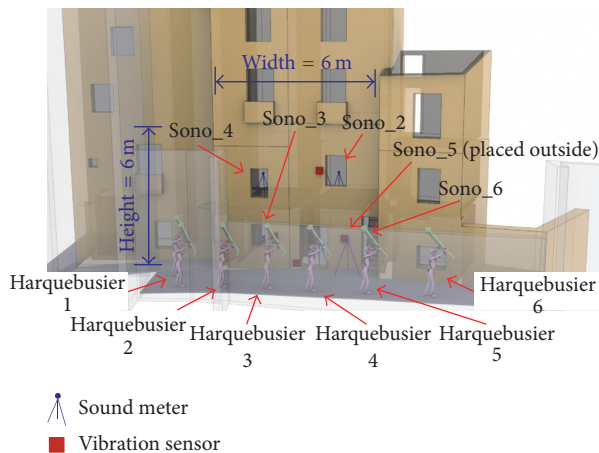


FIGURE 7: Position of harquebuses, sound level meters, and vibration sensors.



FIGURE 8: Harquebusier used in our tests.

system is used for firing these types of weapons. It consists of a mechanical actuator activated by a ball of a firing pin embedded in the chimney. This type of weapon was used by Moorish soldiers and Christians troops. The weapons are usually muzzle-loading. According to its construction and type of camera, the weapon can load from 15 g to 50 g of black gunpowder. The gun barrel has a flared appearance for easy loading. The name “harquebus” is due to the arched shape of the mouth that changed in blunderbuss to facilitate the introduction of gunpowder.



FIGURE 9: Commercial black gunpowder and detonating pistons.

3.3.2. Black Gunpowder. Black gunpowder is a mixture of sulfur, charcoal, and potassium nitrate. It cannot be considered as an explosive because the result of its reaction is in the form of deflagration in detonation. One of the main characteristics of this type of powder is the large volume of gases it produces and the high temperatures it reaches during its combustion. Unlike other explosives, its reaction speed is low and can reach speeds up to 500 m/s, depending on the caliber of the weapon. The dust of powder is very sensitive, so they are supplied in granulated form after adding graphite (which prevents electrostatic charges). To carry out the tests performed in these experiments, we have used black gunpowder marketed by the company Maxam Outdoors (See Figure 9) whose main features are the following ones:

- (i) amount of KNO_3 : 74%
- (ii) grain size: From 0.35 to 1.19 mm.

3.3.3. Sound Level Meters and Sensors. The measurements of the noise levels are made with professional sound level meters. In this case, the model Type 2250 has been chosen [17]. This device can be understood as a portable analyzer capable of satisfying all measurement and analysis needs in isolation studies. Its application ranges from the traditional uses of environmental noise assessment to quality control and evaluation of the noise in the workplace of an industrial work. The Brüel & Kjaer Type 2250 performs Class 1 measurements according to international standards. This device contains a high resolution touch screen that allows easy navigation through the configuration menu to customize predefined templates according to the measurement requirements. The Brüel & Kjaer Type 2250 has a wide dynamic range that supports high amplitude noise levels and noises that are

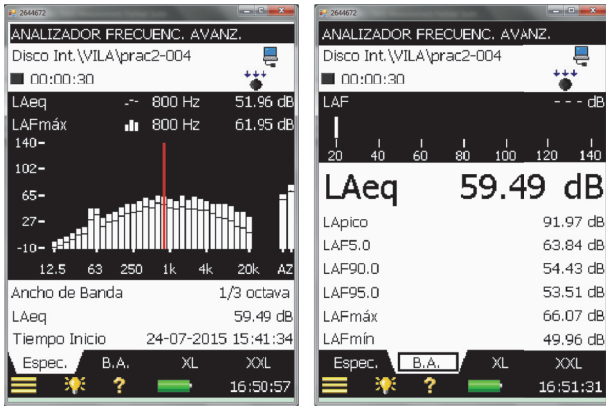


FIGURE 10: Screenshots of sound level meter Bruël & Kjaer Type 2250.

only perceived above background noise. It has a fairly large dynamic range between 20 dB and 140 dB. The device can measure and analyze data in 1/1 octave and 1/3 octave bands. Figure 10 shows some screenshots of this sound level meter that allow the user to visualize the result of the measurements in real time. On the one hand, this sound level meter is able to show measurements in real time; that is, we can move the red cursor along the frequency spectrum and check the levels of sound pressure level as a function of the frequency. We can also see the maximum value registered during the elapsed time. If we move for the next window, we can see a summary of average, minimum, and maximum values as well as the statistical values. This is the average value of sound pressure level registered during the 5%, 90%, and 95% of the measured time.

3.3.4. Accelerometer Used in Scenario 1. The Type 4374 accelerometer is a piezoelectric charge sensor encapsulated in a titanium housing [18]. It has a side connector and integral cable whose function is to connect it to the sound level meter. The Type 4374 sensor must be adhesively attached to the measuring object using beeswax. This accelerometer sensor allows the user to measure high frequency vibration levels in confined spaces and structures where it is difficult to reach. The Type 4374 sensor is based on the piezoelectric element PZ 27 and it is only capable of taking measurements on an axis. This sensor is used in the vibration measurements of scenario 1.

3.3.5. Accelerometer Used in Scenario 2. The accelerometer used in scenario 2 is a Bosch BMA056, 3-axis accelerometer [19] (see Figure 11). This kind of sensor is widely used in smartphones and smart devices because it has very high resolution (0.00390625 m/s^2). It is presented in a very small encapsulation of $3 \times 3 \times 0.95 \text{ mm}^3$. The sensor can be measure in the range of $\pm 1000 \mu\text{T}$ (for x -, y -axis) and $\pm 2500 \mu\text{T}$ (for z -axis) with a resolution of $0.3 \mu\text{T}$ and a sensitivity tolerance of $\pm 4\%$.

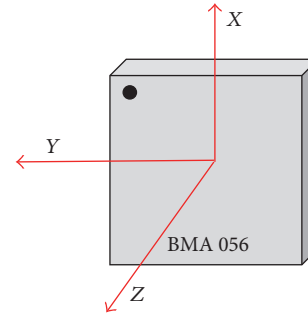


FIGURE 11: Vibration sensor Bosch BMA056- 3-axis accelerometer.

4. Measurement Results

Before starting to interpret the measured data, we should take into account a set of considerations about the acoustic measurements.

When we try to measure the noise level, we should know that the frequency weights respond to acoustic sound problems and have a great psychoacoustic component. This occurs because the human ear does not have a flat response for different frequencies based on the same sound pressure; that is, the human ear has a nonlinear frequency response to sounds.

A sound level meter is intended to approximate its responses to the human ear. An acoustic measure that does not consider these psychoacoustic parameters does not accurately reflect the measurements that disturb noisy space compared to human perception. While the sound pressure level (SPL) in dB describes the physical phenomenon, the weighted decibel level describes the existing volume.

Finally, we would like to point out that our measurements are performed without any kind of weighting, since we do not want to measure the human perception of the noise level produced by the noise sources. In our case, we want to measure the physical effect on the facade and therefore we will use the sound level meters without any weighting; that is, our sound level meter will not apply any equalization as a function of the frequency. This will give us a flat frequency response between 10 Hz and 20 kHz ± 1.5 dB, excluding the microphone response.

The results directly represent the effect we want to measure. All information concerning this type of measurement is presented in the international standard IEC 61672: 2013. Our measurements are carried out in linear weighting (which is equivalent to say that we do not use frequency weights), measured in dB, in the 1/3 octave band [20–22].

4.1. Measurement Results in Scenario 1. To perform the measurements in the first scenario, we used 2 sound level meters. The first one is used to take measurements of the noise level; the second is used to measure the vibrations. The second sound level meter is used together with the 1-axis acceleration piezoelectric sensor (Type 4374), working as a dosimeter. Figure 12 shows the position of these sound level meters while measurements are taken.



FIGURE 12: Sound level meters taking measures in Scenario 1.

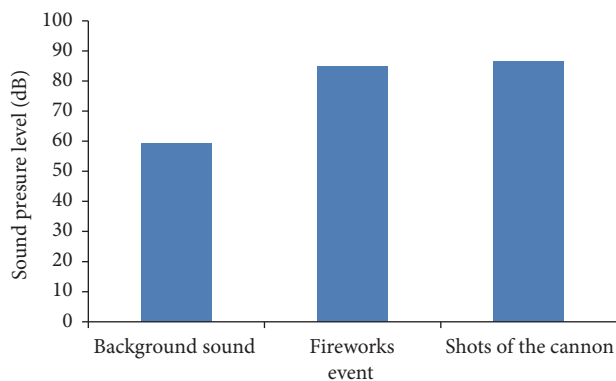


FIGURE 13: Average values of the measures performed for the 3 types of analyzed events.

To start with the measurements of the acoustic impact, it is needed to know the environmental values, that is, the temperature, speed wind, and relative humidity. This is because the acoustic waves are highly affected by them. In addition, when the wind speed is higher than 5 m/s, the acoustic measurements are not valid [23]. The parameters measured in this place are the following ones:

- (i) temperature: 28.2°C
- (ii) relative humidity: 73.3%
- (iii) speed wind: 0.4 m/s.

With these values, we can perform the tests and we will be sure that the recorded values of noise level really represent the effect of the different types of shots performed on the beach.

In order to carry out these measurements, different series of shots every 30 s are performed during which only the shot or event that we intend to monitor is perceived. After that, we calculate the average value of these measures. Figure 13 shows the average values recorded in scenario 1. As we can see, the average value of the background noise has a fairly high value (in this case around 60 dB). This value, certainly, would not allow an inhabitant of this house to rest. However, considering the type of events celebration, we can consider it as low. In relation to the fireworks and the firing of the weapons, in both cases, the average value of noise is around 85 dB.



FIGURE 14: Harquebusiers who execute the shots.

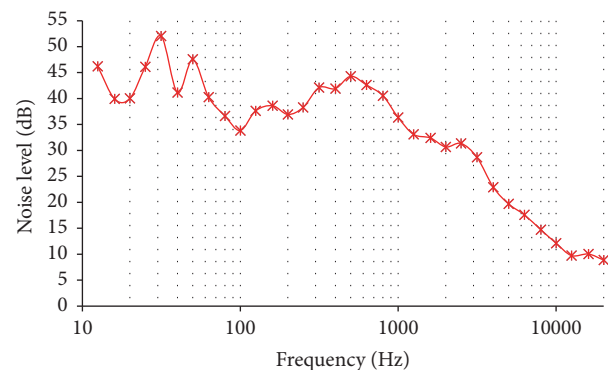


FIGURE 15: Average background sound pressure (in dB) registered in the area of shooting.

The vibration value recorded in this test has been negligible. In fact, at sensory level, the people responsible of carrying out the measures did not perceive any type of stimulus or pressure. Therefore, when we took measures on the architectural elements of the building, the result was nil.

4.2. Measurements Results at Scenario 2. First, we measured the environmental conditions. In this case, the environmental conditions measured in the alley were the following ones:

- (i) temperature: 29.1°C
- (ii) relative humidity: 75.3%
- (iii) speed wind: 1 m/s.

As the wind speed is much lower than 5 m/s, we can perform the tests and we will be sure that the registered values of noise level really represent the effect of the harquebuses on the facade. Figure 14 shows the harquebusiers in the alley prepared for firing.

The first step to analyze an acoustic activity is to check the average values of the noise levels received in the facade without the presence of the activity. In our case, the activity is translated into the presence of shots. A total of 3 shots were fired. From these values we have calculated the average value of noise level (in dB) recorded on the facade. Figure 15 shows the average value of the background noise level in dB recorded on the facade. As we observed, the maximum value of noise level is 52.5 dB at the frequency of 42 Hz. However, we also observed a rather high value (47.5 dB) compared to

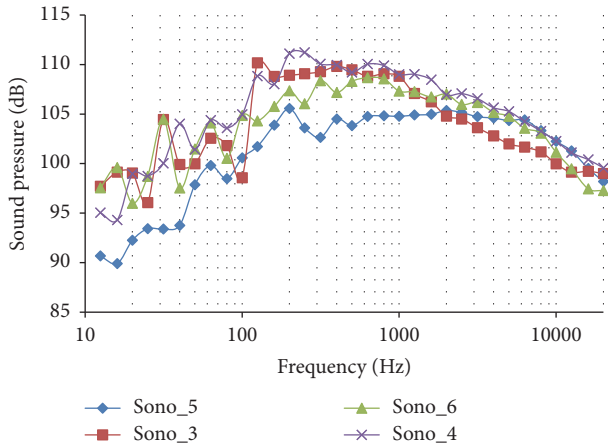


FIGURE 16: Noise level measured by the four sound level meters.

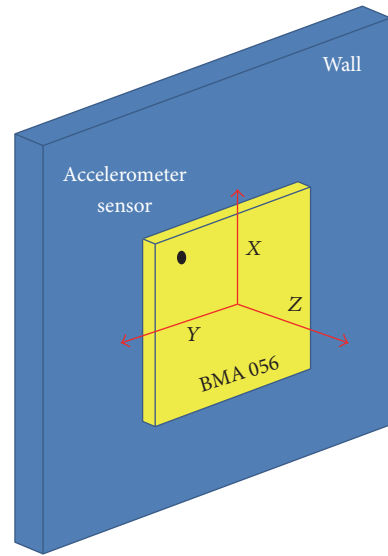


FIGURE 18: Position of the accelerometer on the facade.

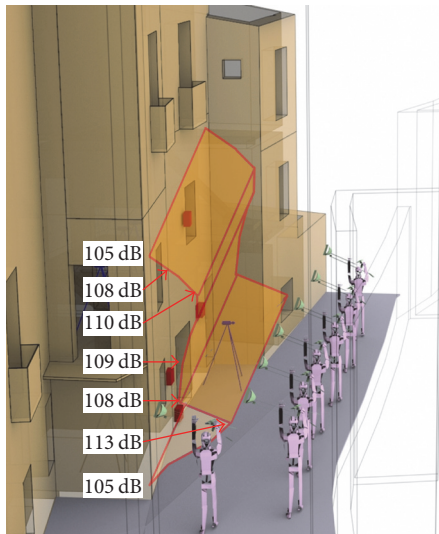


FIGURE 17: Maximum noise levels superposed on the facade.

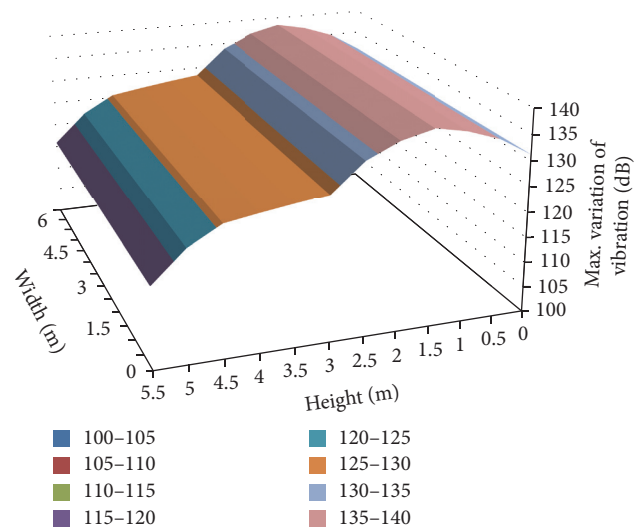


FIGURE 19: Variation of vibration in dB for z-axis.

the rest of the spectrum at 50 Hz. It is easy to conclude that the highest values of noise are located at low frequencies. The range of low frequencies is the one that generates a greater impact on the buildings and, in addition, it generally generates enough discomfort in the people, at the auditory level.

Once the background noise level is measured, we should measure the vibroacoustic impact that firing these weapons generate on the facade. Figure 16 shows the noise level measured by the four sound level meters. As we can see, the sound level meter closest to the ground floor (Sono_5) records the lowest noise level, with 105 dB, while Sono_3 and Sono_4 record values close to 110 dB. In all cases, the highest noise impact has been recorded in the range of 100–250 Hz, which can be considered as low frequencies.

Finally, in order to see more clearly the point where a greater acoustic impact is perceived, in Figure 17 we overlap the maximum values of noise level registered in each point of the facade at 310 Hz over the image of the facade. As we

can see, there are 2 points where the highest noise levels are received. The first one is located at the arquebuses height (around 1.5 m) and the second one is located at 4.5 m height.

In order to record the movements and vibrations generated in the building by the effect of the acoustic wave impacting the facade, we used 3-axis accelerometers. These devices give us information about the movements generated in the building for the X-, Y- and z-axes. However, the most important variation will be recorded on the z-axis due to the position we have placed the sensors on the wall (see Figure 18). We have processed the vibration values individually for each axis.

Figures 19, 20, and 21 show the vibration map on the facade for the z-axis, the y-axis, and the x-axis, respectively. The highest vibrations are recorded on the z-axis (see Figure 19). In addition, the highest value is recorded around

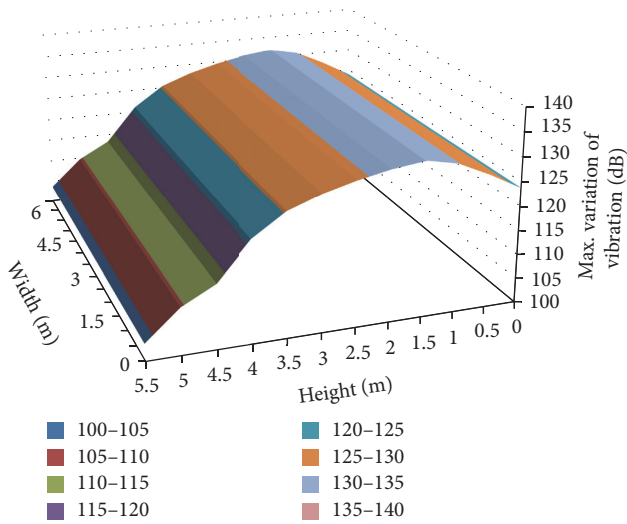


FIGURE 20: Variation of vibration in dB for y-axis.

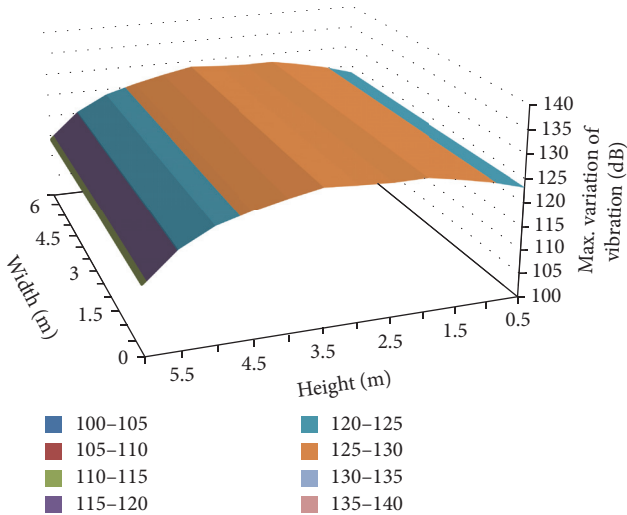


FIGURE 21: Variation of vibration in dB for x-axis.

1.5 m, with maximum value of 138 dB which corresponds to the height at which the harquebuses generate the highest noise level. The axis that registers the lowest vibration is the x-axis, with a maximum value of 130 dB at 3.5 m. height.

As we can see the axis that suffers the greatest vibration is the z-axis. Since acceleration is a vectorial magnitude, it can be measured in the three Cartesian coordinates, as we represented in Figures 19, 20, and 21. However, we can also show the combination of three axes in order to see the magnitude. Figure 22 shows the combined vibration level of three axes as a function of the facade height. Showing these results, we can see that the biggest vibration is registered at 1.5 m height.

In order to see more clearly which points of the facade recorded major movements or vibrations, we superimpose the values given in Figure 19 on the facade. Figure 23 shows the levels of vibration on the facade. In this way, we can see that the part where the greatest vibration occurs is just the

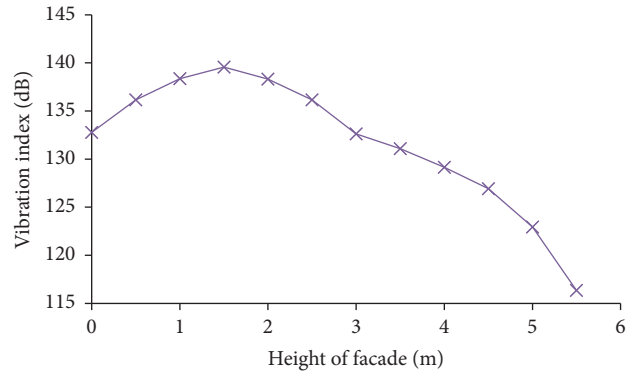


FIGURE 22: Variation of vibration in dB for x-axis.

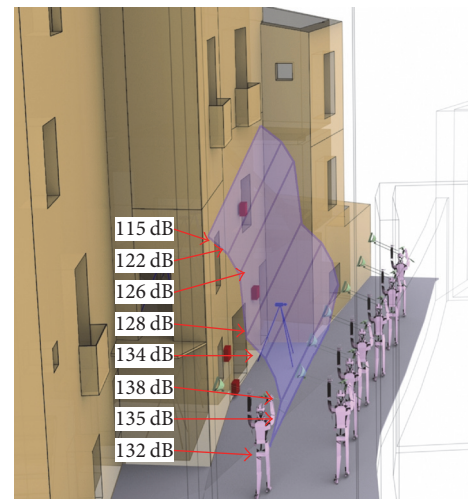


FIGURE 23: Maximum vibration values recorded on the facade.

one that corresponds with the ground floor, with a value close to 140 dB. Then, we can observe a flatter zone with vibration values close to 126–128 dB and finally the vibrations are attenuating as the height increases.

5. Conclusion

In the Spanish Mediterranean coast, during the summer season, we can find several festivals that commemorate historical events such as wars and reconquest of lost territories. During these festivals the ancient battles are replicated along the historical center of the cities. Generally, these recreations are accompanied with pyrotechnics. The European countries are the ones that conserve the major number of historical buildings such as fortresses, watchtowers, churches, and historic facades that are placed in the historical center of the cities. However, there is no study published specifying the repercussion of these recreations over these buildings.

Due to the need of keeping our architectural heritage, in this paper, we have presented a practical study about the vibroacoustic impact that different kind of pyrotechnic can generate over these buildings. In order to perform out a practical study, we used 2 different scenarios, that is, a house

placed on the beach and an old house located in a narrow alley. The measurements have been performed during the festival of Moors and Christians of Villajoyosa (in Alicante province, Spain) which is famous for this festival. In both cases, several sound level meters and vibration sensors have been placed to gather the data.

The results have shown that the celebrations placed in the beach present a very low effect over the dwelling because the effect of the acoustic waves was not perceived as vibration. However, the results shown in the narrow alley were clearly perceived as vibrations and had very high noise level. We have observed that the greatest acoustic impact is recorded at 1.5 m height (with 113 dB), although it also recorded a high noise level at 4.5 m height (with 110 dB). Regarding the vibration results, we have seen that the facade generates greater vibrations in the z-axis at 1.5 m. height, with values around 138 dB. So, there are clearly 2 areas with the greatest impact of sound pressure. This is because, during a shot, the explosion generated by the weapon has approximately been generated at 1.5–2 m height, that is, the height where we can find the weapon handle and the trigger, while the deflagration can reach several meters (up to 5–6 m) height and also causes the propagation of sound waves.

These results show that the vibroacoustic effect on the facade claddings in a bad state is high and is capable of causing detachment and human injuries. The determination of human injuries, rather than the built heritage, can be decisive for limiting these traditional celebrations in historic centers of cities and towns.

Because we have verified that the vibroacoustics effects registered in the housing of the beach do not cause an appreciable impact on the buildings, as future work we would like to perform a more exhaustive study on the house located in the narrow alley. Moreover, we would also like to focus our study on other architectural elements by implementing a wireless sensor network [6] to perform long series of measurements simultaneously in several buildings and combine the results using distributed database management techniques [24, 25].

Conflicts of Interest

The authors declare that there are no conflicts of interest regarding the publication of this paper.

References

- [1] G. J. Ashworth and P. J. Larkbam, *Building a New Heritage: Tourism, Culture and Identity in the New Europe*, Routledge Library Editions: Tourism, 1st edition, 2013.
- [2] M. Crang, "Building a new heritage: tourism, culture and identity in the New Europe," *Journal of Rural Studies*, vol. 12, no. 2, pp. 206–207, 1996.
- [3] S. Sendra, J. Lloret, M. García, and J. F. Toledo, "Power saving and energy optimization techniques for wireless sensor networks," *Journal of Communications*, vol. 6, no. 6, pp. 439–459, 2011.
- [4] S. Sendra Compte, *Deployment of Efficient Wireless Sensor Nodes for Monitoring in Rural, Indoor and Underwater Environments*, Universitat Politècnica de València, 1st edition, 2013.
- [5] M. Garcia, D. Bri, S. Sendra, and J. Lloret, "Practical deployments of wireless sensor networks: a survey," *International Journal on Advances in Networks and Services*, vol. 3, no. 1-2, pp. 170–185, 2010.
- [6] S. Sendra, A. T. Lloret, J. Lloret, and J. J. P. C. Rodrigues, "A wireless sensor network deployment to detect the degeneration of cement used in construction," *International Journal of Ad Hoc and Ubiquitous Computing*, vol. 15, no. 1–3, pp. 147–160, 2014.
- [7] N. Kurata, B. F. Spencer Jr., and M. Ruiz-Sandoval, "Risk monitoring of buildings using wireless sensor network," in *Proceedings of the International Workshop on Advanced Sensors, Structural Health Monitoring, and Smart Structures*, pp. 10–11, Tokyo, Japan, November 2003.
- [8] F. D'Amato, P. Gamba, and E. Goldoni, "Monitoring heritage buildings and artworks with wireless sensor networks," in *Proceedings of the 3rd IEEE Workshop on Environmental, Energy, and Structural Monitoring Systems (EESMS '12)*, pp. 1–6, Perugia, Italy, September 2012.
- [9] J. Lloret, A. Canovas, S. Sendra, and L. Parra, "A smart communication architecture for ambient assisted living," *IEEE Communications Magazine*, vol. 53, no. 1, pp. 26–33, 2015.
- [10] H. Ghayvat, S. Mukhopadhyay, X. Gui, and N. Suryadevara, "WSN- and IOT-based smart homes and their extension to smart buildings," *Sensors*, vol. 15, no. 5, pp. 10350–10379, 2015.
- [11] S. H. Park, P. J. Lee, K. S. Yang, and K. W. Kim, "Relationships between non-acoustic factors and subjective reactions to floor impact noise in apartment buildings," *Journal of the Acoustical Society of America*, vol. 139, no. 3, pp. 1158–1167, 2016.
- [12] J. Marco Sanjuán, "Estudios del nivel sonoro de diferentes tipos de pólvoras negras para arcabuces y trabucos de salvas," *Revista Especial Día 4 que Fuera de la Junta Central de Fiestas de Villena*, 1996, <http://server-die.alc.upv.es/Alcoy/Tuna/interest.htm>.
- [13] P. J. Bennett, K. Soga, I. Wassell et al., "Wireless sensor networks for underground railway applications: Case studies in Prague and London," *Smart Structures and Systems*, vol. 6, no. 5–6, pp. 619–639, 2010.
- [14] M. Späh, K. Hagberg, O. Bartlomé, L. Weber, P. Leistner, and A. Liebl, "Subjective and objective evaluation of impact noise sources in wooden buildings," *Building Acoustics*, vol. 20, no. 3, pp. 193–213, 2013.
- [15] C.-J. Yu and J. Kang, "Environmental impact of acoustic materials in residential buildings," *Building and Environment*, vol. 44, no. 10, pp. 2166–2175, 2009.
- [16] J. Klos, "Vibro-acoustic response of buildings due to sonic boom exposure: July 2007 field test," Reference Document NASA/TM-2008-215349, 2008, <http://ntrs.nasa.gov/archive/nasa/casi.ntrs.nasa.gov/20080037572.pdf>.
- [17] Sound Level Meter Bruël & Kjaer Type 2250 features, Bruël & Kjaer, <https://www.bksv.com/en/products/sound-and-vibration-meters/sound-level-meters-and-vibration-meters/Type-2250-S>.
- [18] Características del sensor de vibración Type 4374, <http://pdf.directindustry.es/pdf-en/bruel-and-kjaer/transducers-conditioning/17114-692236.html#open>.
- [19] Características del sensor de vibración Bosch BMA056-3 axis accelerometer, https://www.bosch-sensortec.com/bst/products/all_products/bmc056.
- [20] IEC 61672-1:2013-Electroacoustics—Sound level meters—Part 1: Specifications, <https://webstore.iec.ch/publication/5708>.
- [21] IEC 61672-2:2013-Electroacoustics—Sound level meters—Part 2: Pattern evaluation tests, <https://webstore.iec.ch/publication/5709>.

- [22] IEC 61672-3:2013-Electroacoustics—Sound level meters—Part 3: Periodic tests, <https://webstore.iec.ch/publication/5710>.
- [23] C. Harris, *Manual de Medidas Acusticas y Control del Ruido*, S.A. McGraw-Hill/Interamericana De España, 3rd edition, 1995.
- [24] O. Diallo, J. J. P. C. Rodrigues, M. Sene, and J. Lloret, “Distributed database management techniques for wireless sensor networks,” *IEEE Transactions on Parallel and Distributed Systems*, vol. 26, no. 2, pp. 604–620, 2015.
- [25] N. Meghanathan, “A generic algorithm to determine maximum bottleneck node weight-based data gathering trees for wireless sensor networks,” *Network Protocols and Algorithms*, vol. 7, no. 3, pp. 18–51, 2015.

Research Article

Performance Evaluation of Plain Weave and Honeycomb Weave Electrodes for Human ECG Monitoring

Xueliang Xiao,¹ Sandeep Pirbhulal,^{2,3} Ke Dong,¹ Wanqing Wu,² and Xi Mei²

¹School of Textiles and Clothing, Jiangnan University, Wuxi 214122, China

²Shenzhen Institutes of Advanced Technology, Chinese Academy of Sciences, Shenzhen 518055, China

³Shenzhen College of Advanced Technology, University of Chinese Academy of Sciences, Shenzhen 518055, China

Correspondence should be addressed to Xueliang Xiao; xiao_xueliang@163.com and Wanqing Wu; 283077639@qq.com

Received 5 February 2017; Accepted 20 April 2017; Published 5 July 2017

Academic Editor: Young-Jin Cha

Copyright © 2017 Xueliang Xiao et al. This is an open access article distributed under the Creative Commons Attribution License, which permits unrestricted use, distribution, and reproduction in any medium, provided the original work is properly cited.

Long-time monitoring of physiological parameters can scrutinize human health conditions so as to use electrocardiogram (ECG) for diagnosis of some human's chronic cardiovascular diseases. The continuous monitoring requires the wearable electrodes to be breathable, flexible, biocompatible, and skin-affinity friendly. Weave electrodes are innovative materials to supply these potential performances. In this paper, four conductive weave electrodes in plain and honeycomb weave patterns were developed to monitor human ECG signals. A wearable belt platform was developed to mount such electrodes for acquisition of ECG signals using a back-end electronic circuit and a signal transfer unit. The performance of weave ECG electrodes was evaluated in terms of skin-electrode contacting impedance, comfortability, ECG electrical characteristics, and signal fidelity. Such performances were then compared with the values from Ag/AgCl reference electrode. The test results showed that lower skin-electrode impedance, higher R-peak amplitude, and signal-to-noise ratio (SNR) value were obtained with the increased density of conductive filaments in weave and honeycomb weave electrode presented higher comfort but poorer signal quality of ECG. This study inspires an acceptable way of weave electrodes in long- and real-time of human biosignal monitoring.

1. Introduction

In the past decade, many kinds of wearable health monitoring systems have been developed in hospitals and real-life circumstances [1–3]. The wearable sensing hardware platform assists in acquiring and processing of multiple physiological features to provide an early recognition of pathological symptoms and to improve the healing rate of disease without superseding in patient's daily routine [4–6]. Electrocardiogram (ECG) has a noteworthy significance in all biosignals from human body. ECG contains consequential information about the individual heart and performance [7] and is a main investigated element for people with cardiovascular diseases and is a standard process in recent cardiac medical care [8, 9]. To date, a large amount of efforts have been accomplished to formulate the approaches for easy, comfortable, accurate, flexible, and continuous monitoring of ECG signals from human body. The cardiovascular diseases

are the main prevalent and severe life-threatening health issues in the world and the major foundation and reason of death for the people in the ages between 44 and 64 [10, 11].

To date, electrodes using Ag/AgCl are mostly and widely utilized in medical environment for measuring ECG because of Ag/AgCl's low and stable half-cell potential. However, the external layer of human skin has a dry dielectric coat known as "stratum corneum," leading to a transporting diminution from ions to electrons. Therefore, Ag/AgCl electrode cannot be exercised directly; a conductive gel is thus employed to moisturize the skin external layer in order to connect the cardiac microcurrent and the back-end monitoring circuit. Nevertheless, this gel-coating process is relative cumbersome and may bring difficulties in production. Moreover, there is likelihood that there may be gel residues on skin that may cause a short circuit of electrodes. Another drawback of using Ag/AgCl electrode is its short serve time that cannot be used for long-time monitoring of human in

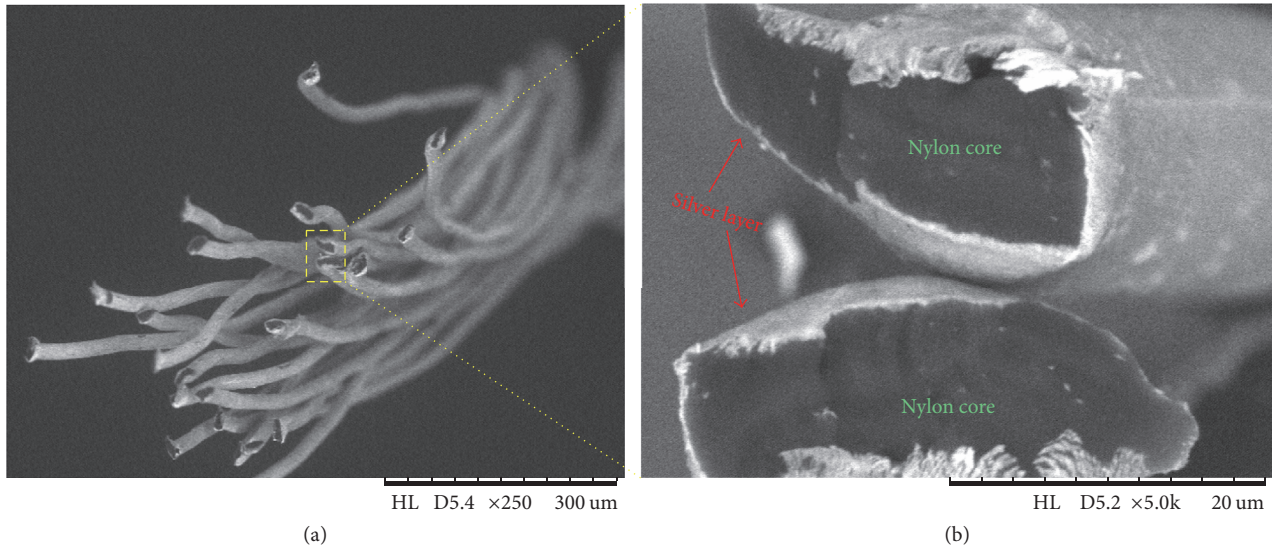


FIGURE 1: Conductive filaments, (a) a bundle of silver-coated nylon filaments used in woven fabric, and (b) an enlarged image of silver-coated layer on filament.

sleeping or working conditions [12, 13]. In addition, Ag/AgCl electrode for ECG measurement process is uncomfortable and painful for patients because the skin preparation for attaching such electrode habitually occupies an abrasion to the external skin layer. The patients who require frequently ECG measurements with skin preparations and gel utilization may also be a reason of infection or allergy. The signal quality of service (QoS) is usually degraded over duration because the skin stratum corneum cells reproduce and the coated conductive gel dries. Furthermore, another disadvantage of such electrodes is not reusable, and the recycling process requires plenty of time and common efforts [14–17].

However, these inherent weaknesses of Ag/AgCl electrode may be overcome with the assistance of textile electrodes because textile structure can assemble different conductive materials within flexible and variable patterns [18–20]. Because of the porous structure, textile electrode can offer better electric conductivity and comfortability without using gel coating. Cho et al. [21] introduced a sputtering conductive alloy on woven fabrics and compared the performance of different types of electrodes from embroidering and weaving processes. It was concluded that the performance of fabric with metal fiber composite (Cu/Ni coated fiber) as a base and embroidered with the wire showed better results in electrical characteristics. A motion sensor was also integrated within the fabric in order to detect the change of skin-electrode impedance accurately. Kannaian et al. [13] proposed an approach of using embroidery stitch on the surface of polyester fabric with 75 D longitudinal density and 150 D horizontal density for electrodes using Wilcom Embroidery software. Such electrodes were compared with commercial Ag/AgCl electrode for the performances in terms of electrode position, cleaning, signal quality, spin supplies, and repeatability. Zieba et al. [22] discussed a textronic knitting method that is integration of biosensors and measurement prototype within knitting patterns. The knitted fabric was used in their work, and the platform

for ECG monitoring was based on three-electrode method. The performance of such functional fabric was compared with different electrodes in ECG monitoring. In the above studies, researchers have devoted to discover more types of conductive and comfortable ECG electrodes. However, the effects of electrode pattern and structure on the electrode conductivity, wearable comfort, and quality of ECG signals have not been studied yet.

This paper introduces four weave-based ECG electrodes with different contents of conductive yarns and weave patterns in ECG acquisition. The weave-based electrodes include plain weave and honeycomb weave with different flexibility, touch feeling, air permeability, and area electrical resistance, respectively. A wearable hardware platform for mounting weave electrodes is used for ECG monitoring. The skin-electrode interference impedance, signal-to-noise ratio (SNR), comfortability from different subjects, and other electrical characteristics of ECG are captured and compared finally, including a comparison between the developed weave electrodes and the reference Ag/AgCl electrodes for the performance in ECG monitoring.

2. Methods and Materials

2.1. Preparation of Weave-Based Electrode. In comparison with knitted fabric, woven fabric is a more stable candidate in biosignal monitoring that is important for reducing motion artifact and obtaining stable signals. In weave patterns, plain weave and honeycomb weave show two typical styles for different comfort parameters, such as air permeability, touch feel, heat, and moisture transfer. Moreover, conductive filaments in the patterns have different bulk resistance evidently even under the same warp and weft densities. Here, we prepared the conductive woven fabrics using silver-coated nylon filaments (70 D, Danier, a unit for fineness). The coated silver layer on each filament has a thickness range of 100–200 nm, as shown in Figure 1. It was measured that the

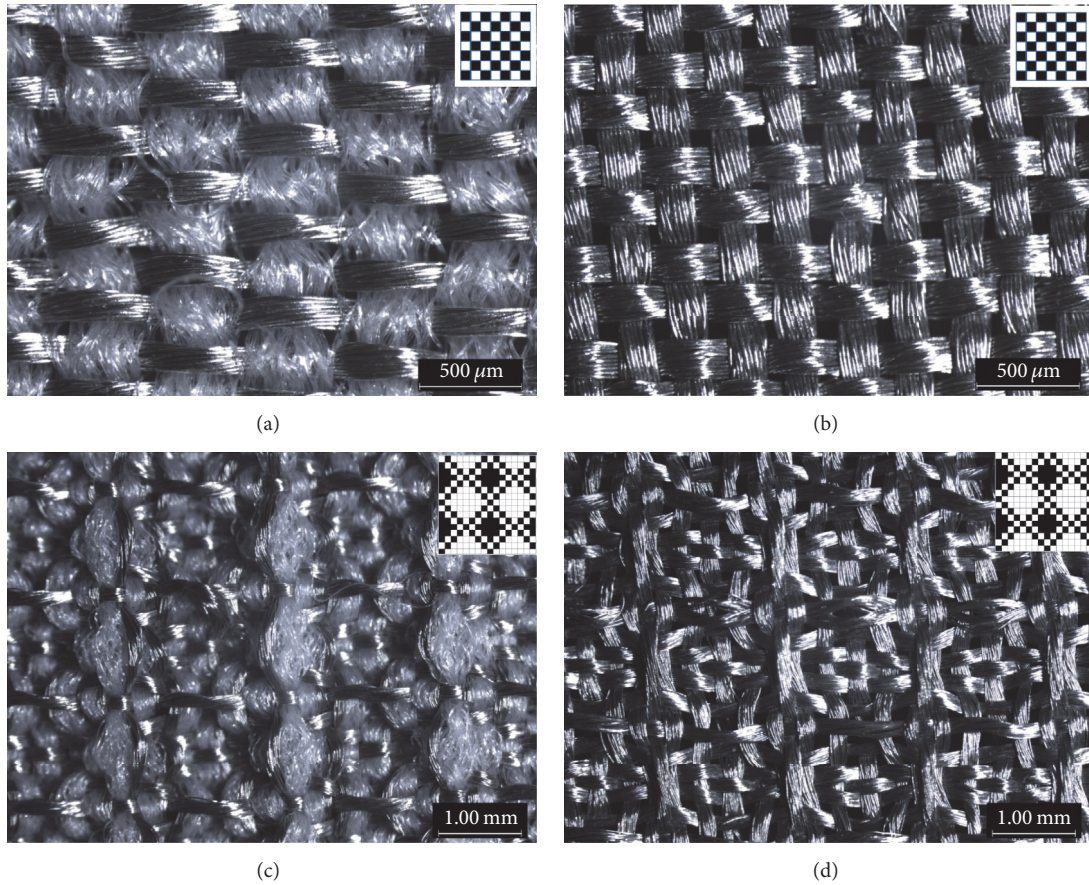


FIGURE 2: Description of four developed weave-based electrodes: (a) plain woven fabric E1 with conductive wefts and nonconductive warps, (b) plain woven fabric E2 with pure conductive yarns, (c) honeycomb woven fabric E3 with conductive wefts and nonconductive warps, and (d) honeycomb woven fabric E4 with pure conductive yarns. The right-top inset figure in each image shows the weave pattern of corresponding fabric.

TABLE 1: Specifications of four developed woven fabrics.

| Fabric | Warp density (yarns/cm) | Weft density (yarns/cm) | Thickness (mm) |
|-----------------------------|-------------------------|-------------------------|----------------|
| Plain woven fabric <i>a</i> | 20 | 64 | 0.45 |
| Plain woven fabric <i>b</i> | 37.35 | 42.71 | 0.32 |
| Honeycomb fabric <i>a</i> | 27.03 | 38.57 | 1.78 |
| Honeycomb fabric <i>b</i> | 30 | 30 | 1.06 |

electrical resistance of each bundle of filaments is 0.02~0.03 Ω /cm. Another kind of yarn used in woven fabric is nonconductive, which is made of blended nylon filaments and cotton fibers (70/30, 70 D).

A rapier woven loom (SL8900S, automatic weave machine) is employed to manufacture four woven fabrics for textile electrodes with the mentioned patterns and materials. These weave electrodes were tailored into identical square size of $45 \times 45 \text{ mm}^2$ to avoid interferences for signal collection, which is referred to the commercial disposable circular electrode (such as 3M electrode) with diameter of 45 mm. Two plain woven fabrics have the same weft yarns that are bundles of silver-coated nylon filaments with twist of 1/cm, as shown in Figures 2(a) and 2(b). The warp yarns of the two plain woven fabrics are different, for example,

conductive and nonconductive, which endow the two fabrics with different area resistances. The honeycomb woven fabrics show similar situations with plain woven fabrics. The specifications of the four fabrics are listed in Table 1.

The fabric morphologies were characterized using a Leica M165C microscope; the fabric thickness was measured by a standard tester (6 g/inch² pressure). Figure 2 shows the SEM images of as-made woven electrodes. Plain woven fabrics show relatively flat surface with regular pores at the interlaced points of four neighbor warp and weft yarns. The size of pores or fabric porosity decides the fabric permeability and wearable comfortability. Honeycomb woven fabric shows slightly a periodicity and forming repeats of inverted pyramidal space on the both surfaces of fabric. In a honeycomb fabric as shown in Figure 2(c), the part of a warp yarn underneath

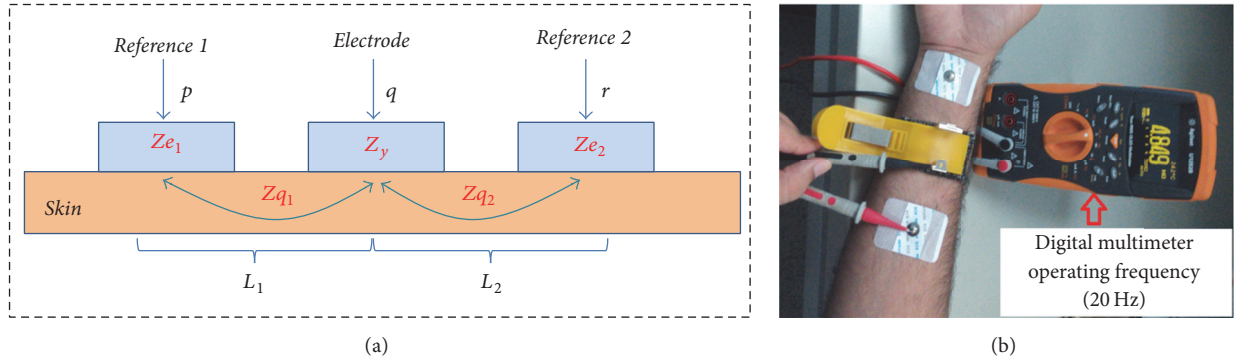


FIGURE 3: Measurement of skin-electrode impedance, (a) block diagram, and (b) real setup for measurement of electrochemical impedance.

a weft float is a warp float. Two layers of floats form a closed internal space. Owing to the periodical repeats of the inverted pyramidal space and the closed internal space, the fabric has been reported with good sound and moisture absorption, good insulating, and quick dry rate [23, 24]. The as-made honeycomb woven fabrics show different electric resistance due to different contents of conductive filaments and connection of fabric surface to human skin.

2.2. Skin-Electrode Impedance Measurement. Impedance measurement is the most important step for evaluating the performance of weave-based electrodes in acquisition of biosignals from human body. To compare the conductivity of different weave-based electrodes, a digital multimeter was used to measure the skin-electrode impedance. A commercial Ag/AgCl ECG electrode (made in 3M Group) was used as a reference electrode [10]. A skin-electrode model using equivalent circuit is shown in Figure 3. The skin-electrode impedance can be calculated as

$$\begin{aligned} Z_{pq} &= Z_{q1} + Z_{e1} + Z_y, \\ Z_{qr} &= Z_{q2} + Z_{e2} + Z_y, \\ Z_{pr} &= Z_{q1} + Z_{q2} + (Z_{e1} + Z_{e2}), \end{aligned} \quad (1)$$

where Z_{q1} and Z_{q2} denote the body impedance between a reference and an unknown electrode at the points “ p, q ” and “ q, r ,” respectively. Z_{e1} and Z_{e2} stand for the interface impedance between the skin and reference electrode at the points of q and r respectively. Z_y is the interface impedance between skin and unknown electrode. Z_{pq} , Z_{qr} , and Z_{pr} are the impedance between each electrode. The proposed weave electrode, in this case, is the unknown electrode. Z_y is located at the center between the two reference electrodes; suppose that $L_1 = L_2$ [7]. Since the same reference electrode was used, it is assumed that

$$\begin{aligned} Z_{e1} &= Z_{e2}, \\ Z_{q1} &= Z_{q2}, \end{aligned} \quad (2)$$

$$Z_y = Z_{pq} - \frac{Z_{pr}}{2}, \quad (3)$$

$$Z_y = Z_{qr} - \frac{Z_{pr}}{2}. \quad (4)$$

Under frequency of 20 Hz, the digital multimeter was utilized to evaluate the impedance between the test points “ p ” and “ q ,” “ q ” and “ r ,” and “ p ” and “ r ,” respectively. The electrode impedance Z_y was calculated using (3) or (4). During the measurement of impedance of a weave electrode, it should be pointed out that the impedance tends to decrease due to the increased contacting area of electrode and human skin that is caused by compression of conductive yarns to skin under a certain pressure. Herein, an elastic Velcro was utilized to offer a stable pressure up to 1000 N/m².

2.3. Establishment of Wearable System for ECG Signal Acquisition. In order to compare the ECG signals acquired through the developed weave electrodes fairly, a dedicated wearable system for recording biopotentials has been designed and established, as shown in Figures 4 and 5. The system consists of three components, namely, sensor (mainly electrodes), integrated hardware platform, and display terminal, as shown in block diagram of Figure 4. Among the three parts, the main body is the integrated wearable hardware platform that contains a HKD-10A module, signal filter, analog-digital conversion, and a wireless communication module. The whole platform is constructed through a filtering and amplification circuit. To reduce the obtained signal noises, such as the noises from baseline drift or 50 Hz of power interference, a developed recording unit is designed specifically and manufactured for ECG monitoring using a HKD-10A monolithic analog front-end with high gain and 1-T Ω input impedance. Owing to the limitation of power consumption, a MSP430F149 module is adopted as a data processor. A HKD-10A sensor was designed to collect ECG signals from microcontroller when an enabling signal was sent from a chip microcontroller through a UART port. The port can be used to stream data into a PC through a Bluetooth communication protocol or an oscilloscope through a connecting probe. The energy for operating the whole system is supplied by a rechargeable Li-ion battery (3.3 V) or a rechargeable USB terminal [25].

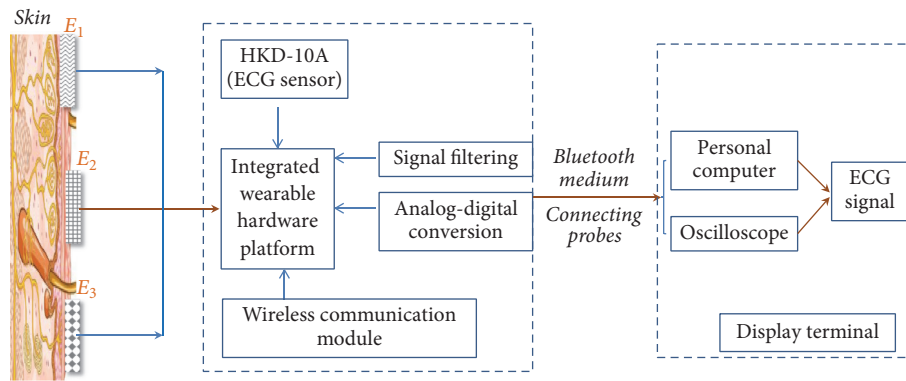


FIGURE 4: A block diagram for wearable hardware platform implementation for obtaining ECG from skin to display terminal.

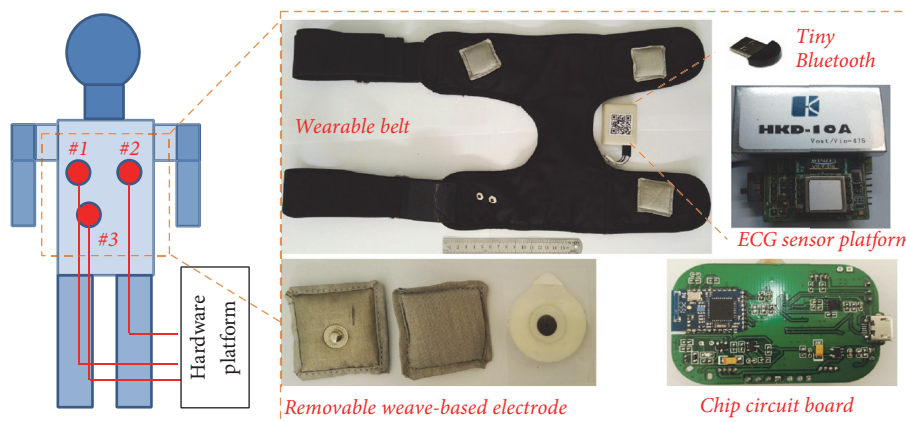


FIGURE 5: Three points for human-hardware platform interaction for ECG measurement and the real wearable experiment setup using belt format and components mounted on the hardware platform.

Noise is the biggest trouble in obtaining clear and stable ECG signals. The noise is generated mainly due to the power line interference, electrode contact noise, baseline drift, instrumentation noise, motion artifacts, electrosurgical noise, and other less significant noise sources. Generally, a hardware filter can eliminate unwanted noise. The filter restricts those noise frequencies where noise occurred, remaining the useful frequencies of ECG signals. The major restriction of hardware filter depends on capacitors that cannot be proscribed well both in construction and in normal utilization [26–29].

Apart from the hardware platform, we also developed software that helps to monitor ECG. Owing to the scrawny shape of ECG signals that can be easily corrupted by various kinds of noises that cannot be filtered completely by the hardware filter, a software filter is dependent on the cut-off frequencies that can be controlled precisely by allowing implementation of advanced filter models. Particularly, ECG amplitude is extremely small, approximately at 1 mV. Thus, it is essential to exercise filter to eliminate an extensive range of noises. Therefore, at the software end, a digital notch filter at 60-Hz for minimizing the power line interference, a finite impulse response band-pass filter for correcting

baseline wander, a multiscale mathematical morphology filter for eliminating motion artifacts and power line interference, and a differential operation method for smoothing and normalizing have been integrated into this developed platform. The ECG signals were recorded under a speed of 25 mm/s. Moreover, the wearable platform is in the format of wearable belt, as shown in Figure 5, where four points are available to mount the removable weave-based electrodes. The developed conductive woven fabrics are tailored into pillow-block shape ($4 \times 4 \text{ cm}^2$) of electrodes that filled with a very thin layer of sponge. The removable electrodes connect with the hardware platform through metal buttons.

2.4. Weave-Based Electrode for ECG Monitoring. The ECG monitoring of a human was carried out using a standard Holter with a single lead, as shown in the three-point interaction of diagram in Figure 5. The obtained lead is approximately oriented along the cardiac axis. This method is a way to produce high quality of ECG because the typical orientation of the cardiac axis is well-known in clinical option. Additionally, this method of standard placement has an intrinsic advantage in conveying useful information for inspection. In this study, Ag/AgCl electrode was used as a

TABLE 2: Fundamental base for performance evaluation of developed weave electrodes for ECG monitoring.

| Particulars | Basis of evaluation | | |
|----------------------------|---------------------|------------|-----------|
| | 2 points | 1 point | 0 points |
| QRS-complex | Found | — | Not found |
| P-wave | Found | — | Not found |
| T-wave | Found | — | Not found |
| R wave amp | >0.35 V | 0.3–0.35 V | <0.3 V |
| Stabilization time | ≤10 s | 10 s–60 s | >60 s |
| R-peak amplitude variation | <0.05 V | 0.05–0.1 V | >0.1 V |

TABLE 3: Weighting coefficients for result analysis.

| Particulars | QRS-complex | P-wave | T-wave | R wave amp | Stabilization time | R-peak amp variation |
|--------------------|-------------|--------|--------|------------|--------------------|----------------------|
| Weight coefficient | 20% | 20% | 20% | 20% | 10% | 10% |

ground reference for measuring impedance. Weave-based electrodes and standard Ag/AgCl electrodes were placed side by side for simultaneous recording the biosignals.

Here in detail, two electrodes were positioned on the chest surface (#1 and #2) near to heart, while a third reference electrode (#3) was placed on the lower left position that is 10 cm away from electrode #1. This arrangement enables producing relatively neat and clean ECG signals with higher R-peak amplitude and QRS-complex waves. For a specific weave-based electrode, its one fabric side was attached to human skin, while the other side was connected to the developed wearable belt through the metal buttons. The acquired signals can be visualized and stored to a specific base station.

2.5. Evaluation of Electrode's Comfortability. The comfort level is a very important factor for patient to accept the attached electrodes for long-time biosignal monitoring. Different types of electrodes have distinguished levels of comfort, because it varies from structures, densities, and materials. There are several subjective comfort performance indexes, for example, thermal comfort, tactile comfort, style comfort, and pressure comfort. To monitor the human ECG, the tactile (touch feeling) comfort is a very useful parameter because the wearable platform requires long time to monitor. The tactile comfort depends on the microstructure, fabric density, and fiber properties of weave-based electrodes. The tactile comfort can be measured on the basis of comfortable feeling to skin-electrode contact. The discomfort is mainly due to tickle, itch, prickle, scratchiness, fiber shedding, and all other factors that could irritate the patients during the long-time ECG monitoring. This study involves four developed weave-based electrodes; each one has a unique comfortability. For testing the comfort level of each electrode, the electrode was attached on the wrist of participant for friction experiment. After the process, each participant was asked about the feeling and comfort level; this subjective feeling was recorded with average value by the informed written consent that was provided to all participants before undergoing the ECG monitoring using the developed electrodes. The other objective parameters of comfort levels, such as thermal conductivity and air permeability, to some extent can tell

us the comfortability of developed weave-based electrodes. Here, air resistance and thermal conductivity were measured five times for average values. The instruments are KES-F Thermo Labo II for measuring the thermal conductivity and KES-F8-API air permeability tester for measuring the air resistance of electrodes.

2.6. Process of Human ECG Monitoring. Ten right-handed volunteers without history of cardiovascular diseases were employed for our ECG monitoring experiments. Each subject was tested under the standard conditions between 4:00 pm and 10:00 pm at temperatures of 21–26°C after refraining from smoking and coffee utilization for six hours before his/her contribution to the experiment. The investigated properties of ECGs and basis of evaluation can be viewed in Table 2. Many factors influence the evaluation of electrode functional quality. Therefore, an evaluation method was developed to compare different weave-based electrodes with different weighting coefficients.

In a repeat of ECG, QRS-complex, P-wave, and T-wave are the main parts that can describe the action of heart. In the evaluation of electrode's quality, if these wave parts were clearly visible, then 2 points were given for the electrode quality; otherwise 0 points were given for the electrode quality without clear waves. The stabilization time was measured from 0 sec until the baseline settled to the level of 1.6 V. If the stabilization time was shorter than 10 seconds, 2 points were then given for the evaluation of electrode quality; however, if the stabilization time was in the range of 11 to 60 seconds, 1 point was given for related electrode quality; otherwise, 0 point was given for related electrode quality. The R-peak amplitude means the signal strength. If it is over 0.35 V, then it will obtain 2 points; if it is under 0.01 V, then it will obtain 0 points. The R-spike amplitude variation means the difference (V) between the lowest and highest peaks. If amplitude variation is under 0.05 V, then it gives 2 points and if it is over 0.1 V, then it will obtain 0 points. The basis of evaluation standard is listed in Table 2.

As shown in Table 3, weighting coefficients were used that depends on the importance of the electrode property in the long-time ECG monitoring and analysis. Here, the most important properties (weighting coefficient) in the

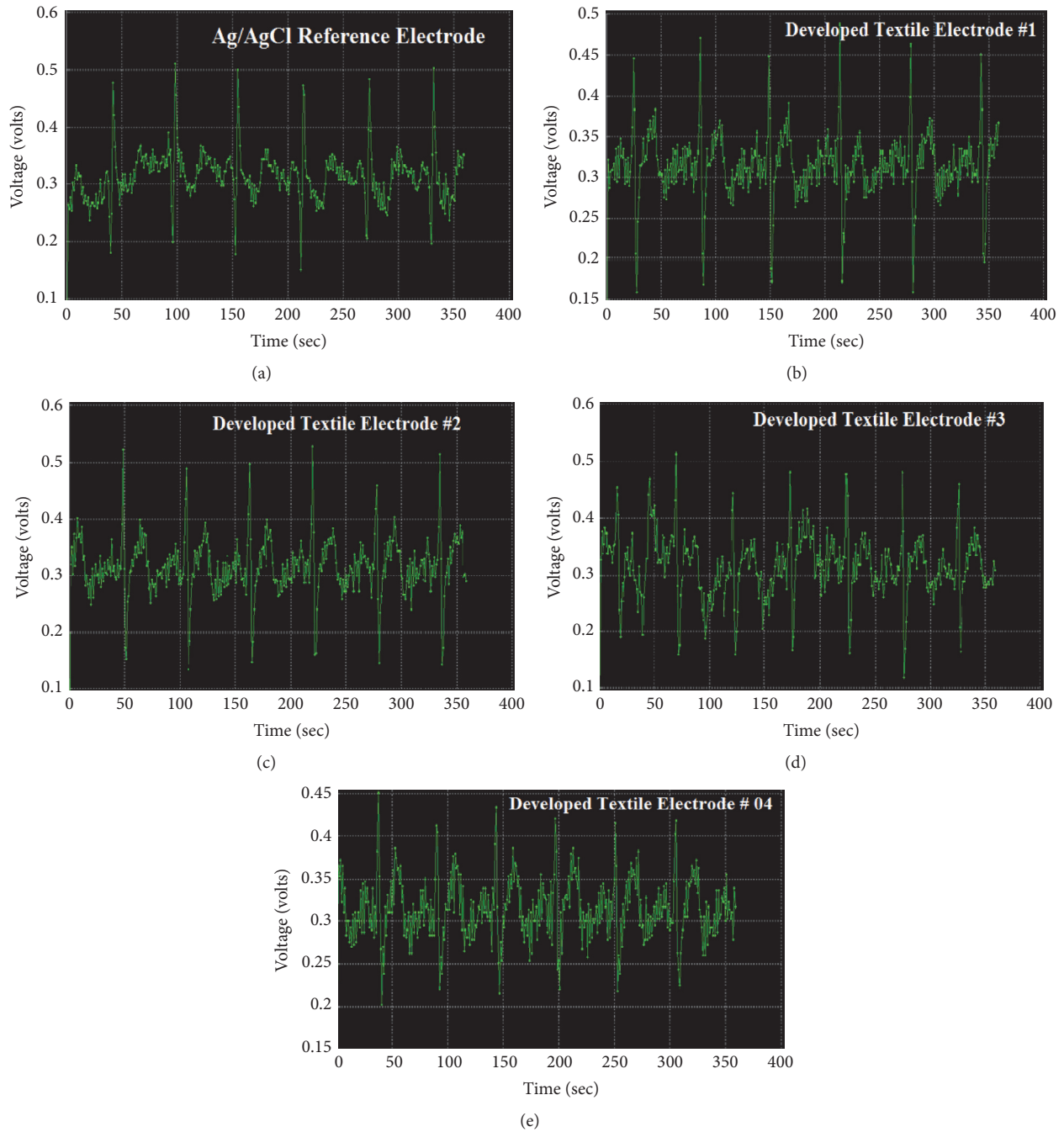


FIGURE 6: Real-time ECG signals obtained from different electrodes: (a) Ag/AgCl reference electrode; (b) plain woven fabric E1; (c) plain woven fabric E2; (d) honeycomb woven fabric E3; (e) honeycomb woven fabric E4.

evaluation are QRS-complex, P-wave, T-wave, noise, and 50 Hz interference. These properties are important because they affect the diagnosis of cardiovascular diseases mostly through ECG signals.

3. Results and Discussion

3.1. ECG Signals from Weave-Based Electrodes. Figure 6 shows five screenshots of ECG signal monitoring for the

same person using five different electrodes that mounted on the developed ECG system. Compared with the quality of ECG signals, it can be judged easily that honeycomb woven fabrics give poorer ECG signals than the signals from plain weaves because some large voltage ranges of P and T waves appeared through honeycomb electrodes. This may be due to the different skin-electrode interface impedance of electrode to skin. For plain weave electrode, fabric made of pure conductive filaments shows better signal quality in

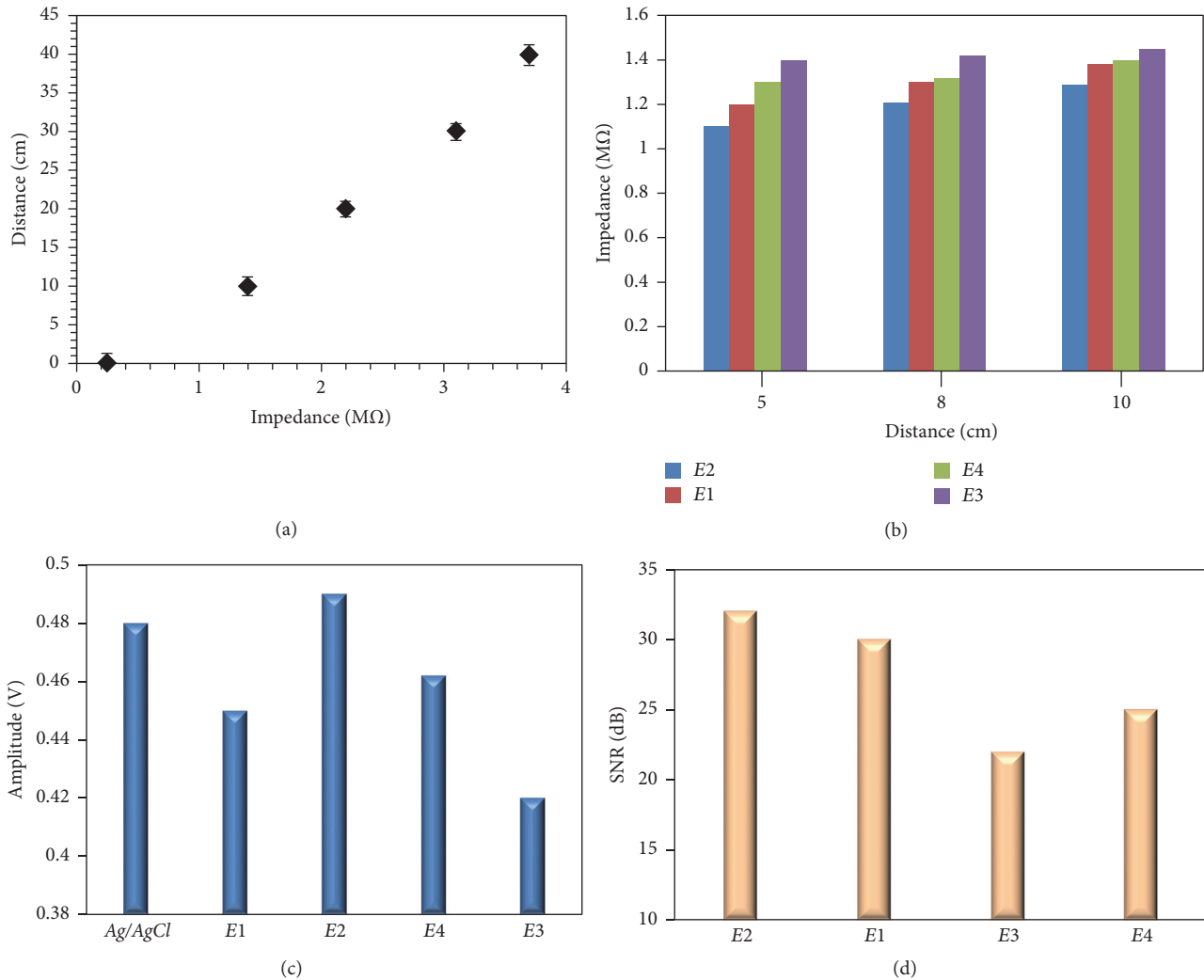


FIGURE 7: Experimental results: (a) effect of distance between two reference electrodes for measuring skin-electrode interference impedance, (b) skin-electrode impedance comparisons between developed electrodes, (c) R-peak amplitude comparisons between weave-based electrodes, (d) signal-to-noise ratio (SNR) comparisons between different weave-based electrodes.

ECG acquisition than the fabric interwoven by conductive weft and nonconductive warp filaments. This can be viewed from the amounts of noises and clarity of P-wave and T-wave in the real ECG signals. However, in comparison with the signal quality from Ag/AgCl electrode, especially to compare the P-wave characteristic peak between Figures 6(a) and 6(c), plain weave electrode still shows slightly lower level in signal collection; even the collected ECG does not affect the diagnosis of patient's cardiovascular diseases.

Based on Figure 6, the acceptance of developed weave-based electrodes was compared according to six parameters and listed in Table 4. From the final scores, it is noted that only electrode E2 has the same value with the reference Ag/AgCl electrode, indicating that E2 can replace the commercialized electrodes from the viewpoint of ECG monitoring. Other developed weave-based electrodes, more or less, have some weakness in monitoring biosignals. The following sections will discuss about the detailed information of developed electrodes in specific performances.

3.2. Difference of Skin-Electrode Impedance among Electrodes. Obviously, textile electrodes can be used for long-term monitoring of biosignals because the electrodes do not annoy human skin; additionally, they are washable, lightweight, and ductile. However, a key disadvantage of such electrode is its large electrode-skin interference impedance. Normally, textile electrodes have impedance values with human skin in the range of 1–5 MΩ/cm² while the Ag/AgCl electrode shows much less impedance up to 10 kΩ/cm². As shown in the experiment setup in Figure 3, the distance between each weave-based electrode and reference electrode can be changeable. The relationship between the distance and the measured related impedance can be plotted in a linear increase tendency, as shown in the tested data in Figure 7(a). This indicates that the human skin is an isotropic resistance when assuming the interface resistance of skin-electrode constant. A comparison for skin-electrode impedance is gathered up between the developed weave electrodes as shown in Figure 7(b). An increase relationship of the impedance

TABLE 4: ECG monitoring and performance analysis comparisons between Ag/AgCl reference electrode and developed weave electrodes.

| Particulars | Ag/AgCl reference electrode | | Plain weave electrode E1 | | Plain weave electrode E2 | | Honeycomb weave electrode E3 | | Honeycomb weave electrode E4 | |
|----------------------------|-----------------------------|------|--------------------------|------|--------------------------|------|------------------------------|------|------------------------------|------|
| | Actual | Rate | Actual | Rate | Actual | Rate | Actual | Rate | Actual | Rate |
| QRS-complex | Found | 2 | Found | 2 | Found | 2 | Found | 2 | Found | 2 |
| P-wave | Found | 2 | Found | 2 | Found | 2 | Found | 2 | Found | 1 |
| T-wave | Found | 2 | Found | 2 | Found | 2 | Found | 1 | Found | 2 |
| R wave amp | 0.494 v | 2 | 0.46 v | 2 | 0.504 v | 2 | 0.477 v | 2 | 0.432 v | 2 |
| Stabilization time | 10 s | 2 | 10 s | 2 | 10 s | 2 | 10 s | 2 | 10 s | 2 |
| R-peak amplitude variation | 0.005–0.02 | 2 | 0.01–0.04 | 1 | 0.005–0.035 | 2 | 0.015–0.07 | 0 | 0.015–0.04 | 1 |
| Score | | 12 | | 11 | | 12 | | 9 | | 10 |

TABLE 5: R-peak amplitude comparisons between Ag/AgCl reference and developed weave-based electrodes.

| Number | Ag/AgCl reference commercial electrode | R-peak amplitude (V) | | | |
|--------|---|--------------------------------|--------------------------------|------------------------------------|------------------------------------|
| | | Plain weave electrode E1 | Plain weave electrode E2 | Honeycomb weave electrode E4 | Honeycomb weave electrode E3 |
| 1 | 0.485 | 0.450 | 0.520 | 0.510 | 0.460 |
| 2 | 0.510 | 0.470 | 0.490 | 0.440 | 0.420 |
| 3 | 0.500 | 0.450 | 0.495 | 0.480 | 0.445 |
| 4 | 0.480 | 0.485 | 0.520 | 0.480 | 0.430 |
| 5 | 0.485 | 0.460 | 0.480 | 0.485 | 0.420 |
| 6 | 0.505 | 0.450 | 0.520 | 0.470 | 0.420 |

with the distance for each kind of weave-based electrode is still viewed. Under one distance, it is clearly found that plain weave electrode shows less impedance than honeycomb electrode under the same size of electrode. This is due to the honeycomb feature with large amounts of repeats of microconcave pits on the fabric surface that cannot contact human skin completely.

Under the same fabric pattern, the application of non-conductive yarns into fabric would increase the impedance significantly; for example, E2 (with nonconductive filaments) has very low resistance in weft direction while it is almost insulated in warp direction. In experiment, the impedance has been measured under different distance values, for example, 5 cm, 8 cm, and 10 cm. Consistent with Figure 7(b), the test results in detail showed that plain woven fabric (E2) made of pure conductive filaments, fabric (E1) made of blended conductive filaments, honeycomb fabrics (E4) made of pure conductive filaments, and honeycomb fabric (E3) made of blended conductive filaments have skin-electrode impedance of 1.107, 1.227, and 1.269 MΩs, 1.195, 1.299, and 1.349 MΩs, 1.315, 1.325, and 1.419 MΩs, and 1.407, 1.440, and 1.454 MΩs at distance of 5 cm, 8 cm, and 10 cm, respectively. The values indicate that the introduction of nonconductive filaments into electrode may increase the wearable electrode comfortability; however, it may not be conducive to reduce the impedance in biosignal monitoring.

3.3. ECG Electrical Characteristic Comparisons. The electrical performance of weave-based electrode in ECG monitoring is evaluated and recorded, as the R-peak amplitude values tested for six times shown in Table 5. The average values of the amplitude are compared in the histogram of Figure 7(c). The R-peak amplitude values were obtained under the same test conditions including the same hardware and subject. Thus, it is noted that plain weave electrode E2 shows the highest amplitude, indicating that pure conductive fabric with tight attachment to human skin can effectively decrease the skin-electrode impedance and improve the whole circuit in signal peak amplitude, which means that such electrode can acquire even weaker biosignals or more sensitive to weak surface potential accumulated from heart or muscle. Due to the concave structure of each unit cell of honeycomb woven fabric, the fabric attaching to human

skin is not as tight as plain woven fabric, which means that the effective contacting area of skin and electrode is reduced and the R-peak amplitude is manifested to decrease either. Similarly, introduction of common textile fibers into conductive fabric, although this would increase the fabric wearable comfortability, can decrease the sensitivity of fabric electrode in ECG monitoring; here, the observed peak amplitude is thereafter decreased. This is consistent with the test data and comparisons of developed weave-based electrodes in skin-electrode impedance.

Moreover, the stabilization time for ECG signals is set to be 10 s for all compared electrodes. In Table 4, a variable, namely, R-peak amplitude variation is used to estimate the biosignal stability in all cases. Consistently, a variation in R-peak amplitudes for each electrode is noted that the electrodes E1, E2, E3, and E4 show that R-peak variation is in 0.01–0.04, 0.005–0.035, 0.015–0.04, and 0.015–0.07, respectively. This means the monitored signals are smoother to present in ECG when the resistance of electrode is less, and higher conductive electrode would lead to higher quality of ECG signals.

3.4. Comparison for Signal-to-Noise Ratio (SNR). SNR of ECG is determined by the root mean square (RMS) of the isoelectric region. For ECG, the SNR is the ratio of useful signal power (P_{signal}) to noise power (P_{noise}), as expressed in

$$\text{SNR} = \log \frac{P_{\text{signal}}}{P_{\text{noise}}} = \log \frac{(A_{\text{signal}})^2}{(A_{\text{noise}})^2}, \quad (5)$$

where “SNR” denotes the signal-to-noise ratio and “A” represents the mean square root of amplitude. Because of using different filters, the signal of power frequency with the range of 49.5 Hz to 50.5 Hz was removed. Thus, the SNR of ECG signal for each electrode was determined. The comparison of SNR values between developed weave-based electrodes is illustrated in Figure 7(d) and Table 6. The measured SNR values for electrodes E3 and E4 are lower than the values from electrodes E1 and E2, among which E2 shows the highest SNR value, that is, 33.86 dB. This means that the plain weave with conductive warp and weft yarns has better signal clarity or less noise under the same monitoring environment and conditions. This is consistent with the monitored signals

TABLE 6: Signal-to-noise ratio (SNR) comparison between developed weave-based electrodes.

| Electrode type | Measurement | Value 1 | Value 2 | Average value | SNR (dB) |
|--------------------------|-------------|---------|---------|---------------|----------|
| Plain W-electrode E2 | Signal | 0.203 | 0.389 | 0.296 | 33.86 |
| | Noise | 0.003 | 0.009 | 0.006 | |
| Plain W-electrode E1 | Signal | 0.189 | 0.413 | 0.301 | 33.61 |
| | Noise | 0.007 | 0.010 | 0.0065 | |
| Honeycomb W-electrode E3 | Signal | 0.268 | 0.320 | 0.284 | 25.54 |
| | Noise | 0.013 | 0.017 | 0.015 | |
| Honeycomb W-electrode E4 | Signal | 0.320 | 0.253 | 0.286 | 28.29 |
| | Noise | 0.009 | 0.013 | 0.011 | |

TABLE 7: Comparison of comfort level between four weave electrodes.

| Electrode number | Tactile comfort (?/10) | Air resistance (KPa·s/m) | Thermal conductivity (W/m·K) |
|------------------|---------------------------|-----------------------------|---------------------------------|
| E1 | 7.5/10 | 0.82 | 0.058 |
| E2 | 7/10 | 0.68 | 0.065 |
| E3 | 8.5/10 | 0.18 | 0.018 |
| E4 | 8/10 | 0.12 | 0.024 |

from ECG in Figure 6. Assuming the hardware, software system and test conditions are constant during all ECG monitoring; high quality of ECG means good connection of skin and electrode. More connection area of skin and electrodes would lead to high SNR value because more biopotential/charges are collected through the connection area. For such case, electrode E2 has more effective and larger amounts of conductive filaments in touching human skin. In comparison, honeycomb woven fabrics display more noises during ECG monitoring because of less effective conductive filaments attaching to skin and easier deformation of such fabric structure that causes the effective connection area may be always changeable slightly. This is manifested through the frequently appeared noises at the P-wave and T-wave positions.

3.5. Comparison of Weave Electrodes on Comfort Level. The comfort level of developed weave-based electrodes attached on human skin is a very important parameter, which decides the acceptance of patients to the developed weave electrodes. This parameter also determines whether the developed electrode is comfortable enough to be used for long-term physiological signal monitoring. As to our developed four weave ECG electrodes, they were woven with different patterns, material components, fabric density, microstructure, and fiber properties; thus the four weave electrodes have different tactile comfort levels. In this study, ten volunteers were employed to evaluate the tactile comfort of attached electrodes. Their scores are listed in Table 7, which showed that honeycomb woven fabric has better tactile comfort, especially when honeycomb uses common textile fibers that have already proved to be biocompatible to human skin.

Air resistance means the ease of air and moisture to transfer through the fabric electrode. A higher value of such factor indicates a more difficult of air and moisture to transfer. The tested values show that honeycomb woven

fabric has better ability of air and moisture to transfer in comparison with plain weave electrodes. The thermal conductivity shows the heat transfer ability of fabric; this factor is useful when the wearer is in the extreme conditions. The tested values of such factors indicate that the warmth retention of honeycomb weave is better than plain weave because the concave surface of honeycomb could store still air inside for less heat convection. In a word, honeycomb weave electrode seems a better candidate for ECG signal monitoring because of its comfortable wear from subjective and objective views. However, from the viewpoints of skin-electrode impedance, electrical characteristic, and SNR value, conductive plain weave indicates a better candidate for ECG signal monitoring. This discovery may inspire new design of textile electrode for human biosignal long-term monitoring, so as to combine the structures of plain woven and honeycomb woven characteristics.

4. Conclusions

Textile electrode becomes popular in current booming developed wearable electronics for its flexible, breathable, biocompatible, and conductive properties that can be used for long-time monitoring of some human chronic cardiovascular diseases. Weave electrode has relative stable structure that is usually encountered in some new wearable electronics. Here, four woven conductive fabrics were developed in two patterns and pure/blended conductive components to study their feasibility in real-time ECG monitoring.

Apart from preparation of weave-based electrodes, we also established a hardware-based platform for acquiring signals where all system and test conditions were assumed constant during the whole monitoring process. Skin-electrode impedance, electrical characteristic, signal-to-noise ratio, and comfort level are key factors to evaluate the feasibility of developed weave-based electrode in biosignals collection.

Experimental data indicated that more content of conductive filaments and larger connection area of conductive fabric part to human skin would lead to lower skin-electrode impedance, larger R-peak amplitude, larger value of signal-to-noise ratio, but poorer comfortability. There is a necessity to find out a balance point between higher quality of ECG acquisition and wearable comfortability. There may be an intermediate pattern between plain weave and honeycomb weave that both can obtain good ECG signals and also can give the wearer good feeling of skin attaching in dressing. In near future, we are looking forward to these developed weave electrodes in long-time biosignal monitoring for chronic diseases. A long-term training is also required for patients with diseases such as obstructive sleep apnea, hypertension, negative emotion management, and stress in order management for their proper monitoring.

Disclosure

Xueliang Xiao and Sandeep Pirbhulal are co-first authors.

Conflicts of Interest

The authors declare no competing financial interests.

Authors' Contributions

The authors Sandeep Pirbhulal and Xueliang Xiao contributed equally.

Acknowledgments

This work was financially supported by the *National Undergraduate Innovation Training Program* (Grant no. 201610295020), *Natural Science Foundation of Jiangsu Province* (Grant no. BK20160157), *Research Fund for Industry-University Cooperation of Jiangsu Province* (Grant no. BY2016022-07), and *Guangzhou Science and Technology Planning Project* (Grant no. 2016A030310129).

References

- [1] A. Rangarajan, "Emerging trends in healthcare adoption of wireless body area networks," *Biomedical Instrumentation and Technology*, vol. 50, no. 4, pp. 264–276, 2016.
- [2] S. Pirbhulal, H. Zhang, S. C. Mukhopadhyay et al., "An efficient biometric-based algorithm using heart rate variability for securing body sensor networks," *Sensors*, vol. 15, no. 7, pp. 15067–15089, 2015.
- [3] P. Chahuaara, A. Fleury, F. Portet, and M. Vacher, "On-line human activity recognition from audio and home automation sensors: comparison of sequential and non-sequential models in realistic Smart Homes," *Journal of Ambient Intelligence and Smart Environments*, vol. 8, no. 4, pp. 399–422, 2016.
- [4] R. Pan, D. Chua, J. S. Pathmasuntharam, and Y. P. Xu, "An opportunistic relay protocol with dynamic scheduling in wireless body area sensor network," *IEEE Sensors Journal*, vol. 15, no. 7, pp. 3743–3750, 2015.
- [5] G. Valenza, L. Citi, C. Gentili, A. Lanatá, E. P. Scilingo, and R. Barbieri, "Characterization of depressive states in bipolar patients using wearable textile technology and instantaneous heart rate variability assessment," *IEEE Journal of Biomedical and Health Informatics*, vol. 19, no. 1, pp. 263–274, 2015.
- [6] Q. Ni, A. B. G. Hernando, and I. P. de la Cruz, "The elderly's independent living in smart homes: a characterization of activities and sensing infrastructure survey to facilitate services development," *Sensors*, vol. 15, no. 5, pp. 11312–11362, 2015.
- [7] B. Taji, S. Shirmohammadi, V. Groza, and I. Batkin, "Impact of skin-electrode interface on electrocardiogram measurements using conductive textile electrodes," *IEEE Transactions on Instrumentation and Measurement*, vol. 63, no. 6, pp. 1412–1422, 2014.
- [8] B.-S. Lin, A. M. Wong, and K. C. Tseng, "Community-based ecg monitoring system for patients with cardiovascular diseases," *Journal of Medical Systems*, vol. 40, no. 4, article no. 80, pp. 1–12, 2016.
- [9] L. Loreto, T. Andrea, D. Lucia, L. Carla, P. Cristina, and R. Silvio, "Accuracy of EASI 12-lead ECGs in monitoring ST-segment and J-point by nurses in the Coronary Care Units," *Journal of Clinical Nursing*, vol. 25, no. 9–10, pp. 1282–1291, 2016.
- [10] F. Miao, Y. Cheng, Y. He, Q. He, and Y. Li, "A wearable context-aware ECG monitoring system integrated with built-in kinematic sensors of the smartphone," *Sensors*, vol. 15, no. 5, pp. 11465–11484, 2015.
- [11] S. Song, M. Rooijackers, P. Harpe et al., "A low-voltage chopper-stabilized amplifier for fetal ECG monitoring with a 1.41 power efficiency factor," *IEEE Transactions on Biomedical Circuits and Systems*, vol. 9, no. 2, pp. 237–247, 2015.
- [12] A. Karilainen, S. Hansen, and J. Muller, "Dry and capacitive electrodes for long-term ECG-monitoring," in *Proceedings of 8th Annual Workshop on Semiconductor Advances*, vol. 2005, p. 156.
- [13] T. Kannaian, R. Neelaveni, and G. Thilagavathi, "Design and development of embroidered textile electrodes for continuous measurement of electrocardiogram signals," *Journal of Industrial Textiles*, vol. 42, no. 3, pp. 303–318, 2013.
- [14] F. Sun, Z. Zhao, Z. Fang, L. Du, and D. Chen, "Design and implementation of a high integrated noncontact ECG monitoring belt," *Journal of Fiber Bioengineering and Informatics*, vol. 8, no. 1, pp. 37–46, 2015.
- [15] H. Li, X. Chen, L. Cao et al., "Textile-based ECG acquisition system with capacitively coupled electrodes," *Transactions of the Institute of Measurement and Control*, vol. 39, no. 2, pp. 141–148, 2017.
- [16] D. Pani, A. Dessi, J. F. Saenz-Cogollo, G. Barabino, B. Fraboni, and A. Bonfiglio, "Fully textile, PEDOT: PSS based electrodes for wearable ECG monitoring systems," *IEEE Transactions on Biomedical Engineering*, vol. 63, no. 3, pp. 540–549, 2016.
- [17] G. Buchberger, R. A. Barb, J. Schoeftner et al., "Transparent, flexible, thin sensor surfaces for passive light-point localization based on two functional polymers," *Sensors and Actuators, A: Physical*, vol. 239, pp. 70–78, 2016.
- [18] M. Vega-Barbas, I. Pau, J. Ferreira, E. Lebis, and F. Seoane, "Utilizing smart textiles-enabled sensorized toy and playful interactions for assessment of psychomotor development on children," *Journal of Sensors*, vol. 2015, Article ID 898047, 9 pages, 2015.
- [19] G. M. Paul, F. Cao, R. Torah, K. Yang, S. Beeby, and J. Tudor, "A smart textile based facial emg and eog computer interface," *IEEE Sensors Journal*, vol. 14, no. 2, pp. 393–400, 2014.
- [20] G. Mattana, T. Kinkeldei, D. Leuenberger et al., "Woven temperature and humidity sensors on flexible plastic substrates for

- e-textile applications,” *IEEE Sensors Journal*, vol. 13, no. 10, pp. 3901–3909, 2013.
- [21] G. Cho, K. Jeong, M. J. Paik, Y. Kwun, and M. Sung, “Performance evaluation of textile-based electrodes and motion sensors for smart clothing,” *IEEE Sensors Journal*, vol. 11, no. 12, pp. 3183–3193, 2011.
- [22] J. Zięba, M. Frydrysiak, L. Tesiorowski, and M. Tokarska, “Textronic clothing to ECG measurement,” in *2011 IEEE International Symposium on Medical Measurements and Applications, MeMeA 2011*, Italy, May 2011.
- [23] X. Xiao, T. Hua, L. Li, and J. Wang, “Geometrical modeling of honeycomb woven fabric architecture,” *Textile Research Journal*, vol. 85, no. 16, pp. 1651–1665, 2015.
- [24] X. Xiao, T. Hua, J. Wang, L. Li, and W. Au, “Transfer and mechanical behavior of three-dimensional honeycomb fabric,” *Textile Research Journal*, vol. 85, no. 12, pp. 1281–1292, 2015.
- [25] W. Wu, H. Zhang, S. Pirbhulal, S. C. Mukhopadhyay, and Y.-T. Zhang, “Assessment of biofeedback training for emotion management through wearable textile physiological monitoring system,” *IEEE Sensors Journal*, vol. 15, no. 12, pp. 7087–7095, 2015.
- [26] A. K. Belchandan, K. Deshmukh, and J. Kumar, “Removal of noises in ECG signal by using digital FIR-IIR filter in VHDL,” *Digital Signal Processing*, vol. 8, no. 5, pp. 135–139, 2016.
- [27] A. Gupta and S. Bhandari, “ECG noise reduction by different filters: a comparative analysis,” *International Journal of Research in Computer and Communication Technology Advance Technology*, vol. 4, no. 7, pp. 424–431, 2015.
- [28] A. Sahu and J. Kumar, “Filtering of ECG signal using adaptive and non adaptive filters,” *Manager’s Journal on Digital Signal Processing*, vol. 4, no. 1, pp. 1–2, 2016.
- [29] K. K. Patro and P. R. Kumar, “De-noising of ECG raw signal by cascaded window based digital filters configuration,” in *IEEE Power, Communication and Information Technology Conference, PCITC 2015*, pp. 120–124, India, October 2015.